

LLE Review

Quarterly Report



About the Cover:

The cover photo shows Jim Tellinghuisen, OMEGA Experiments Technician, positioning an electronic x-ray camera (charge injection device, CID) at the image plane of a Kirkpatrick–Baez (KB) microscope deployed on the OMEGA target chamber. The first article in this issue details the use of these cameras on OMEGA.



Shown at left is a wide-field view of the OMEGA target chamber's diagnostic port (H13), which contains a KB microscope with a CID camera at the image plane (the long tube pointing downward). The final beam injection mirrors surround the port. A pinhole camera with CID-camera readout is located just above the KB microscope.

This report was prepared as an account of work conducted by the Laboratory for Laser Energetics and sponsored by New York State Energy Research and Development Authority, the University of Rochester, the U.S. Department of Energy, and other agencies. Neither the above named sponsors, nor any of their employees, makes any warranty, expressed or implied, or assumes any legal liability or responsibility for the accuracy, completeness, or usefulness of any information, apparatus, product, or process disclosed, or represents that its use would not infringe privately owned rights. Reference herein to any specific commercial product, process, or service by trade name, mark, manufacturer, or otherwise, does not necessarily constitute or imply its endorsement, recommendation, or favoring by

the United States Government or any agency thereof or any other sponsor. Results reported in the LLE Review should not be taken as necessarily final results as they represent active research. The views and opinions of authors expressed herein do not necessarily state or reflect those of any of the above sponsoring entities.

The work described in this volume includes current research at the Laboratory for Laser Energetics, which is supported by New York State Energy Research and Development Authority, the University of Rochester, the U.S. Department of Energy Office of Inertial Confinement Fusion under Cooperative Agreement No. DE-FC03-92SF19460, and other agencies.

Printed in the United States of America
Available from
National Technical Information Services
U.S. Department of Commerce
5285 Port Royal Road
Springfield, VA 22161

Price codes: Printed Copy A04
Microfiche A01

For questions or comments, contact Frederic J. Marshall,
Editor, Laboratory for Laser Energetics, 250 East River Road,
Rochester, NY 14623-1299, (716) 275-2279.

Worldwide-Web Home Page: <http://www.lle.rochester.edu/>

LLE Review



Quarterly Report

Contents

In Brief	iii
Imaging of Laser–Plasma X-Ray Emission with Charge-Injection Devices (CID’s)	119
X-Ray Spectroscopic Measurements of Areal Density and Modulations of Compressed Shells in Implosion Experiments on OMEGA	124
Secondary D- ³ He Proton Spectra from D ₂ -Filled OMEGA Targets	130
Comparison of a Liquid Crystal Point-Diffraction Interferometer and a Commercial Phase-Shifting Interferometer	142
Understanding the Mechanism of Glass Removal in Magnetorheological Finishing (MRF)	157
Publications and Conference Presentations	

In Brief

This volume of the LLE Review, covering April–June 2000, features an article by F. J. Marshall, T. Ohki, D. McInnis, Z. Ninkov, and J. Carbone, who detail the conversion of the OMEGA time-integrated x-ray diagnostics to electronic readout using direct-detection x-ray cameras [charge-injection devices (CID's)]. Pinhole and x-ray microscope images are shown along with inferred calibration measurements of the CID cameras. Currently, the same cameras are being used to obtain x-ray spectra in a TIM-based spectrometer, extending their use to all time-integrated imaging and spectroscopic x-ray instruments used on OMEGA.

Additional highlights of the research presented in this issue are

- V. A. Smalyuk, B. Yaakobi, F. J. Marshall, and D. D. Meyerhofer investigate the spatial structure of the temperature and density of target-shell plasmas at peak compression (stagnation). This is accomplished by examining the energy dependence of the x-ray emission using narrow-band x-ray filters and the known absorption properties of the shell dopant (Ti).
- F. Séquin, C. K. Li, D. G. Hicks, J. A. Frenje, K. M. Green, R. D. Petrasso, J. M. Soures, V. Yu. Glebov, C. Stoeckl, P. B. Radha, D. D. Meyerhofer, S. Roberts, C. Sorce, T. C. Sangster, M. D. Cable, S. Padalino, and K. Fletcher detail the physics and instrumentation used to obtain and interpret secondary D-³He proton spectra from current gas-filled-target and future cryogenic-target experiments. Through a novel extension of existing charged-particle detection techniques with track detectors, the authors demonstrate the ability to obtain secondary proton spectra with increased sensitivity.
- M. Guardelben, L. Ning, N. Jain, D. Battaglia, and K. Marshall compare the utility of a novel liquid-crystal-based, point-diffraction interferometer (LCPDI) with the commercial standard phase-shifting interferometer and conclude that the LCPDI is a viable low-cost alternative.
- A. B. Shorey, S. D. Jacobs, W. I. Kordonski, and R. F. Gans detail the mechanisms of glass polishing using the magnetorheological finishing (MRF) technique currently being studied in the Center for Optics Manufacturing (COM). Material-removal experiments show that the nanohardness of carbonyl iron (CI) is important in MRF with nonaqueous MR fluids with no nonmagnetic abrasives, but is relatively unimportant in aqueous MR fluids and/or when nonmagnetic abrasives are present.

Frederic J. Marshall
Editor

Imaging of Laser–Plasma X-Ray Emission with Charge-Injection Devices (CID’s)

Introduction

X-ray imaging and x-ray spectroscopy are used in laser–plasma-generated physics research to diagnose conditions in the laser targets. Examples of techniques used to image x-ray emission are pinhole cameras, Kirkpatrick–Baez (KB) microscopes, curved crystal optics, and Wölter microscopes.^{1–3} All spectroscopic diagnostics rely also on spatial resolution to record an x-ray spectrum. Examples of spectroscopic techniques are Bragg crystal diffraction and grating diffraction. The simplest method of recording images is time-integrated exposure of film, a common example being the calibrated Kodak direct exposure film (DEF).⁴ Alternatively, images can be recorded by a solid-state device that is either directly sensitive to x rays (photons absorbed in the device) or indirectly sensitive (photons absorbed in a phosphor coating, generating visible range photons that are then absorbed in the device).

This work details the method of obtaining time-integrated images of laser–plasma x-ray emission using charge-injection devices (CID’s), as has been demonstrated on the University of Rochester’s 60-beam UV OMEGA laser facility.⁵ The CID has an architecture similar to a charge-coupled device (CCD). The differences make them more resistant to radiation damage and, therefore, more appropriate for some applications in laser–plasma x-ray imaging. Images were obtained with pinhole cameras, KB microscopes,² and a tunable monochromatic x-ray microscope.⁶ Simultaneous images obtained on these systems with calibrated x-ray film have enabled determination of the absolute detection efficiency of the CID’s in the energy range from 2 to 8 keV.

Charge-Injection Devices (CID’s)

The CID cameras used in this work are manufactured by CID Technologies, Inc. of Liverpool, NY.⁷ The model CID4150 is an 812×604 array having square pixels with $38.5\text{-}\mu\text{m}$ center-to-center spacing and overall array dimensions of 31.3×23.2 mm. Details of the pixel architecture found in the literature^{8–11} are summarized as follows: Each pixel contains two storage areas (pads). At the start of integration,

voltage applied to both pads injects any stored charge into the substrate layer. Next, charge is accumulated under a negatively biased column storage pad until the bias is changed to transfer the stored charge to a row pad. The row pad is attached to a row preamplifier from which the signal is output and digitized. The CID’s used in this work were operated at room temperature and with no conversion phosphor coating on the detector surface (direct x-ray detection). A PC-based analog-to-digital converter with 16-bit resolution, operating at 500 kHz, accomplished the camera readout. The relatively high-speed readout was employed to minimize dark current in the uncooled detectors.

Figure 83.1 shows a CID camera in its housing and an epoxy-encased dental imaging version,¹¹ for comparison, alongside a film pack and film pack positioner, illustrating the relative compactness of the CID camera. All signal amplification and switching electronics are contained in the CID camera. An overview of the installation on the OMEGA target chamber and surrounding structure is shown in Fig. 83.2. The

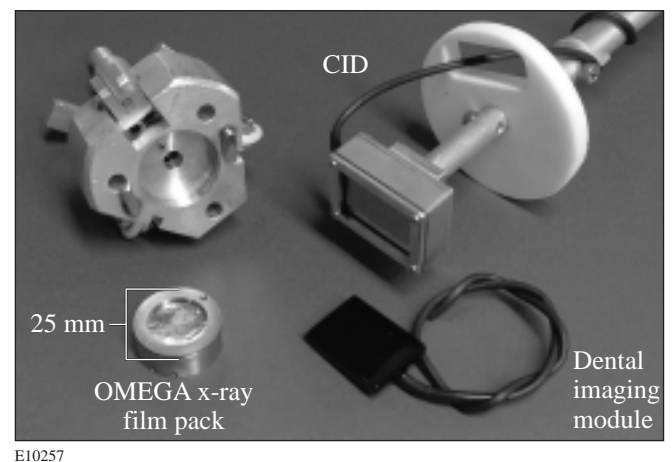


Figure 83.1
Picture of CID camera mounted on the end of a pinhole camera positioner. The CID camera replaces the film pack holder (upper left) and film pack (lower left). The CID camera was designed to be compact, as evidenced by the dental imaging version (lower right).

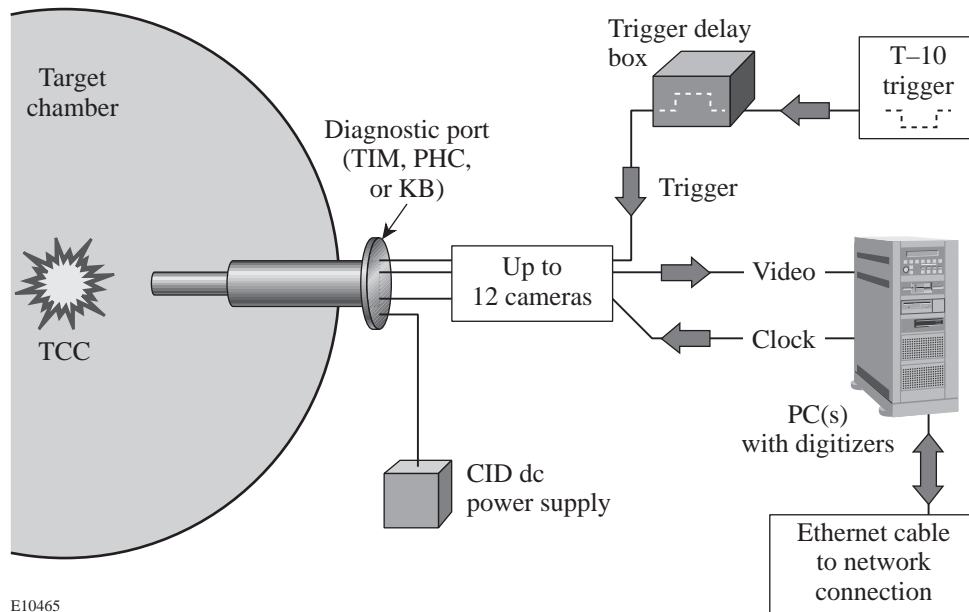


Figure 83.2
Schematic of the CID camera interface to an OMEGA x-ray diagnostic.

E10465

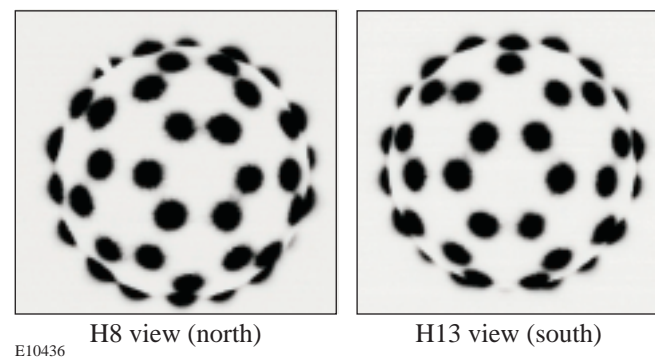
dc power is supplied along with a clocking line and an integration trigger line. The common integration trigger supplies each camera in use with a pre-shot pulse to acquire a background image and an on-shot pulse to acquire an image on the laser target shot. The two images are subtracted to provide the final image. The single output line contains the unformatted video signal, which is sent to a PC-based analog-to-digital converter card (ADC). Up to two PC's are used to acquire six CID camera outputs per PC, on as many as 12 CID cameras for the currently planned system.

Experiments

The CID cameras were used to obtain images of laser-plasma x-ray emission on OMEGA. Three different diagnostics were used as platforms for these tests: x-ray pinhole cameras and two different KB microscopes. One microscope was outfitted with a grating and used to obtain grating-dispersed images of target implosion cores.¹² The other microscope was outfitted with metal multilayer monochromators and used to obtain narrow-energy-band (monochromatic) x-ray images of target implosion cores.⁶

Figure 83.3 shows two images obtained with pinhole cameras located on opposite sides of the target chamber. The pinhole cameras have $11\text{-}\mu\text{m}$ pinholes and were located 170 mm from the target. The CID's were located to provide images with a magnification of 4.0 ($\sim 10\text{ }\mu\text{m}/\text{pixel}$ at the target plane). The images are of x-ray emission from a 4-mm-diam, Au-coated plastic sphere. The OMEGA beams were surface focused onto the target using the standard OMEGA optics and

distributed phase plates designed to produce Gaussian-like focal spots with a diameter of $\sim 900\text{ }\mu\text{m}$ (containing 95% of the energy). These produce x-ray spots with diameters of $\sim 600\text{-}\mu\text{m}$ full width at half-maximum (FWHM). The images are analyzed to determine the relative pointing of each beam compared to the desired pointing (all beams pointed so as to converge at the target center, in the spherical-implosion-pointing mode). Typically six or more film-based cameras are used to obtain like images, necessitating film loading, unloading, developing, drying, and finally digitizing. Although these processes are streamlined by using auto film developers, quick drying, and video camera digitizing, the typical minimum processing time of ~ 40 min cannot compete with the several-minute time scale required to store and redisplay multiple digital image files.



E10436

Figure 83.3
CID images taken from two opposing pinhole cameras on an OMEGA pointing shot.

Another example of CID-camera-obtained x-ray images is shown in Fig. 83.4. The CID's were located behind the same pinhole cameras described above, but farther away at a magnification of 8.0. The images are of the time-integrated x-ray emission from an imploded laser fusion target (in this case, a 3-atm-D₂-filled, 20- μ m-thick CH shell). Figure 83.4(a) was taken with minimum filtration in front of the CID sensor (150 μ m of Be, mostly in the pinhole camera itself), while Fig. 83.4(b) was taken with a CID on a pinhole camera on the opposite side of the target chamber and additional filtration of 50 μ m of Al was used to limit the soft x-ray component of the image. Figure 83.4(a) clearly shows the target's outer-shell emission plus stalk emission (all of which occurs during target acceleration). Figure 83.4(b) shows only the harder x-ray emission that is confined to the high-density, high-temperature implosion core region.

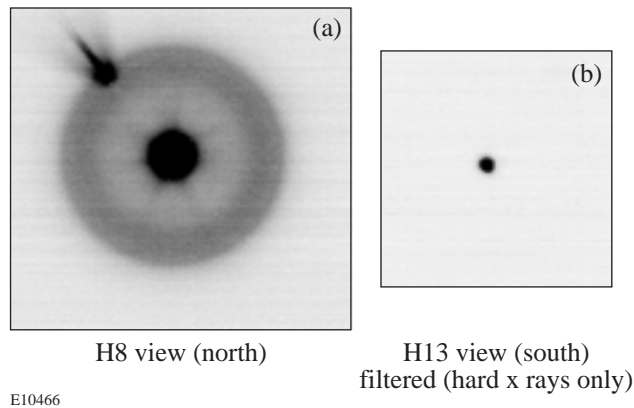


Figure 83.4
CID images of a directly driven imploding OMEGA laser target (from opposing pinhole cameras): (a) soft x-ray image containing emission from the outer shell region, the stalk, and a saturated core region; (b) hard x-ray image containing only emission from the core.

Pairs of images, one on film and one with a CID on the same x-ray microscope, have been obtained on a series of OMEGA target shots. The KB microscope was outfitted with a diffraction grating that yielded dispersed spectra of the implosion cores.¹² The magnification of the images is 20.3. Since the KB microscope is a four-mirror, four-image version with image views separated by 1.4° on the target chamber sphere, the images are nearly identical except for differences in the recording media. Figure 83.5 shows a pair of such images: (a) a film-recorded image (Kodak DEF) and (b) a CID-camera-recorded image. Both images are produced by the KB microscope,

which has Ir-coated mirrors operating at grazing angles of 0.70°. Attenuation by 140 μ m of Be is common to both, as is diffraction by the 0.2- μ m-period transmission grating. The CID camera had an additional 25 μ m of Be acting as a light shield and housing cover. Both images show nearly identical features. The main features captured by the grating-dispersed microscope (zeroth-order image of implosion and first-order diffracted image of the core) are seen in both images. Since the film and microscope have been absolutely calibrated, comparison of the film- and CID-recorded core spectra can be used to infer the absolute sensitivity of the CID pixels. Figure 83.6(a) shows such a comparison taken along the core spectrum and plotted as a function of photon energy. The CID pixel's inferred quantum efficiency dependence on energy is shown in Fig. 83.6(b). Although a precise model for the CID pixels has not been developed, the results of Janesick *et al.*¹³ for the case of a front-side-illuminated, thin-depletion-region CCD are shown for comparison in Fig. 83.6(b). This model should be representative of the CID sensitivity.

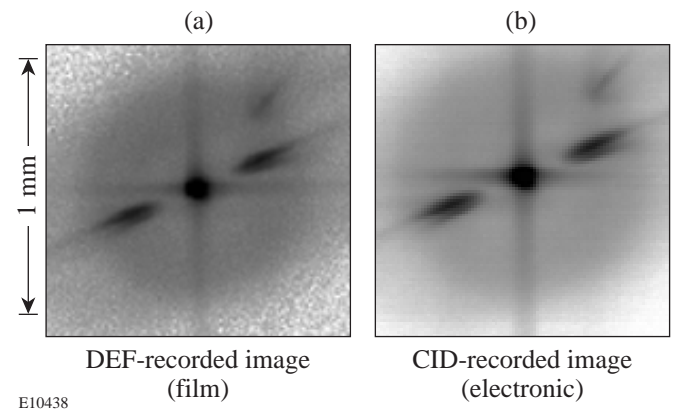


Figure 83.5
A pair of simultaneously recorded x-ray microscope images taken with (a) Kodak DEF film and (b) a CID camera. The image is an imploding OMEGA target with dispersion of the core emission by an x-ray transmission grating (evidenced by the features $\sim 30^\circ$ from the horizontal to the upper right and lower left). The horizontal and vertical streaks are due to small-angle specular scattering from the microscope mirrors.

Lastly, a pair of images taken with the KB microscope outfitted with metal multilayer monochromators is shown in Fig. 83.7. The imaging system has been previously described.⁴ WB₄C multilayers with a 2d spacing of 26.5 Å were used, and the magnification of the images is 13.6. The monochromators were tuned so as to produce images of target emission centered on the Ar He-like β -line (3.683 ± 0.011 keV) and the Ar H-like

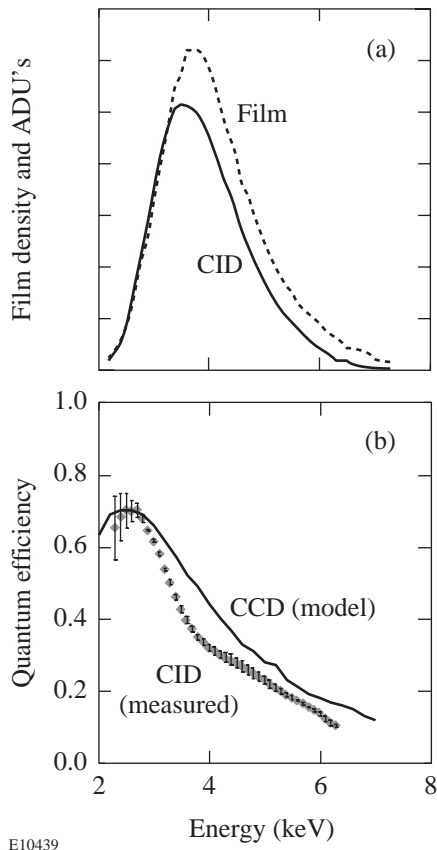


Figure 83.6

Comparison of CID- and film-recorded spectra. (a) Lineouts through the two spectral features; (b) inferred CID quantum efficiency, derived from the calibrated constants of the microscope/grating/film system.

β -line (3.935 ± 0.012 keV), where the indicated energy range is determined by the FWHM's of the monochromator diffraction peaks. The target was a 15-atm, D_2 -filled, 20- μm -thick, 1-mm-diam CH shell containing 0.35% by atomic number of Ar gas as a dopant. The images show the enhanced line-plus-continuum emission from the implosion core region. The asymmetry of the core is ascribed to the lack of perfect direct-drive beam balance on this shot, aggravated by several lower-intensity beams being near each other on the target chamber sphere. The images show a clear core region whose size and morphology can be easily measured.

Conclusion

CID cameras have been used to obtain time-integrated x-ray images on a variety of imaging and spectroscopic diagnostics on the OMEGA laser facility's target chamber. Cross calibration of the CID camera with film shows that the CID pixels,

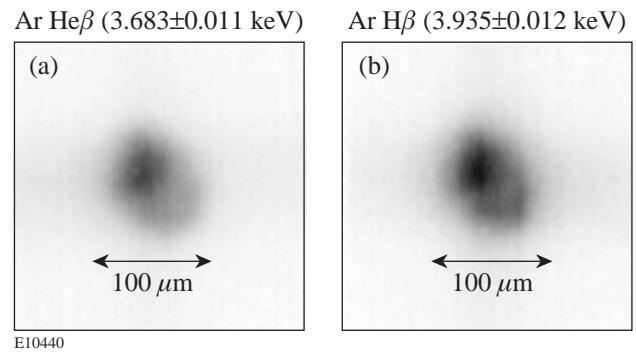


Figure 83.7

Monochromatic images of an imploding OMEGA laser target taken with two CID cameras. (a) Image of emission at 3.683 ± 0.011 keV, centered on the Ar He-like β -line; (b) image of emission at 3.935 ± 0.012 keV, centered on the Ar H-like β -line.

when used in direct-detection mode (i.e., without a phosphor), have a useful energy range of better than 2 to 8 keV, with additional sensitivity to be expected, especially at higher energies. Currently, all existing OMEGA time-integrated x-ray diagnostics are being outfitted with CID cameras as an optional recording medium.

ACKNOWLEDGMENT

The authors acknowledge the support of the OMEGA laser operations group and the staff at the University of Rochester's Laboratory for Laser Energetics. This work was supported by the U. S. Department of Energy Office of Inertial Confinement Fusion under Cooperative Agreement No. DE-FC03-92SF19460, the University of Rochester, and the New York State Energy Research and Development Authority. The support of DOE does not constitute an endorsement by DOE of the views expressed in this article.

REFERENCES

1. J. A. Koch *et al.*, *Appl. Opt.* **37**, 1784 (1998).
2. F. J. Marshall and Q. Su, *Rev. Sci. Instrum.* **66**, 725 (1995).
3. N. M. Ceglio, A. M. Hawryluk, and R. H. Price, *Appl. Opt.* **21**, 3953 (1982).
4. B. L. Henke *et al.*, *J. Opt. Soc. Am. B* **3**, 1540 (1986).
5. T. R. Boehly, D. L. Brown, R. S. Craxton, R. L. Keck, J. P. Knauer, J. H. Kelly, T. J. Kessler, S. A. Kumpan, S. J. Loucks, S. A. Letzring, F. J. Marshall, R. L. McCrory, S. F. B. Morse, W. Seka, J. M. Soures, and C. P. Verdon, *Opt. Commun.* **133**, 495 (1997).
6. F. J. Marshall and J. A. Oertel, *Rev. Sci. Instrum.* **68**, 735 (1997).
7. CID Technologies, Inc., Liverpool, NY 13088.

8. Z. Ninkov, C. Tang, and R. L. Easton, in *Charge-Coupled Devices and Solid State Optical Sensors IV*, edited by M. M. Blouke (SPIE, Bellingham, WA, 1994), Vol. 2172, pp. 180–186.
9. J. J. Zarnowski *et al.*, in *Charge-Coupled Devices and Solid State Optical Sensors IV*, edited by M. M. Blouke (SPIE, Bellingham, WA, 1994), Vol. 2172, pp. 187–198.
10. J. Carbone *et al.*, in *Solid State Arrays and CCD Cameras*, edited by C. N. Anagnostopoulos, M. M. Blouke, and M. P. Lesser (SPIE, Bellingham, WA, 1996), Vol. 2654, pp. 131–138.
11. J. Carbone *et al.*, in *Solid State Sensor Arrays: Development and Applications II*, edited by M. M. Blouke (SPIE, Bellingham, WA, 1998), Vol. 3301, pp. 90–99.
12. F. J. Marshall, J. A. Delettrez, R. Epstein, and B. Yaakobi, *Phys. Rev. E* **49**, 4381 (1994).
13. J. R. Janesick *et al.*, *Opt. Eng.* **26**, 156 (1987).

X-Ray Spectroscopic Measurements of Areal Density and Modulations of Compressed Shells in Implosion Experiments on OMEGA

Introduction

In inertial confinement fusion (ICF), spherical targets are driven either directly with laser beams¹ or indirectly with x-ray drive.² Initial target nonuniformities, either existing or created by the drive, can grow because of hydrodynamic instabilities disrupting the implosion and reducing its thermonuclear yield.³ Therefore, it is important to measure the effects of these instabilities on the target performance and particularly on the shell integrity. Fusion reactions occur during the stagnation phase, at peak compression, when the maximum density and temperature are achieved. Simultaneously, the hot core and the inner surface of the shell emit most of their radiation in x rays.³ This emission not only contains information about important parameters such as areal density, temperature, and their uniformity in the region from where the emission originates (hot core and inner shell), but can also be used to probe the rest of the cold shell.⁴ While the shell's final areal density, neutron yield, and core temperature are important parameters of the target performance, the shell's integrity provides a more direct signature of instability.

Cold-shell integrity has been measured for shells with Ti-doped layers.⁵ Monochromatic core images were obtained at energies below and above the *K*-edge energy of Ti with a pinhole-array x-ray spectrometer.⁶ The ratio between such images reflects the nonuniformity of the cold shell; however, these measurements were limited to implosions with 20- μm -thick shells and 1-ns square pulse shape, which had the highest-intensity x-ray emission from the core. Slowly rising pulse shapes and thicker shells produce implosions with lower core intensity. When measured with a pinhole-array spectrometer, this intensity was insufficient to perform meaningful analysis.

In the present experiments the sensitivity of the measurements is increased by replacing the diffracting crystal in the pinhole-array spectrometer with filters for sampling the spectrum below and above the Ti *K* edge. This allows for measurements of shell integrity for 20- and 24- μm -thick shells with both the 1-ns square pulse shape and a slower-rising, 2.3-ns pulse that has a 1:6 foot-to-main-pulse intensity ratio (PS26).

Pure CH targets were used to measure nonuniformities in radiation temperature and uniformity of the emitting (hot) part of the target, which consists of the core and inner part of the shell.

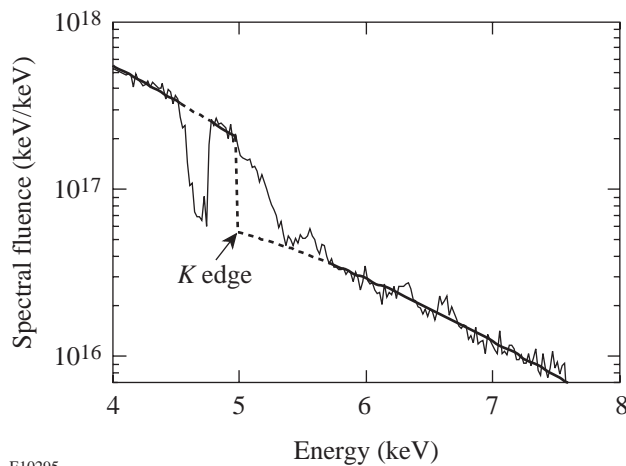
In this article three measurement methods are described: (1) Imaging of the cold-shell modulations is based on the imaging of core radiation in two x-ray energies, absorbed and nonabsorbed by the shell. The ratio of intensities in the two narrow-energy-band x-ray images is used to infer modulation in the areal density of the absorbing shell. (2) Measurements of temperature nonuniformities in the core radiation use core images from two energy bands, both unattenuated by the shell. (3) Imaging of the hot-shell modulations measures emission nonuniformities at x-ray energies unattenuated by the shell. Since most of this emission comes from the inner, hot shell, the modulations in the images are related to the hot shell's areal-density nonuniformities.

Experiments

The targets used in these experiments were CH shells of $\sim 450\text{-}\mu\text{m}$ inner radius and 20- and 24- μm shell thickness. Targets with Ti had 2- μm , Ti-doped CH (6.2% by atom) layers at the inner part of the shell. Targets were filled with 3 or 15 atm of D_2 . Targets were irradiated with 351-nm laser light using the 60-beam OMEGA laser system.⁷ Two pulse shapes were used in these experiments: a 1-ns square pulse shape with total on-target energy of about 25 kJ and PS26 with a duration of ~ 2.5 ns and total on-target energy of about 20 kJ. Beam-smoothing techniques used during these experiments included distributed phase plates⁸ (DPP's) and smoothing by spectral dispersion⁹ (SSD). The 2-D SSD had an IR bandwidth of $1.25 \text{ \AA} \times 1.75 \text{ \AA}$, producing a 0.2-THz bandwidth at 351 nm. The estimated illumination uniformity for 60 overlapping OMEGA beams with DPP's and SSD was $\sigma_{\text{rms}} \sim 2.5\%$, which was calculated from the on-target single-beam distribution and averaged over the length of the pulse.¹⁰ Beam-to-beam energy variations were typically $\sim 7\%$, which produces an additional on-target illumination nonuniformity of $\sigma_{\text{rms}} \sim 2.5\%$, with most of that contribution in modes 1 through 5.¹⁰

The thin solid line in Fig. 83.8 shows the measured spectrum of the core emission integrated over the time of a stagnation phase at peak compression (~ 300 ps) and integrated over the area of the core ($\sim 80 \mu\text{m}$). The spectrum is from the implosion of a $24\text{-}\mu\text{m}$ -thick shell, with a $2\text{-}\mu\text{m}$ inner Ti-doped layer and an initial D_2 fill pressure of 3 atm by 1-ns-square-pulse illumination. The spectrum was measured with a spectrometer fitted with an ammonium dihydrogen phosphate (ADP) crystal and a $15\text{-}\mu\text{m}$ -wide slit. The spectrum contains absorption lines due to $1s\text{-}2p$ transitions in Ti ions near the 4.6-keV energy.¹¹ These lines are absorbed within the warm Ti-doped region ($T \sim 300$ to 600 eV), whereas radiation above the Ti K edge at 4.96 keV is absorbed by much colder Ti. The intensity above the K edge falls down gradually rather than abruptly, indicating a temperature gradient in the absorbing region and an associated gradual K -edge shift to higher energies due to ionization.¹¹ The electron temperature of the emission region ($T_e = 0.86 \pm 0.04$ keV) and the areal density of cold Ti in the shell ($\rho R_{\text{Ti}} = 2.1 \pm 0.1$ mg/cm²) have been derived from the fit to the measured spectrum, shown by the thick solid line outside absorption areas of warm Ti (at ~ 4.6 keV) and shifted K edge.

This spectrum was used not only to identify the spectral regions of x rays appropriate for imaging but also to calculate imaging sensitivity in order to convert intensity modulations in the image to modulations of the shell's areal density.



E10295

Figure 83.8

Measured time-integrated spectrum of the core emission taken with a $24\text{-}\mu\text{m}$ -thick shell with a $2\text{-}\mu\text{m}$ inner Ti-doped layer, at an initial fill pressure of 3 atm D_2 , and 1-ns-square-pulse illumination.

Imaging of Cold-Shell Modulations

To measure the shell's integrity, the target is imaged at energies weakly absorbed by the shell, below the Ti K edge, and at energies strongly absorbed by the shell (above the Ti K edge at about 6.5 keV). The compressed core radiation serves as a backlighter for the shell.⁵ Any modulations in this emission are measured from the core image below the K edge. The image above the K edge has approximately the same modulations in the backlighter and additional modulations in the absorbing shell.

Time-integrated images of core emission were taken with a $6\text{-}\mu\text{m}$ pinhole array, at $4\times$ magnification, and recorded on DEF film. Two images were taken with a Ti filter at energies below the Ti K edge (~ 4.9 keV); the other two images were taken with an iron filter at energies above the Ti K edge (~ 6.5 keV). A schematic of the instrument is shown in Fig. 83.9. Instead of one image per energy channel, a pair of images were taken not only to reduce noise by averaging images but also to estimate the noise itself by subtracting one image from another. The calculated resolution for the imaging system was $\sim 6 \mu\text{m}$, with modulation transfer functions (MTF's) very similar for both 4.9- and 6.5-keV energy channels. The noise spectrum has been used in the Wiener filter applied to reduce noise during image processing. The thicknesses of both the Ti and the Fe filters were varied for different shots in order to achieve an optimum intensity on the film since intensity levels were different for different shot conditions.

The energy spectrum was measured for each target experiment using the crystal spectrometer. The approximate x-ray energy spectra of the images for each energy channel were calculated by multiplying this spectrum by the filter response. Figure 83.10(a) shows the spectra calculated for the lower-energy filter (solid line) and the higher-energy filter (dotted line). The conditions of the target experiment were a $20\text{-}\mu\text{m}$ -thick CH shell with a $2\text{-}\mu\text{m}$ inner Ti-doped layer, filled with 3 atm of D_2 , irradiated by a 1-ns square pulse. Lineouts of two lower-energy-band images (solid lines) and two higher-energy-band images (dotted lines) are shown in Fig. 83.10(b). Note that the lineouts from the same energy band have similar features that are different from the features in the other energy band. This indicates that the features seen in the images are not noise, and that the differences between the images at different energies are likely due to modulations in the absorbing shell. (It is assumed that the core-emission image does not change appreciably over an $\sim 1.6\text{-keV}$ interval in photon energy between the two energy bands, i.e., the features of the core

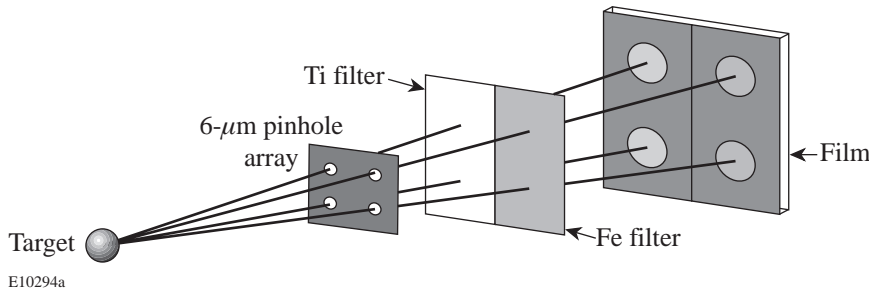


Figure 83.9

Schematic of the 6- μm filtered pinhole array. Two time-integrated images are obtained with a Ti filter at energies below the Ti K edge (~ 4.9 keV); the other two images are obtained with an Fe filter at energies above the Ti K edge (~ 6.5 keV). The magnification of the images is $4\times$ and the images are recorded with DEF film.

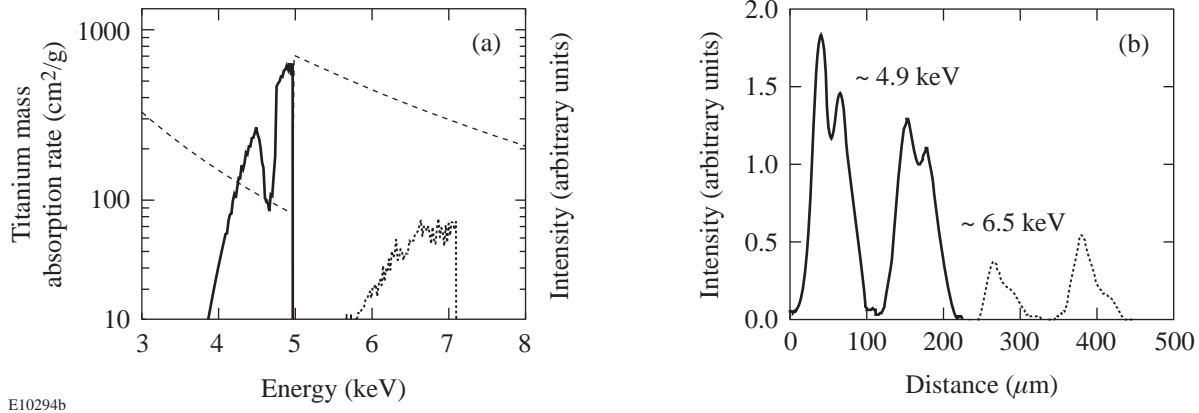


Figure 83.10

(a) The calculated spectra of the images below the Ti K edge (solid line) and above the Ti K edge (dotted line). The Ti mass absorption rate is shown by the dashed line. (b) The lineouts of two images taken below the Ti K edge (solid line) and above the Ti K edge (dotted line).

emission are the same at ~ 4.9 and ~ 6.5 keV. (This assumption is confirmed in the next section.)

The images were processed with the Wiener-filtering technique.¹² If $C(\mathbf{f})$ is the signal plus noise of the image (obtained by averaging two images for a particular x-ray energy channel) in Fourier space with coordinates \mathbf{f} , and $\langle N(\mathbf{f}) \rangle$ is the average spectrum of the noise (calculated from the difference of two images for a particular energy band), then the restored signal spectrum $R(\mathbf{f})$ is given by the Wiener-filter formula¹²

$$R(\mathbf{f}) = \frac{C(\mathbf{f})}{\text{MTF}(\mathbf{f})} \cdot \frac{|C(\mathbf{f})|^2 - \langle |N(\mathbf{f})|^2 \rangle}{|C(\mathbf{f})|^2}, \quad (1)$$

where $\text{MTF}(\mathbf{f})$ is the modulation transfer function of the pinhole camera calculated for a particular x-ray energy channel. The filtered images are obtained by transforming the restored spectrum $R(\mathbf{f})$ back to real space.

The modulations of the ratio of intensities for filtered images below the K edge [$I_{<K}(\mathbf{x})$] and above the K edge [$I_{>K}(\mathbf{x})$] are related to the shell-areal-density modulations $\delta[\rho R(\mathbf{x})]$ by

$$\delta[\rho R(\mathbf{x})] = \delta \left\{ \ln \left[\frac{I_{<K}(\mathbf{x})}{I_{>K}(\mathbf{x})} \right] \right\}_{\mu_{>K} - \mu_{<K}}, \quad (2)$$

where $\mu_{>K}$ and $\mu_{<K}$ are the spectrally weighed mass absorption coefficients of cold Ti at energies above and below K edge, respectively, which were calculated for each shot using the measured x-ray spectra [Fig. 83.10(a)].

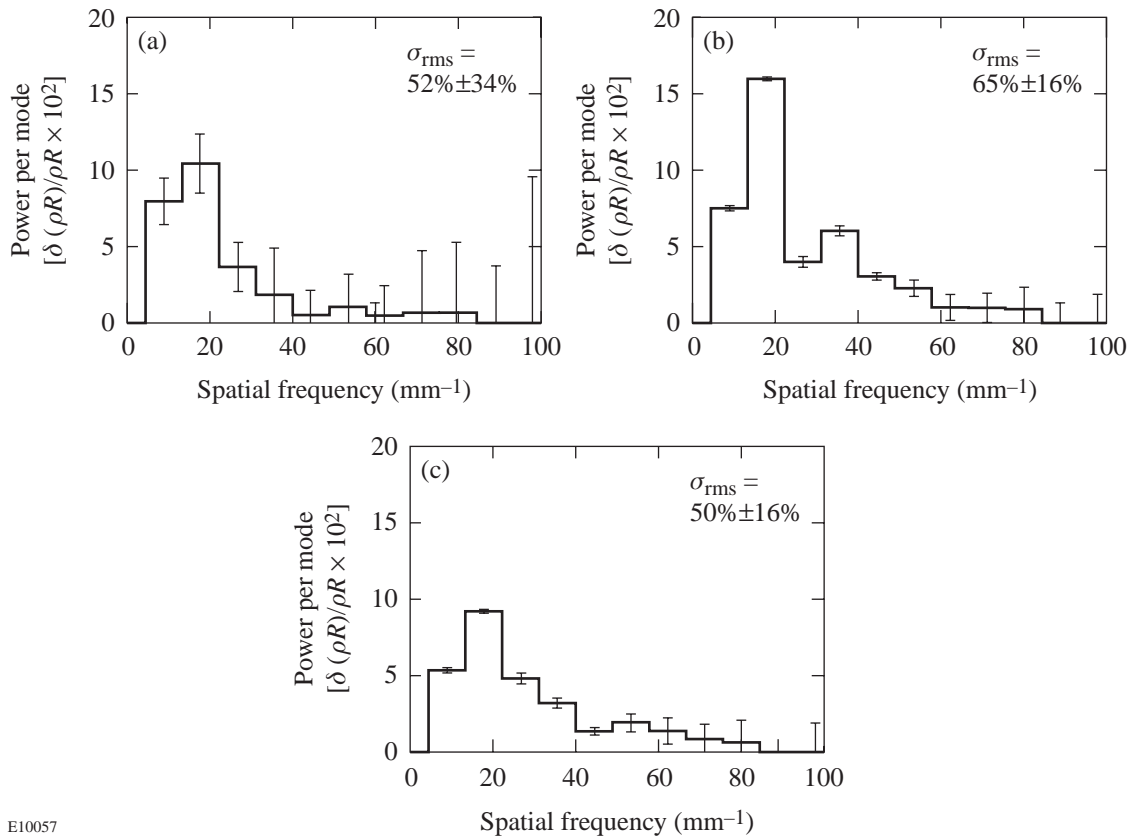
Figure 83.11 shows the power per mode of the measured modulation as a function of spatial frequency of the cold, Ti-doped shell areal density at peak compression. The data are from three target experiments, measured using core images taken at x-ray energies above and below the Ti K edge. For each

target experiment, the areal-density modulations were normalized to the measured cold-shell areal densities, which were deduced from the crystal spectrometer data, similar to that shown in Fig. 83.8, yielding relative modulations in the cold-shell areal density $\delta[\rho R(\mathbf{x})]/\rho R(\mathbf{x})$. To minimize errors due to spherical effects in the analysis of the outer section of the core images, only the 60- μm -diam central portion of each 100- μm -diam image was analyzed. The spectra in Figs. 83.11(a) and 83.11(b) correspond to 20- and 24- μm -thick-shell targets driven with a 1-ns square pulse shape. The spectrum in Fig. 83.11(c) corresponds to a 24- μm -thick-shell target driven with pulse shape PS26. All three targets were filled with 3 atm of D_2 . To obtain the power per mode, shown in Fig. 83.11, absolute values of the Fourier amplitudes squared were summed at each spatial frequency. The σ_{rms} of the total nonuniformity is the square root of the sum of the power per mode over the spatial frequency. The spectra shown in Fig. 83.11 are very similar. They are peaked at a spatial frequency of 20 mm^{-1} (corre-

sponding to a wavelength of $50 \mu\text{m}$ or mode number $\ell \sim 5$) with spatial features extending down to a wavelength of about $15 \mu\text{m}$. The total σ_{rms} of the nonuniformities is similar for all three shots and is $\sim 50\% \pm 20\%$. Adding previous data⁵ to these measurements, we conclude that the nonuniformity σ_{rms} ranges from the noise level of $\sim 20\%$ up to $\sim 50\%$ and is similar for target experiments with a 20- or 24- μm -thick shell and with 1-ns square or PS26 pulse shapes.

Measurements of Temperature Nonuniformities

Measurements of the cold-shell integrity are based on the assumption that the distribution of core emission does not change appreciably over an $\sim 1.6\text{-keV}$ interval in photon energy between the two energy bands at ~ 4.9 and $\sim 6.5 \text{ keV}$. This assumption is valid if the effective emission temperature is constant over the whole area of the image. We use the term “effective” with respect to temperature in order to emphasize that the measured images of the cores are two dimensional, and



E10057

Figure 83.11 Power per mode of the measured modulation as a function of spatial frequency for target experiments with (a) 20- μm -thick shells and 1-ns square pulse shape, $\sigma_{\text{rms}} = 52\% \pm 34\%$, (b) 24- μm -thick shells and 1-ns square pulse shape, $\sigma_{\text{rms}} = 65\% \pm 16\%$, and (c) 24- μm -thick shells and PS26 pulse shape, $\sigma_{\text{rms}} = 50\% \pm 16\%$. All experiments were taken with 3-atm- D_2 -filled shells with a 2- μm -thick, inner-Ti-doped (6.2% by atom) layer.

not three dimensional as the cores are themselves. The intensity at each point is an integral over the core in the direction of the imaging system. Regions with different temperatures may exist inside the core; however, when integrated along the path toward the imaging system, only an integrated or effective temperature is observable.

Figure 83.12 represents the lineouts of the core images measured with Sn filters at an x-ray energy of about 3.5 keV (solid lines) and with Fe filters at an x-ray energy of about 6.5 keV (dashed lines). These data are from a target experiment with a 24- μm -thick CH shell (no Ti doping), filled with 15 atm of D_2 and driven by a 1-ns square pulse shape. At x-ray energies of ≈ 3 keV, the core emission is not significantly absorbed by the outer shell. Differences in the shapes of the images as a function of energy band would indicate the presence of nonuniformities in the effective temperature. Lineouts of the captured images shown in Fig. 83.12 are, in fact, very similar. The image features are similar for the two images taken from the same energy band, indicating that these features are not noise. The fact that these features have the same shape for both energy bands indicates that the effective temperature is nearly constant over the entire area of the images. The measured effective temperature $T_{\text{eff}} = 0.86 \pm 0.04$ keV was found from the ratio of two different energy-band images shown in Fig. 83.12.

A similar analysis was performed on results from experiments with other conditions, including different CH-shell thicknesses and different pulse shapes. For all of these shots

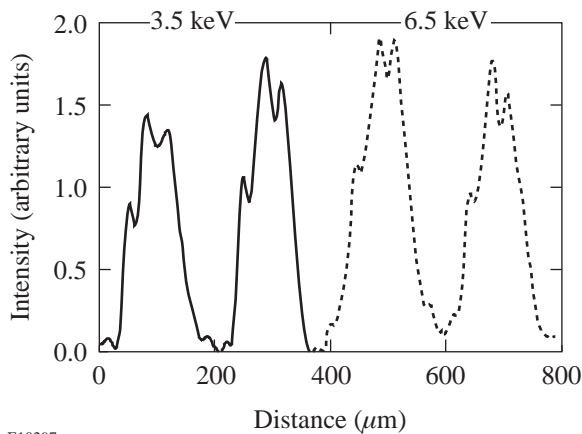


Figure 83.12

The lineouts of two images taken at ~ 3.5 keV (solid line) with a Sn filter, and at ~ 6.5 keV (dashed line) with an Fe filter for a target experiment on a 24- μm -thick shell, filled with 15 atm of D_2 , driven by a 1-ns square pulse shape.

effective temperatures were constant over the whole area of the images within the experimental error determined by the noise in the images.

Imaging the Hot-Shell Modulations

As shown above, the core images have no temperature nonuniformities within the experimental resolution and sensitivity; the modulations seen in the high-energy, unattenuated images are due to areal-density modulations in the emission region. The core images are produced by the emission from the hot core and dominated by the emission from the inner hot shell; therefore, modulations in the image lineouts shown in Fig. 83.12 are mostly due to hot-shell areal-density modulations. Assuming that the absorption of x rays in the core and the shell is negligible, the intensity at the detector is proportional to the areal density of the emission region in the direction of x-ray propagation.

To analyze the areal-density nonuniformity of the hot inner shell, the smooth envelope of the core image $I_{\text{env}}(\mathbf{x})$ (obtained by filtering the image in Fourier space) was subtracted from the core image $I(\mathbf{x})$. The relative areal-density nonuniformity of the hot shell is given by the relation

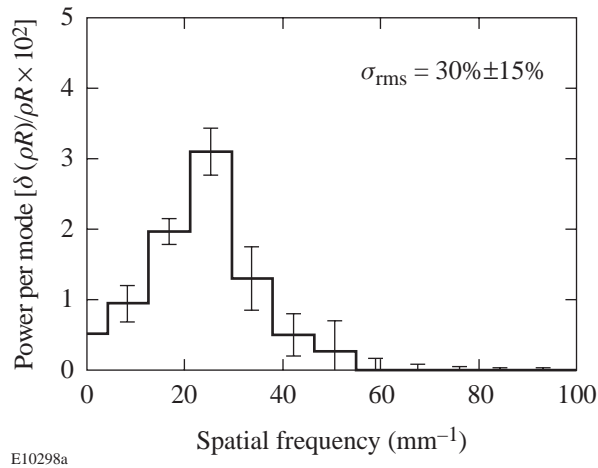
$$\frac{\delta[\rho R(\mathbf{x})]}{\rho R(\mathbf{x})} = \sqrt{2} \left(\frac{I(\mathbf{x}) - I_{\text{env}}(\mathbf{x})}{I_{\text{env}}(\mathbf{x})} \right). \quad (3)$$

Since the signals from both “walls” of the hot shell are added to give $I(\mathbf{x})$, the relative nonuniformities in the captured image $[I(\mathbf{x}) - I_{\text{env}}(\mathbf{x})]/I_{\text{env}}(\mathbf{x})$ are multiplied by the factor of $\sqrt{2}$ in order to analyze modulations corresponding to only one wall of the shell (the assumption made here was that areal-density perturbations in the shell region are uncorrelated).

Figure 83.13 shows the measured power per mode of the areal-density nonuniformities as a function of spatial frequency for the hot inner shell. The spectrum is peaked at spatial scale lengths of 40 to 50 μm with a total σ_{rms} of $30\% \pm 15\%$. It is similar to the measured cold-shell spectra in both magnitude and shape.

Conclusions

Time-integrated measurements of the shell integrity are presented at peak compression, the final stage of a spherical implosion. Perturbations in the cold, or absorbing, part of the shell were studied using shells with and without inner Ti-doped layers. The hot, or emitting, part of the shell was studied using pure plastic shells. It is found that modulations in both



E10298a

Figure 83.13

Power per mode of hot CH plasma emission as a function of spatial frequency for a target experiment on a 24- μm -thick shell, filled with 15 atm of D_2 , driven by a 1-ns square pulse shape, $\sigma_{\text{rms}} = 30\% \pm 15\%$.

the cold and hot parts of the shell are peaked at spatial scale sizes of 40 to 50 μm , with nonuniformities extending to $\sim 15 \mu\text{m}$. The magnitude of relative areal-density perturbations is in the range from the noise level of $\sim 15\%$ to 20% up to $\sim 50\%$ for both 1-ns square and PS26 pulse shapes. Time-resolved measurements at peak compression and earlier, in the deceleration phase, will aid in understanding the present findings.

ACKNOWLEDGMENT

This work was supported by the U.S. Department of Energy Office of Inertial Confinement Fusion under Cooperative Agreement No. DE-FC03-92SF19460, the University of Rochester, and the New York State Energy Research and Development Authority. The support of DOE does not constitute an endorsement by DOE of the views expressed in this article.

REFERENCES

1. S. E. Bodner, D. G. Colombant, J. H. Gardner, R. H. Lehmberg, S. P. Obenschain, L. Phillips, A. J. Schmitt, J. D. Sethian, R. L. McCrory, W. Seka, C. P. Verdon, J. P. Knauer, B. B. Afeyan, and H. T. Powell, *Phys. Plasmas* **5**, 1901 (1998).
2. J. D. Lindl, *Phys. Plasmas* **2**, 3933 (1995).
3. D. K. Bradley, J. A. Delettrez, R. Epstein, R. P. J. Town, C. P. Verdon, B. Yaakobi, S. Regan, F. J. Marshall, T. R. Boehly, J. P. Knauer, D. D. Meyerhofer, V. A. Smalyuk, W. Seka, D. A. Haynes, Jr., M. Gunderson, G. Junkel, C. F. Hooper, Jr., P. M. Bell, T. J. Ognibene, and R. A. Lerche, *Phys. Plasmas* **5**, 1870 (1998).
4. B. Yaakobi, F. J. Marshall, D. K. Bradley, J. A. Delettrez, R. S. Craxton, and R. Epstein, *Phys. Plasmas* **4**, 3021 (1997).
5. B. Yaakobi, V. A. Smalyuk, J. A. Delettrez, R. P. J. Town, F. J. Marshall, V. Yu. Glebov, R. D. Petrasso, J. M. Soures, D. D. Meyerhofer, and W. Seka, in *Inertial Fusion Sciences and Applications '99*, edited by W. J. Hogan C. Labaune, and K. A. Tanaka (Elsevier, Paris, 2000), pp. 115–121.
6. B. Yaakobi, F. J. Marshall, and D. K. Bradley, *Appl. Opt.* **37**, 8074 (1998).
7. T. R. Boehly, D. L. Brown, R. S. Craxton, R. L. Keck, J. P. Knauer, J. H. Kelly, T. J. Kessler, S. A. Kumpan, S. J. Loucks, S. A. Letzring, F. J. Marshall, R. L. McCrory, S. F. B. Morse, W. Seka, J. M. Soures, and C. P. Verdon, *Opt. Commun.* **133**, 495 (1997).
8. Y. Lin, T. J. Kessler, and G. N. Lawrence, *Opt. Lett.* **20**, 764 (1995).
9. S. Skupsky, R. W. Short, T. Kessler, R. S. Craxton, S. Letzring, and J. M. Soures, *J. Appl. Phys.* **66**, 3456 (1989).
10. F. J. Marshall, J. A. Delettrez, V. Yu. Glebov, R. P. J. Town, B. Yaakobi, R. L. Kremens, and M. Cable, *Phys. Plasmas* **7**, 1006 (2000).
11. B. Yaakobi, R. S. Craxton, R. Epstein, and Q. Su, *J. Quant. Spectrosc. Radiat. Transfer* **58**, 75 (1997).
12. V. A. Smalyuk, T. R. Boehly, D. K. Bradley, J. P. Knauer, and D. D. Meyerhofer, *Rev. Sci. Instrum.* **70**, 647 (1999); W. H. Press *et al.*, *Numerical Recipes in FORTRAN: The Art of Scientific Computing*, 2nd ed. (Cambridge University Press, Cambridge, England, 1992), pp. 701–715.

Secondary D-³He Proton Spectra from D₂-Filled OMEGA Targets

Introduction

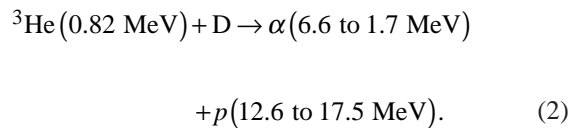
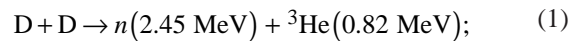
Two new diagnostic techniques now provide the first high-quality spectra of secondary fusion protons from imploded D₂-filled capsules in inertial confinement fusion (ICF) experiments. The potential utility of secondary neutrons and protons for diagnosing such capsules has been recognized for more than two decades,^{1–8} but practical use of protons has previously been limited by the lack of accurate spectroscopic measurements. The first new technique utilizes a magnet-based charged-particle spectrometer; the second involves “wedge-range-filter”-based spectrometers utilizing special filters and CR39 nuclear track detectors. These spectrometers were recently used to acquire data from target capsules with about 14 atm of D₂ fuel in 19- μ m-CH shells, imploded at the 60-beam OMEGA laser facility by irradiation with 22 kJ of laser energy. Results of that work, presented in this article, are important for the information they give about current experiments and for the potential they show for characterization of the cryogenic D₂-filled capsules to be used in the near future.

The general value of charged-particle spectrometry for capsule diagnostics has recently been demonstrated with magnet-based charged-particle spectrometers (CPS's), which are now used on a regular basis to measure spectra of primary fusion products (p , D, T, α) and “knock-on” particles (p , D, T, and ³He elastically scattered by 14.1-MeV neutrons³)^{9,10} for a wide range of capsule types and implosion conditions on OMEGA.¹¹ Measured spectra provide a number of important implosion parameters such as primary yields, fuel ion temperature, and areal density (ρR) of fuel, shell(s), or fuel plus shell. Areal densities are determined by measuring the energy loss of charged fusion products as they pass out through the fuel and shell⁹ or by measuring the yields of knock-on particles.¹⁰

In the most important future ICF experiments utilizing cryogenic capsules with DT or D₂ fuel, large areal densities will limit the number of diagnostic measurements that can be made of charged particles. On the National Ignition Facility (NIF), ρR_{total} of imploded DT capsules is eventually expected to exceed 1 g/cm². In this case, the only charged particles that

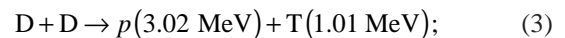
could escape and be detected for studying ρR are tertiary protons,¹² which have energies as high as 30.8 MeV. DT capsules planned for OMEGA may (based on 1-D simulations) reach ρR_{total} of 0.2 to 0.3 g/cm². In this case, knock-on deuterons and tritons, resulting from elastic collisions with primary 14.1-MeV neutrons, could be detected and used to study ρR with CPS's.¹⁰

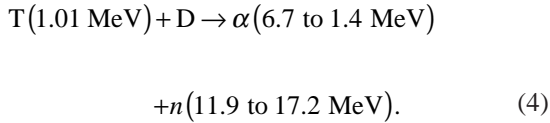
In the shorter term, cryogenic experiments will be carried out with pure-D₂ fuel. No charged primary fusion products will be energetic enough to escape and be detected, and there will be no high-energy primary neutrons to generate energetic knock-on particles. In addition, the method of determining ρR_{fuel} by measuring secondary-neutron yields⁶ will fail for $\rho R_{\text{fuel}} \geq 0.1$ g/cm². Fortunately, secondary D-³He protons (12.6 to 17.5 MeV) will escape from D₂-filled capsules with relatively high ρR . These protons are created in the two steps indicated in reactions (1) and (2):



In one of the primary branches of the D-D reaction, ³He is created with 0.82 MeV of kinetic energy. Some of the ³He ions then react in-flight with thermal D ions, creating protons that, because of the kinetic energy of the ³He, have a range of energies. Measured spectra of these protons can be used to measure ρR_{fuel} and ρR_{total} .

The remainder of this article will discuss the use of spectral measurements. Although the emphasis throughout is on secondary protons, there is also discussion of how they relate to the secondary neutrons created through reactions (3) and (4):





The following sections discuss (1) how the characteristics of secondaries are related to the physical parameters of capsules; (2) how accurately measured spectra of secondary protons are made with the magnet-based CPS's and with "wedge-range-filter"-based spectrometers; (3) measurements during OMEGA shots; (4) physical interpretation of data; and (5) future application to cryogenic-target experiments.

Secondary Spectra and Capsule Characteristics

Two simple models of plasma structure are used here to illustrate how measurements of secondary yields and spectra are related to properties of compressed capsules. In the "hot-spot" model, all primary fusion reactions take place in a small region at the center of the spherical fuel, and the fuel outside the hot spot, where the primary fusion products react with cooler fuel to create secondaries, has uniform density and temperature. In the "uniform" model, the fuel is uniform over its entire spherical volume so that primary and secondary reactions take place everywhere. In both cases, there can be a spherical shell or pusher of a different material outside the fuel (generally CH, in most current OMEGA experiments). It is assumed in these simple models that the capsule is spherically symmetric, with no mixing of fuel and shell material, although numerical work currently underway indicates that fuel/shell mixing could be important. In future work, more-sophisticated models will be used.

The slowing down of primary ³He and T in D fuel is modeled with the formalism described in Ref. 13, with results shown in Fig. 83.14. The production rates for secondaries are then determined by the cross sections shown in Fig. 83.15 (calculated from Ref. 14). The resultant yields, and the shapes of spectra as they are created in the fuel, are discussed below. Modifications to the spectrum of protons as they slow down on their way out of the fuel and shell are then determined by the stopping power illustrated in Fig. 83.16 (calculated according to Ref. 13).

1. Yields

By integrating over the appropriate paths of primary fusion products ³He and T and using the foregoing assumptions to calculate their energies as a function of position, and then utilizing the secondary production rates, we can calculate yields Y_{2p} and Y_{2n} of secondary protons and neutrons as fractions of the primary-neutron yield Y_{1n} and obtain the results shown in Fig. 83.17. Related calculations were carried out previously¹⁻⁸ for some of these cases, utilizing older models for the slowing down of ³He and T. The authors pointed out that a nearly linear relationship exists between ρR_{fuel} and the secondary-to-primary-yield ratios as long as ρR_{fuel} is low enough that the primary particles (³He or T) escape the fuel. Each yield ratio reaches a saturation level (as shown in Fig. 83.17) when the appropriate primary particle is completely slowed down in the fuel, but measurements of yield can be used to infer ρR_{fuel} as long as saturation has not been reached. The results are weakly dependent on plasma density, but the plasma temperature has a strong impact on the value of ρR_{fuel} at which the linear relationship fails because of com-

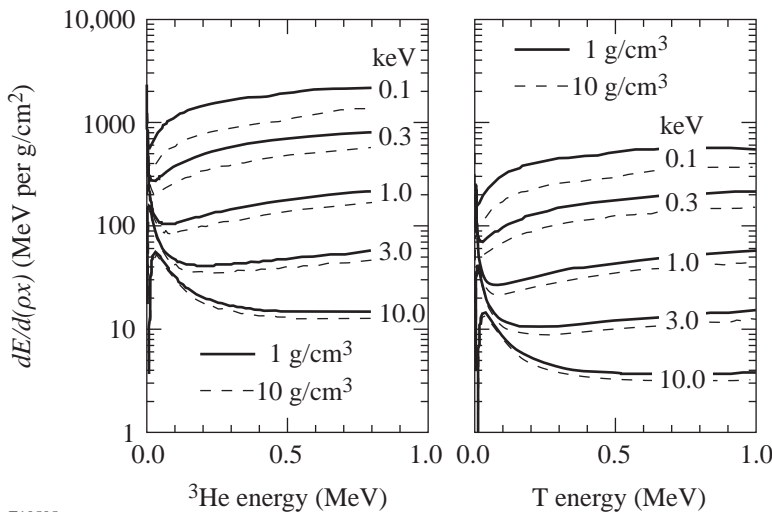
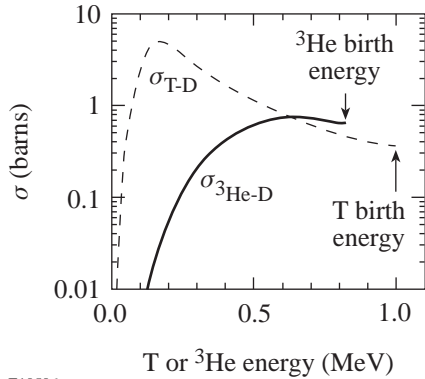


Figure 83.14
Stopping powers for ³He (left) and T (right) in D plasmas of various temperatures (calculated according to Ref. 13). Note that at higher temperatures there is an important peak in the stopping power at low energies, due to ion-induced slowing.

E10505

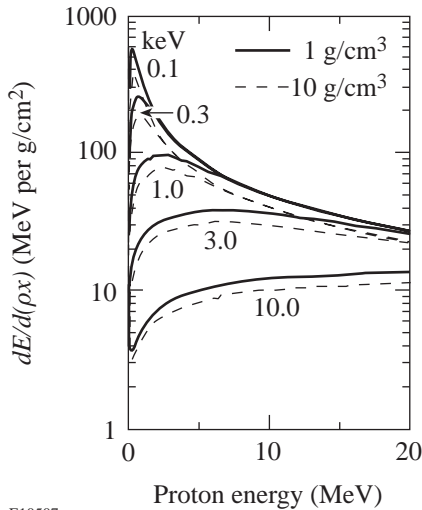
plete slowing down of the primary particles in the fuel. This is a consequence of the temperature dependence of the total particle ranges, as illustrated in Fig. 83.18. Because of the magnitude of the cross sections (Fig. 83.14), secondary protons are preferentially produced close to the birth position of primary ³He, while secondary neutrons are preferentially created near the end of the range of the primary T (see Fig. 83.19).



E10506

Figure 83.15

Fusion cross sections (σ) for energetic ³He or T with cold D plasma (calculated according to information in Ref. 14).



E10507

Figure 83.16

Stopping power for protons in D plasmas of various temperatures (calculated according to Ref. 13). The values for CH plasmas are almost identical except for being higher by a factor of about 14/13 (the ratio of the numbers of electrons per unit mass).

Two differences between the hot-spot and uniform models are apparent in Fig. 83.17: (1) The value of ρR_{fuel} for a given yield is slightly higher in the uniform model, reflecting the fact that the mean distance traveled by primary particles before they encounter the fuel–pusher interface is smaller by a factor of 0.75. (2) Complete saturation of yield at high values of ρR_{fuel} in the uniform model is approached asymptotically, but never reached, because some primaries are always created close enough to the surface to escape the fuel.

Although a measured secondary-proton yield can be used in the context of our models to infer ρR_{fuel} only in regimes where the primary ³He escapes the fuel before stopping, another kind of information can be inferred when complete stopping occurs in the fuel. As seen in Fig. 83.17, the electron temperature T_e determines the maximum possible secondary-to-primary ratio Y_{2p}/Y_{1n} . If it is known that yield saturation has been reached, it is possible to estimate the effective electron temperature as illustrated in Fig. 83.20. A similar relationship between electron temperature and yield saturation holds for secondary neutrons.

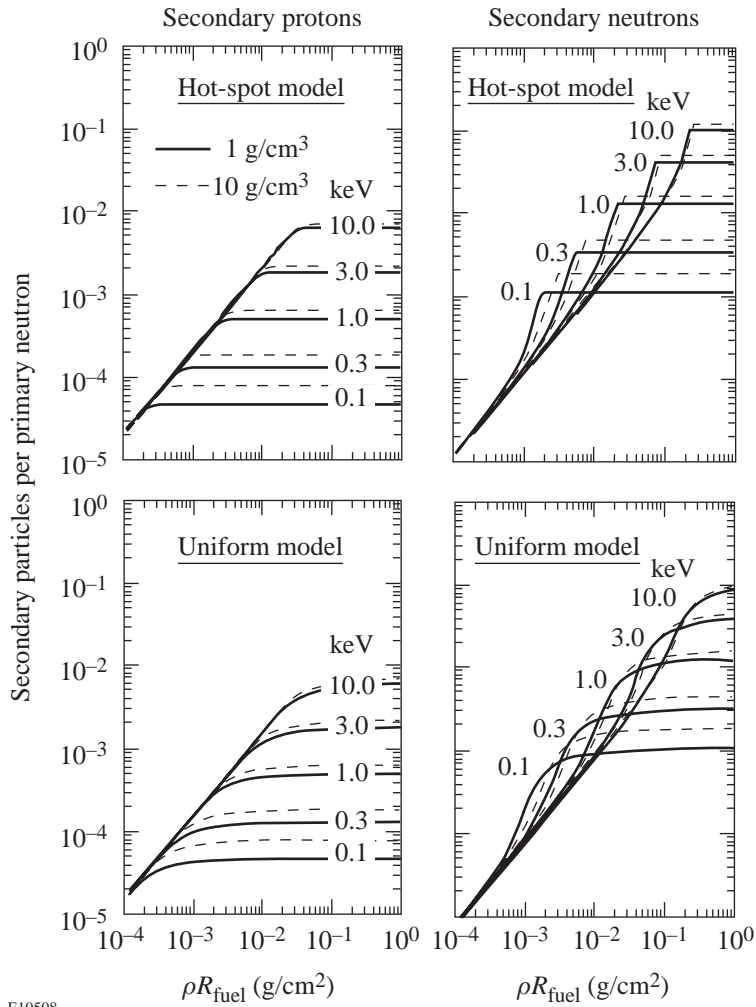
2. Birth Spectra

Going beyond the calculation of yields, we can investigate the shapes of secondary-particle spectra at their birth. Consider first the protons. If ρR_{fuel} is small, so that primary ³He particles escape the fuel before losing much of their 0.82-MeV birth energy, then the protons they produce by fusing with fuel deuterons are equally distributed between limiting energies of about 12.6 and 17.5 MeV. The energy limits are defined by kinematics and are determined by ³He energy at the time of interaction with D. The flat distribution as a function of energy between the limits can be demonstrated by assuming that fusion products are distributed isotropically in the D–³He center-of-mass frame, transforming to the lab frame, and calculating the number of particles per unit energy. The number of protons produced during the slowing down of ³He from energy $E_{3\text{He}}$ to $E_{3\text{He}} - \Delta E_{3\text{He}}$ is proportional to

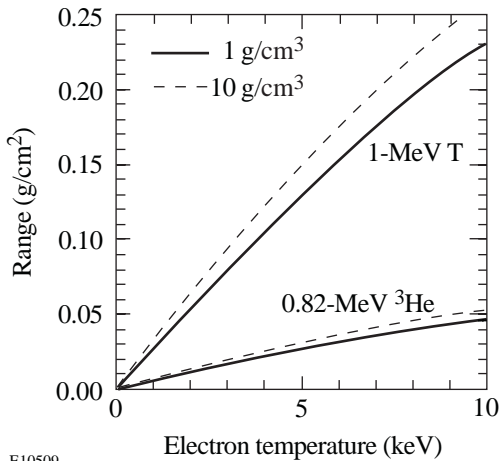
$$\Delta E_{3\text{He}} \sigma_{3\text{He-D}}(E_{3\text{He}}) / [dE_{3\text{He}}/d(\rho x)],$$

where $\sigma_{3\text{He-D}}(E_{3\text{He}})$ is as shown in Fig. 83.15, X is the distance along the trajectory of ³He in the plasma, and $dE_{3\text{He}}/d(\rho x)$ is as shown in Fig. 83.14.

For larger values of ρR_{fuel} , some of the ³He will slow down before leaving the fuel; when they interact with the fuel, the kinematically defined width of the resultant proton spectrum



E10508

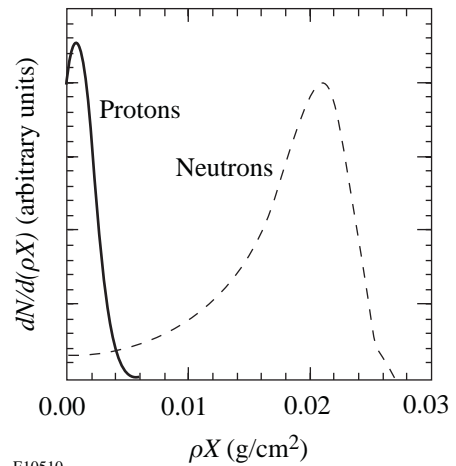


E10509

Figure 83.18
Ranges of primary D-D fusion products in a D plasma for different plasma densities and temperatures (from the stopping-power curves in Fig. 83.14).

Figure 83.17

Yields of secondary protons (left) and neutrons (right), calculated using Li and Petrasso's ion-slowing formalism¹³ to model the slowing down of primary fusion products in a D plasma. The two top plots assume the "hot-spot" model, in which all primary reactions take place in a small region at the center and secondary reactions take place outside the hot spot in a cooler region that is uniform in density and temperature. The two bottom plots assume the "uniform" model in which primary and secondary reactions take place throughout the uniform plasma. Plasma densities and electron temperatures T_e are as indicated.



E10510

Figure 83.19

Illustration of how secondary protons are created mostly near the birth position of the primary ³He, while secondary neutrons are created mostly toward the end of the range of primary T. The vertical axis is in arbitrary units that are different for the two curves; the horizontal axis unit ρX is the distance from primary birth position in g/cm² for a 1-keV, 3-g/cm³ D plasma.

will be smaller. But since $\sigma_{3\text{He-D}}(E_{3\text{He}})$ decreases rapidly as $E_{3\text{He}}$ goes below about 0.5 MeV, the contributions to the final proton spectrum become very small for lower-energy ³He and the shape of the total proton spectrum remains relatively insensitive to the amount of slowing down, or equivalently the value of ρR_{fuel} . This is demonstrated in Fig. 83.21, which shows how, in the case of a hot-spot model, the shape of the spectrum gets built up as a contribution of parts due to ³He

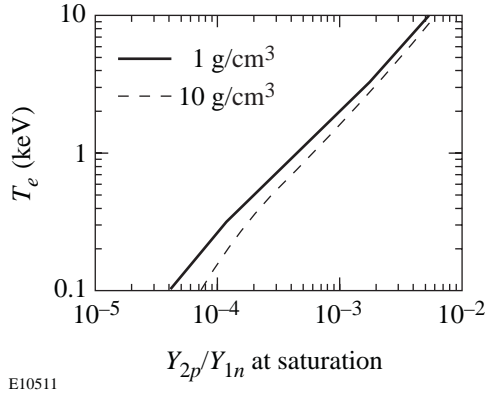


Figure 83.20
Electron temperature for which Y_{2p}/Y_{1n} cannot exceed a given saturation value (see Fig. 83.17). Under some circumstances, this relationship can be used to estimate T_e .

slowed down by different amounts. Figure 83.21 also illustrates that the shape of the birth spectrum is relatively insensitive to the plasma temperature. The mean energy of the spectrum varies slightly with the amount of slowing down of ³He, as shown in Fig. 83.22.

The secondary-neutron birth-spectrum shape is significantly more sensitive to ρR_{fuel} because the reaction cross section of primary T with fuel D increases rapidly as T energy decreases (down to about $E_T = 0.2$ MeV, as shown in Fig. 83.15). As discussed in Refs. 6–8, this means that the neutron spectrum gets narrower as ρR_{fuel} increases (and the exiting T energy decreases). Figure 83.21 illustrates this for the case of the hot-spot model.

3. Measured Spectra

A proton birth spectrum is never measured directly because it is modified by passage through the fuel and shell before being measured in a real experiment. Since the birth spectrum is relatively insensitive to fuel conditions, a measured spectrum contains diagnostic information about fuel and shell by virtue of the changes in the spectrum that can be inferred.

The mean energy of the secondary protons decreases according to the amount of material they traverse (Fig. 83.16

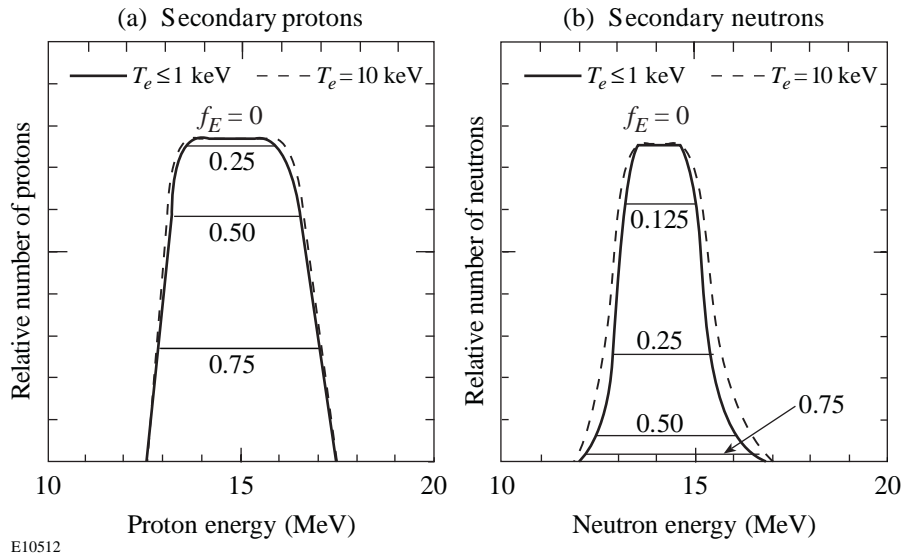


Figure 83.21
Calculated shapes of secondary-proton and -neutron spectra. These curves were generated by assuming that (a) the slowing of T or ³He in a D plasma varies with energy as shown in Fig. 83.14, and (b) the primary particles are created near the center and pass through a uniform fuel that ranges their energies down to some fraction f_E of their birth energy (hot-spot model). The plasma density was assumed to be 3 g/cm^3 . On each plot, the different curves show how the spectrum shape is built up as the primary particle gets ranged down; the curves *do not* show how the *number* of secondary particles varies with ρR . Each plot has one curve for plasma temperature 10 keV, corresponding to $f_E = 0$. This curve is arbitrarily normalized so its amplitude is the same as the corresponding curve for lower temperature to demonstrate that the shape is not strongly dependent on temperature.

showed how the stopping power of fuel or shell plasma for protons varies with proton energy and plasma temperature). For the case of a D plasma with $\rho = 3 \text{ g/cm}^3$, Fig. 83.23 illustrates the slowing down of secondary protons as a function of T_e and ρX , where X is distance traveled through the plasma. The dependence on ρ is weak; the ratio of ρX to the mean energy loss $\langle \Delta E_{2p} \rangle$ varies approximately as $\rho^{0.07}$ for $\rho X \leq 0.1 \text{ g/cm}^2$. The dependence on temperature is weak for $T_e \leq 1 \text{ keV}$ and becomes progressively stronger for increasing T_e . For a CH plasma, the ratio of ρX to $\langle \Delta E_{2p} \rangle$ is lower by about 13/14. If we assume that most of the protons are generated near the center of the fuel, then we can relate $\langle \Delta E_{2p} \rangle$ to a sum of contributions from ρR_{fuel} and ρR_{shell} .

The protons are not all generated precisely at the center of the fuel, so they pass through slightly different amounts of material while leaving the capsule. This affects the mean energy, but that effect is fairly small for the OMEGA data discussed here. It also causes a broadening of the spectrum, and in future work that broadening will be used as another constraint on capsule structure.

A secondary-neutron birth spectrum can be measured directly.¹⁵ The shape of this spectrum is sensitive to fuel conditions, so it has potential diagnostic value.⁸ Figure 83.24 summarizes the plasma parameter regimes in which the measurement methods described above are applicable.

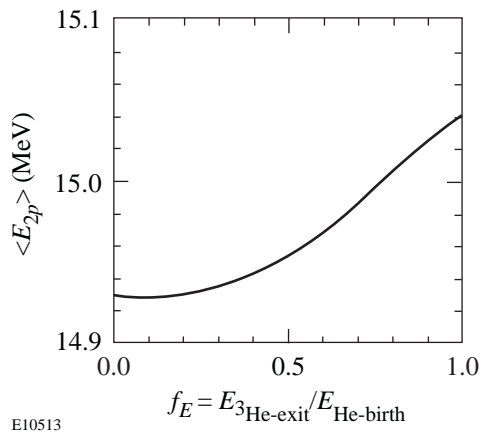


Figure 83.22
Dependence of the mean energies of the proton birth spectra (shown in Fig. 83.21) on the fraction of ³He energy remaining when the ³He reaches the fuel–pusher interface. Plasma temperature was assumed to be 3 keV, and the density was 3 g/cm³. If the appropriate value of f_E (defined in the previous figure caption) is unknown, the effective mean energy will be uncertain. In such a case, we could use the value $14.97 \pm 0.04 \text{ MeV}$, which corresponds to the assumption of equal probability for all values of f_E .

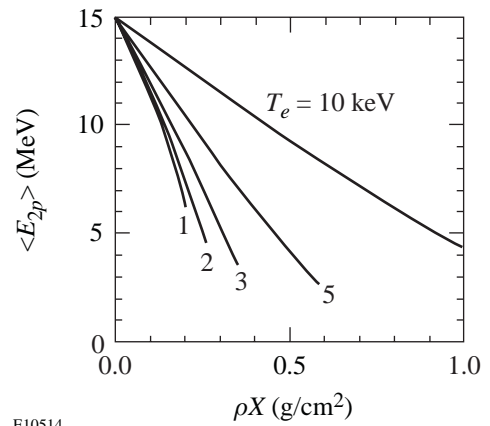


Figure 83.23
The mean energy of a secondary-proton spectrum after slowing down in a D plasma with $\rho = 3 \text{ g/cm}^3$. The horizontal axis unit ρX is distance from birth position in g/cm². For a CH plasma, the value of ρX corresponding to a given energy should be reduced by the factor 13/14 (the ratio of electrons per unit mass for D to the value for CH). The dependence on ρ is weak; for $\rho X \leq 0.1$, the value of ρX corresponding to a given energy varies approximately as $\rho^{0.07}$.

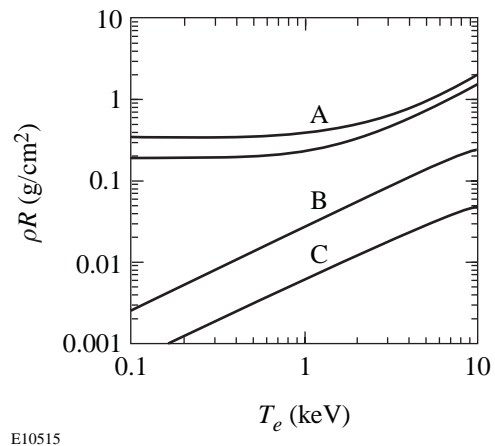


Figure 83.24
Boundaries of regimes in which various measurements can give diagnostic information about a 3-g/cm³, pure-D plasma (assuming the hot-spot model). Note that ρR refers to ρR_{total} for curve A, but ρR_{fuel} for curves B and C. (A) Measurements of Y_{2p}/Y_{1n} and secondary-proton energy shift can be made only in the region *below* these curves, which show the ρR_{total} at which secondary protons fail to escape from the plasma (one curve each for the upper and lower limits of the birth spectrum). (B) Measurements of Y_{2n}/Y_{1n} give information about ρR_{fuel} only in the region *below* this curve, which shows where primary T is ranged out completely by the fuel and where the “saturated” regions of Fig. 83.17 are reached. *Above* this curve, measurement of Y_{2n} could give information about the fuel electron temperature. (C) Measurements of Y_{2p}/Y_{1n} give information about ρR_{fuel} only in the region *below* this curve, which shows where primary ³He is ranged out completely by the fuel and where the saturated regions of Fig. 83.17 are reached. *Above* this curve, measurement of Y_{2p} can give information about the fuel electron temperature (see Fig. 83.20).

Instruments for Measuring Secondary-Proton Spectra

1. A Magnet-Based Charged-Particle Spectrometer

Two magnet-based spectrometers (CPS1 and CPS2) are installed on OMEGA. More information about CPS1 and CPS2 is available elsewhere,^{16,17} but the principle of operation is illustrated in Fig. 83.25, which shows how a magnet is used to separate protons (or other charged particles) of different energies into different trajectories. The particles are stopped in CR39 nuclear track detectors, which are subsequently etched in a solution of NaOH and water, and then scanned with a microscope. A small hole appears at the location of the track of each individual proton. The position of a particle track gives the particle energy directly by virtue of the trajectory followed through the magnet. Final determination of an energy spectrum involves subtracting a background noise level, which includes neutron-induced noise and “intrinsic track noise.” The neutron noise consists of tracks caused by protons elastically scattered by primary fusion neutrons, either in the CR39 itself or in surrounding materials; it scales with primary-neutron yield. The intrinsic track noise is caused by structural defects in the CR39, which look like particle tracks after etching; it is independent of implosion yields. Both types of noise are uniformly distributed on the CR39, subject to statistics.

Measuring secondary-proton spectra with CPS2 is more difficult than measuring other spectra, such as those of primary D-³He protons,⁹ for two reasons: (1) CR39 is not very sensitive to protons with energies higher than about 7 MeV, so when

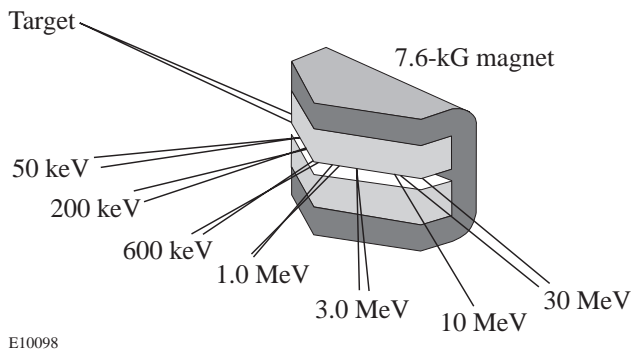


Figure 83.25

Concept of the magnet-based charged-particle spectrometers, showing how the magnetic field separates protons of different energies. Particles from the target capsule pass through a collimating aperture (not shown) before entering the magnet. After leaving the magnet, they are stopped in pieces of CR39 nuclear track detectors (not shown). The positions of the detected particles then indicate their energies by virtue of the trajectories followed.

detecting protons with higher energies it is necessary to use a filter to range the protons down in energy just before they impact the detector. This is not difficult for primary D-³He protons, which are nearly monoenergetic. But for the wide interval of incident energies associated with secondary protons, no single-filter thickness will range all protons down to the 0.5- to 7-MeV interval for which the detector is efficient. For this reason, a new filter whose thickness varies with position (or, equivalently, energy) was fabricated of aluminum. (2) Statistical noise is a significant problem. Typical primary D-D neutron yields in the OMEGA experiments have been of the order of 10^{11} , and the secondary-proton yield is usually in the vicinity of 10^8 . With a spectrometer slit width of 3 mm, a slit length of 15 mm (perpendicular to the magnet dispersion direction), and a target-to-slit distance of 100 cm, the maximum total number of detected protons per shot is about 360—enough to give reasonable statistical errors for the total yield and the mean energy, but the error bars on individual energy bins in a spectrum will be large. In addition, the number of background noise events that must be subtracted is comparable to the number of true proton events, making the statistical noise even worse. After dispersion by the magnet, the 360 protons are spread out over an area of about 3 cm^2 on the CR39, giving 120 protons/ cm^2 . This has to be compared with noise that comes from intrinsic defects and from neutrons. Intrinsic noise events generally appear at a density of the order of 50 per cm^2 . Neutron-induced events occur at about one per 10^4 neutrons, or about 45 per cm^2 on the CR39 (which is about 135 cm from the target); thus, for a single shot, the ratio of noise events to secondary-proton events is of the order of 1.

2. Wedge-Range-Filter Spectrometers

Another new type of spectrometer, a wedge-range-filter spectrometer (WFS), has recently been tried for the first time. In a WFS (which will be described in detail elsewhere¹⁸), CR39 is again used as the particle detector, and special filters are used to range down the proton energies so they fall within the interval of sensitivity of the detector. The advantages of using range-filter measurements are simplicity and the ability to operate at lower yields by getting closer to the target. The disadvantages are (1) the interval of incident energies that can be detected with a single-filter thickness is not wide enough to cover the entire secondary-proton spectrum, and (2) it is difficult to get accurate spectral information. Secondary-proton yields have previously been estimated in this way by counting proton tracks behind a constant-thickness filter,³⁻⁶ and Azechi *et al.*⁶ used such data to make broadband estimates of different parts of the proton spectrum.

To find an improved approach, we have recently performed highly detailed calibrations of the response of CR39 to protons of different energies (different energies result in different track sizes)¹⁹ and calibrations of the transmission characteristics of various filters. This information allows us to define a direct mapping between track diameter and incident proton energy for a given filter thickness. That mapping can be used to reconstruct part of the incident spectrum from a histogram of track diameters, but for each filter thickness the incident energy interval that is most accurately reconstructed is less than 1 MeV wide. To accurately reconstruct the entire secondary-proton spectrum, which is more than 5 MeV wide, it is necessary to have data from many different filter thicknesses. For this reason we use a special ranging filter with continuously varying thickness, making it possible to reconstruct a continuous spectrum over a wide energy interval. The filters used here were machined from aluminum, with thicknesses varying from 400 μm to 1800 μm . The fabrication tolerances turned out to be worse than desired, and the filters were slightly too thin. For the purposes of this first study, it was therefore necessary to estimate the thickness error by cross-calibrating the measured spectra with spectra acquired with the magnet-based CPS2. This single correction parameter was then applied to all data from WFS's. More-accurate fabrication and calibration techniques will make this unnecessary in the future.

A simple estimate of statistical errors can be made, assuming that a WFS is 15 cm from a capsule producing $Y_{1n} \approx 10^{11}$ and $Y_{2p} \approx 10^8$. With an effective area of about 3 cm² for the bulk of our spectrum, the number of incident protons will be about 10^5 . These are spread out over at least 5 MeV, and at each filter thickness only about 1/3 of the spectrum is detected, so the number of protons actually counted is $\sim 3 \times 10^4$. This makes intrinsic noise totally irrelevant, but the number of neutron-induced events is $\sim 1 \times 10^4$. By restricting ourselves to an appropriate subset of track diameters, the number of proton events can be reduced by a factor of 2 and the number of neutron events by a factor of 4. The ratio of noise events to secondary-proton events is thus only ~ 0.15 , and the large number of events guarantees very small statistical errors even after background subtraction.

Spectrum Measurements

1. Experiments

To illustrate the measurement and interpretation of secondary-proton spectra with our two new types of spectrometers, we present data from a recent series of four similar OMEGA shots. Table 83.I lists some basic shot parameters. The target capsules had ~ 14 atm of D₂ fuel in 19- μm -thick CH shells with

outer diameters of ~ 910 μm . Each capsule was imploded by irradiation with ~ 22 kJ of 0.35- μm UV light applied in 60 beams for 1 ns (in a square-top pulse). The light was smoothed by spectral dispersion (2-D SSD with 0.3-THz bandwidth²⁰). Primary-neutron yields Y_{1n} (measured via indium activation) varied from 8.1 to 9.8×10^{10} , while secondary-neutron yields Y_{2n} (measured with a time-of-flight diagnostic or Cu activation) were in the range of 1.1 to 1.8×10^8 . Yield-weighted ion temperatures were 3.2 to 3.5 keV (measured with a neutron time-of-flight diagnostic).

CPS2 proton data were acquired by exposing one piece of CR39 to the protons from all four shots in order to sum the yields and minimize errors due to counting statistics. The background noise level was determined by measuring the number of apparent events at energies higher than the upper energy of the secondary-proton spectrum, and this mean noise level was subtracted from the total spectrum to give the results shown in Fig. 83.26. Table 83.I lists the mean energy and the yield of this proton spectrum.

WFS data for each of the four shots were taken at a distance of 15 cm from the target. Resultant spectra are shown in Fig. 83.27, and measured parameters are listed in Table 83.I. Figure 83.28 shows how the average of these spectra compares to the spectrum from the magnet-based CPS2.

2. Measurement Uncertainties

The proton yields obtained with CPS2 or with one of the WFS's have measurement uncertainties due to counting statistics. In addition, each measurement represents an average over a small solid angle, and measurements made at multiple positions during the same shot have shown that there are angular variations in particle fluxes that substantially exceed uncertainties due to counting statistics. This spatial variation

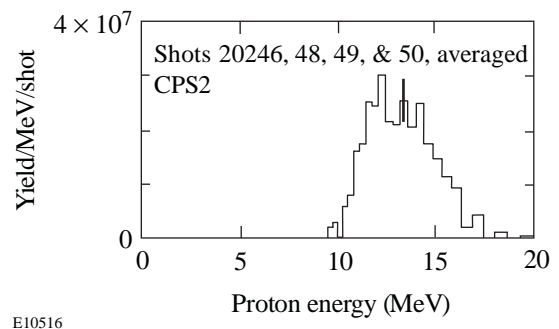
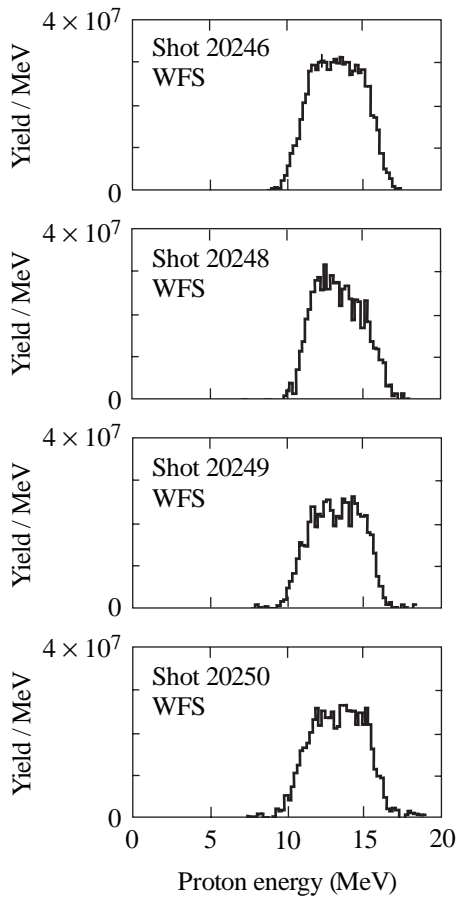


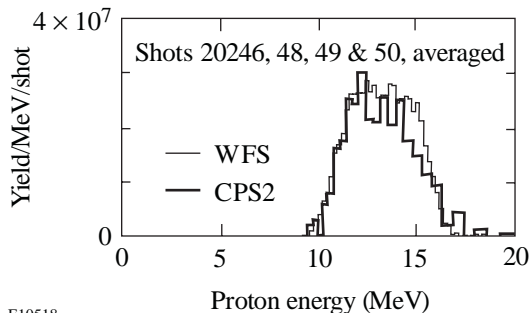
Figure 83.26
Spectrum of secondary protons for four shots, measured with the magnet-based spectrometer CPS2. One typical statistical error bar is shown.



E10517

Figure 83.27

Spectra of secondary protons for the four individual OMEGA shots, as measured with the wedge-range-filter spectrometers (WFS's). One typical statistical error bar is shown in the top plot. The statistical errors in the lower three plots are slightly higher because only 1/3 of the available data were used.



E10518

Figure 83.28

Comparison of the average spectrum measured with CPS2 (from Fig. 83.26) and the average of the individual WFS-measured spectra of Fig. 83.27.

of proton flux has been noted for a wide variety of shots and will be described in detail elsewhere. The standard deviation within measured spatial distributions of secondary-proton yield during individual shots tends to be in the vicinity of 20%. This puts a fundamental limit on the accuracy of any single yield measurement (as an indicator of total yield) and provides motivation for using multiple detectors.

The CPS2 yield measurements are affected by counting statistics in the measured spectra, including the subtracted background levels. The CPS2-measured proton-yield uncertainties quoted in Table 83.I were determined by adding, in quadrature, the statistical uncertainty (about 5%) and the expected standard deviation due to spatial variations (20% for a single shot, but 10% here for an average over four statistically independent shots). CPS2 measurements of mean energies have an uncertainty due to counting statistics (about 0.1 MeV here) and also due to any systematic energy calibration errors. Absolute calibration is accurate to about 0.1 MeV at 15 MeV.²¹ The spatial variations in particle flux mentioned above do not seem to be accompanied by energy variations, so the energy measurement uncertainties quoted in Table 83.I are obtained by adding the statistical error to the calibration uncertainty in quadrature.

The WFS yield measurements are subject to the same 20% uncertainty due to spatial variations. Statistical errors for these measurements tend to be much smaller (near 1% for each shot), so in Table 83.I a 20% uncertainty is assigned to each individual measurement. Since there are four individual and statistically independent measurements (for the four shots), the error assigned to the shot-averaged yield is 10%. Errors in the measurement of mean energy are caused by counting statistics, but these statistical errors are quite small (about 0.02 MeV for shot 20246). The calibration error is larger, and since the energy calibration for these preliminary measurements was artificially tied to the calibration of the magnet-based CPS2, we do not list errors here (this will be remedied in the future).

3. Performance of the Spectrometer Types

Overall, the secondary-proton spectra obtained with the WFS's have less noise than those from CPS2. Statistical errors per shot are a factor of 10 smaller because the detector can be closer to the target, can use a larger active area, and has a higher ratio of true signal events to noise events. This advantage will diminish when secondary yields increase, as they are expected to for cryogenic targets. For current yields, the performance benefits combine with simplicity to make this approach very useful as a complement to the CPS's and particularly attractive

for studying the spectrum from many directions simultaneously for symmetry characteristics.²² Theoretically, the WFS's should work at yields of ~10⁶ and up to ~10¹⁰ (by moving farther from the target). They will not work for yields of 10¹¹ or more, unless they can be moved well outside the target chamber, because of track overlap problems in the CR39. This probably limits their use to secondary (and tertiary) protons and, occasionally, primary protons from low-yield D-³He shots. The primary charged products of many other targets will have yields that are too high, and the measure-

ment of knock-on particles from DT targets,¹⁰ which is of great interest to the ICF program, requires a separation of different particle types (D, T, and p), which cannot be performed with this approach.¹⁹ These are appropriate applications for the magnet-based CPS's.

Interpretation of Measured Proton Spectra

1. Yield and Fuel Parameters

The measurements described above reflect properties of compressed targets, and in this section we look at implications

Table 83.I: OMEGA shot parameters, measurements, and inferred properties.

Parameter	Shot 20246	Shot 20248	Shot 20249	Shot 20250	<20246,48,49,50>
Fuel	14.2 atm D ₂	14.3 atm D ₂			
Shell	19 μm CH				
Outer Diameter	911 μm	909 μm	913 μm	905 μm	909.5 μm
Laser Energy	21.9 kJ	21.0 kJ	22.1 kJ	21.9 kJ	21.7 kJ
Laser Pulse	1 ns, square				
T _i (keV)	3.2±0.5	3.5±0.5	3.5±0.5	3.2±0.5	3.3±0.5
Y _{1n} (×10 ¹⁰)	9.76±0.07	8.06±0.06	8.28±0.06	9.17±0.07	8.82±0.03
Y _{2n} (×10 ⁷)	17.7±1.2	11.6±0.9	11.1±0.9	12.4±1.0	13.1±0.5
Y _{2p} (×10 ⁷)	15.8±3.1 ^{A,WFS}	11.8±2.4 ^{A,WFS}	12.1±2.4 ^{A,WFS}	12.1±2.4 ^{A,WFS}	11.4±1.3 ^{A,CPS2} 12.9±1.3 ^{A,WFS}
<E _{2p} > (MeV)	13.24 ^{B,WFS}	13.36 ^{B,WFS}	13.23 ^{B,WFS}	13.24 ^{B,WFS}	13.32±0.15 ^{CPS2} 13.27 ^{B,WFS}
ρR _{fuel} (mg/cm ²) from Y _{2n} /Y _{1n}	≤ (18±2)	≤ (15±2)	≤ (15±2)	≤ (14±2)	≤ (16±1)
ρR _{fuel} (mg/cm ²) from Y _{2p} /Y _{1n}	≥ (8±2) ^{WFS}	≥ (7±2) ^{WFS}	≥ (7±2) ^{WFS}	≥ (6±2) ^{WFS}	≥ (6±1) ^{CPS2} ≥ (7±1) ^{WFS}
ρR _{total} (mg/cm ²) from <E _{2p} >	55 ^{B, WFS}	52 ^{B, WFS}	56 ^{B, WFS}	55 ^{B, WFS}	53±6 ^{CPS2} 54 ^{B, WFS}

^{CPS2}Measured with the magnet-based spectrometer CPS2.

^{WFS}Measured with a “wedge-range-filter” spectrometer.

^AStatistical errors are much smaller, but a 20% uncertainty is assumed because of known spatial nonuniformities (see pg. 138).

^BStatistical errors are very small, but systematic calibration errors have not been quantified (see pg. 138).

for physical parameters. The measured ratios Y_{2p}/Y_{1n} can be used to estimate ρR_{fuel} , with the information in Fig. 83.17, subject to two caveats. First, preliminary numerical simulations have suggested that any mixing at the shell–fuel boundary may result in an increase in secondary-neutron yield for a given ρR_{fuel} , meaning that the values in Fig. 83.17 could give us a value of ρR_{fuel} that is too high. For this reason, we will interpret our secondary-neutron-derived values of ρR_{fuel} as upper limits. Second, the results are slightly dependent on assumptions we make about temperature and density in the fuel. We know from neutron measurements that the ion temperatures are slightly higher than 3 keV; we assume the electron temperatures are the same. The mass density can't be determined directly, but we will find that the maximum possible value of ρR_{fuel} for these shots is about 18 mg/cm². This information can be used with the capsule dimensions and fill pressure to estimate that ρ is unlikely to exceed 10 g/cm³. Inferred ρR_{fuel} increases slowly with increasing assumed ρ here, so using this upper limit on density will once again give us an upper limit on ρR_{fuel} . Since we don't know whether the radial profiles correspond more nearly to a uniform or hot-spot model, we can choose the larger results of the uniform model as an upper limit. Under these assumptions, we calculate upper limits on ρR_{fuel} in our four individual shots of 14 to 18 mg/cm², as listed in Table 83.I.

The measurements of Y_{2p}/Y_{1n} can also be used in conjunction with Fig. 83.17 to study ρR_{fuel} . In this case, there are reasons to interpret our results as lower limits. First, the values of Y_{2p}/Y_{1n} are very close to saturation. Second, preliminary work indicates that mixing at the shell–fuel boundary may sometimes result in a small decrease in secondary-proton yield for a given ρR_{fuel} , meaning that Fig. 83.17 could give us an inferred value of ρR_{fuel} that is too low. We therefore quote values from the hot-spot model (which gives lower numbers than the uniform model), using again the upper limit on ρ of 10 g/cm³ (inferred ρR_{fuel} decreases slowly with increased assumed ρ here). The resulting lower limits for our shots fall in the interval from 6.3 to 8 mg/cm², as indicated in Table 83.I. These values are very similar to values for DT-filled capsules with similar shells and fill pressures, using CPS-measured spectra of knock-on particles.¹⁰

2. Energy Shift and ρR_{total}

The energy shift of a measured spectrum, relative to the birth spectrum, is due to proton slowing in both D fuel and CH shell. Figure 83.16 shows that the proton stopping powers normalized to ρ are almost the same for both D and CH, and in the vicinity of the birth energies of the protons there is little

variation with plasma temperature for $T_e < 3$ keV. In addition, it will turn out that the shell ρR dominates the total ρR and that the amount of slowing down in the fuel is small. We therefore estimate ρR_{total} from the shift in mean energy by using the relationship for CH described in Fig. 83.23 and its caption, together with parameters appropriate for the shell. The result is weakly dependent on electron temperature and density in the shell, and we assume that $T_e = (1 \pm 0.5)$ keV and $\rho = (20 \pm 10)$ g/cm³. These assumptions, together with the assumptions behind Fig. 83.23, lead to the inferred values of ρR_{total} shown in Table 83.I, which are all in the vicinity of 55 mg/cm². We note that this is similar to values measured for D-³He–filled capsules and DT-filled capsules with similar shells and fill pressures.^{9,10}

3. Future Improvements

Future data-interpretation work will involve more-detailed analytical and numerical modeling and the utilization of more information from proton spectra. The WFS-measured spectra for single shots are clean enough to allow detailed comparisons of spectrum shapes with model predictions. The important fact is that the combination of neutron and proton measurements provides a strong set of constraints that must be addressed in any complete model of the physics of capsule behavior.

Conclusions

We have shown the first detailed measurements of secondary-proton spectra from D₂-filled capsules in ICF experiments and demonstrated that charged-particle spectrometry can be used to provide useful diagnostic information about D₂-filled capsules in OMEGA. The energy downshift of a spectrum is directly related to the total areal density of the capsule, and the secondary-proton yield gives diagnostic information about fuel parameters such as the fuel areal density (especially in conjunction with primary- and secondary-neutron yields).

This first feasibility demonstration is particularly important because measurement of secondary-proton spectra may be the only diagnostic method for studying the areal densities of imploded, cryogenic D₂ capsules if ρR_{fuel} exceeds the limit for usefulness of secondary-neutron measurements (of the order of 0.1 g/cm², as shown in Figs. 83.17 and 83.24). It is expected that cryogenic, D₂-filled capsules will be imploded on OMEGA in the near future. Estimates of total areal densities, made from 1-D simulations, are as high as 0.2 to 0.3 g/cm². Under such circumstances, the measurement of secondary-proton spectra will still be possible with the techniques described here (and the increased yields will substantially decrease the statistical errors). This can be seen in Fig. 83.24, which

indicates the range of conditions under which the protons will escape the capsule and be measurable.

ACKNOWLEDGMENT

We thank Brock Bose for assistance in scanning CPS2 data. The work described in this article was performed in part at the LLE National Laser Users' Facility (NLUF) and was supported in part by U.S. Department of Energy Contract Number DE-FG03-99SF21782, LLE subcontract number PO410025G, LLNL subcontract number B313975, and the U.S. Department of Energy Office of Inertial Confinement Fusion under Cooperative Agreement No. DE-FC03-92SF19460. Part of this work was also performed under the auspices of the U.S. Department of Energy by University of California Lawrence Livermore National Laboratory under contract No. W-7405-Eng-48.

REFERENCES

- H. D. Campbell and F. H. Southworth, in *1st Topical Meeting on the Technology of Controlled Nuclear Fusion* (American Nuclear Society, Hinsdale, IL, 1974), pp. 75–76.
- E. G. Gamalii *et al.*, JETP Lett. **21**, 70 (1975).
- S. Skupsky and S. Kacenjar, J. Appl. Phys. **52**, 2608 (1981).
- T. E. Blue and D. B. Harris, Nucl. Sci. Eng. **77**, 463 (1981).
- T. E. Blue *et al.*, J. Appl. Phys. **54**, 615 (1983).
- H. Azechi *et al.*, Appl. Phys. Lett. **49**, 555 (1986).
- H. Azechi, M. D. Cable, and R. O. Stapf, Laser Part. Beams **9**, 119 (1991).
- M. D. Cable and S. P. Hatchett, J. Appl. Phys. **62**, 2233 (1987).
- C. K. Li, D. G. Hicks, F. H. Séguin, J. A. Frenje, R. D. Petrasso, J. M. Soures, P. B. Radha, V. Yu. Glebov, C. Stoeckl, D. R. Harding, J. P. Knauer, R. L. Kremens, F. J. Marshall, D. D. Meyerhofer, S. Skupsky, S. Roberts, C. Sorce, T. C. Sangster, T. W. Phillips, M. D. Cable, and R. J. Leeper, Phys. Plasmas **7**, 2578 (2000).
- C. K. Li *et al.*, “Study of Direct-Drive, DT-Gas-Filled-Plastic-Capsule Implosions Using Nuclear Diagnostics on OMEGA,” to be submitted to Physics of Plasmas.
- T. R. Boehly, D. L. Brown, R. S. Craxton, R. L. Keck, J. P. Knauer, J. H. Kelly, T. J. Kessler, S. A. Kumpan, S. J. Loucks, S. A. Letzring, F. J. Marshall, R. L. McCrory, S. F. B. Morse, W. Seka, J. M. Soures, and C. P. Verdon, Opt. Commun. **133**, 495 (1997).
- R. D. Petrasso, C. K. Li, M. D. Cable, S. M. Pollaine, S. W. Haan, T. P. Bernat, J. D. Kilkenny, S. Cremer, J. P. Knauer, C. P. Verdon, and R. L. Kremens, Phys. Rev. Lett. **77**, 2718 (1996).
- C. K. Li and R. D. Petrasso, Phys. Rev. Lett. **70**, 3059 (1993).
- S. Glasstone and R. H. Lovberg, *Controlled Thermonuclear Reactions: An Introduction to Theory and Experiment* (Van Nostrand, Princeton, NJ, 1960), Chap. 2.
- F. J. Marshall, J. A. Delettrez, R. Epstein, V. Yu. Glebov, D. R. Harding, P. W. McKenty, D. D. Meyerhofer, P. B. Radha, W. Seka, S. Skupsky, V. A. Smalyuk, J. M. Soures, C. Stoeckl, R. P. Town, B. Yaakobi, C. K. Li, F. H. Séguin, D. G. Hicks, and R. D. Petrasso, Phys. Plasmas **7**, 2108 (2000).
- D. G. Hicks, “Charged Particle Spectroscopy: A New Window on Inertial Confinement Fusion,” Ph.D. thesis, Massachusetts Institute of Technology, 1999.
- D. G. Hicks, C. K. Li, R. D. Petrasso, F. H. Séguin, B. E. Burke, J. P. Knauer, S. Cremer, R. L. Kremens, M. D. Cable, and T. W. Phillips, Rev. Sci. Instrum. **68**, 589 (1997).
- F. H. Séguin *et al.*, “A Proton Spectrometer Based on a Wedge-Shaped Range Filter and CR-39 Nuclear Track Detectors,” to be submitted to Review of Scientific Instruments.
- J. A. Frenje *et al.*, “Charged Particle Measurements in DD, $D^3\text{He}$, and DT Implosions at the OMEGA Laser Facility Using Diagnostic Techniques Based on CR-39 Track Detection,” to be submitted to Review of Scientific Instruments.
- S. Skupsky and R. S. Craxton, Phys. Plasmas **6**, 2157 (1999).
- D. G. Hicks *et al.*, “Charged-Particle Acceleration and Energy Loss in Laser-Produced Plasmas,” to be published in Physics of Plasmas.
- P. B. Radha, J. A. Delettrez, R. Epstein, S. Skupsky, J. M. Soures, S. Cremer, and R. D. Petrasso, Bull. Am. Phys. Soc. **44**, 194 (1999).

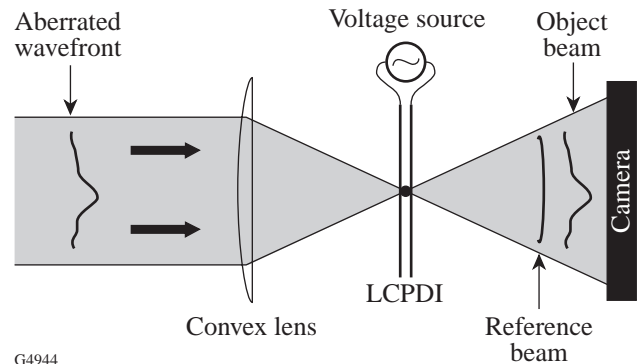
Comparison of a Liquid Crystal Point-Diffraction Interferometer and a Commercial Phase-Shifting Interferometer

Introduction

Fusion-class lasers, such as OMEGA, typically require hundreds, or even thousands, of high-performance optical elements ranging in diameter from several millimeters to tens of centimeters. To obtain high irradiation uniformity required for direct-drive ICF, it is critical that (1) the optical performance of these elements and associated optical subsystems be well characterized before being installed in the laser, and (2) their high performance be maintained throughout their lifetime in the laser system. Commercially available Fizeau phase-shifting interferometers¹ with aperture sizes of between 4 and 18 in. have been used to characterize the laser beam wavefront before optical elements are installed on OMEGA. Although these interferometers have high sensitivity, their expense and susceptibility of the measurement to environmental disturbance scale significantly with aperture size. Once optical elements are installed into OMEGA, wavefront characterization of OMEGA beamlines is performed at $\lambda = 1054$ nm with a shearing interferometer,² but the method suffers from (1) an inability to perform gradient measurements in more than two directions, (2) a sensitivity to only low-order phase errors, and (3) low spatial resolution. We have investigated the use of a phase-shifting, point-diffraction interferometer (PDI) both as a replacement to the shearing interferometer and as a low-cost alternative to commercially available phase-shifting interferometers.

The PDI^{3,4} is an elegantly simple device that consists of a pinhole, upon which a laser beam under test is focused, and a region of high optical density surrounding the pinhole, which is used to attenuate a portion of the incident beam. Light diffracted from the pinhole generates a reference wavefront, while light that propagates around the pinhole is the object beam under test. Interference fringes of high contrast are obtained by attenuating the object beam such that object and reference beam intensities are nearly equal. A distinct advantage of the PDI design is its truly common-path nature, i.e., both object and reference beams follow the same path as opposed to two different paths, such as in the Mach-Zehnder, Michelson, or Fizeau interferometers.⁵ This attribute makes

the PDI an attractive alternative to other interferometers for several reasons: (1) sensitivity to environmental disturbances such as mechanical vibration, temperature fluctuations, and air turbulence is reduced; (2) very short coherence length lasers can be used, without the need for path-length-adjusting optics to maintain high fringe visibility; and (3) fewer optical elements are required, reducing the size and cost of the instrument. Several modifications of the PDI to incorporate the phase-shifting technique are described in the literature;⁶ however, the liquid crystal point-diffraction interferometer (LCPDI), introduced by Mercer and Creath,^{7,8} is particularly attractive because of its simplicity, ease of use, and low manufacturing cost. The LCPDI maintains the advantages of the standard PDI, while providing an ability to phase-shift the object beam wavefront relative to the reference wavefront. It is a modification of the PDI, where the pinhole that generates the reference wavefront is replaced by a glass or plastic microsphere that is embedded within a nematic liquid crystalline “host” (see Fig. 83.29). A voltage applied to the liquid crystal (LC) cell



G4944

Figure 83.29

Schematic diagram of the liquid crystal point-diffraction interferometer (LCPDI). The laser beam is focused onto an area of the device containing a glass or plastic microsphere in the LC fluid gap that takes the place of the pinhole in the standard point-diffraction interferometer (PDI). The portion of the beam passing through the microsphere forms the reference wavefront of the interferometer, and light passing around the microsphere forms the object beam under test. Phase-shifting is accomplished through the application of an electric field to the LCPDI, as described in Fig. 83.30.

causes a phase shift of the object beam relative to the diffracted reference beam by an effective refractive index change of the LC. A “guest” dye that is added to the liquid crystalline host improves fringe contrast by attenuating the object beam intensity. Notably, the phase-shifting LCPDI was shown by Mercer and Rashidnia to be significantly more robust when compared with a phase-shifting Mach–Zehnder interferometer.⁹

We compared a visible-wavelength LCPDI to a commercially available, Mark IV XP Fizeau phase-shifting interferometer¹⁰ and found that LCPDI measurements of a witness sample were in close agreement with measurements of the same sample made using the commercially available interferometer. Two systematic, phase-shift error sources in the LCPDI that contributed to measurement discrepancies were (1) an intensity modulation from frame to frame caused by the dichroism of the dye⁸ and, to a lesser extent, (2) molecular alignment distortions of the host liquid crystal around the microsphere.¹¹ These phase-shift errors currently produce a spatially dependent accuracy in the LCPDI that, in some regions, closely compares with the Mark IV, but departs from the Mark IV measurements by approximately 50 nm in regions of highest systematic error. A smaller departure of the measurement from that of the Mark IV at higher spatial frequencies was due to interference effects caused by residual reflections between the CCD array and the final imaging lens. By modifying LCPDI fabrication parameters and through judicious choice of phase acquisition and analysis methods, these systematic errors can be significantly reduced.

LCPDI Construction

LCPDI cells were fabricated with liquid crystal Merck E7, a eutectic composition of rodlike molecules that has a nematic phase at room temperature. The long axes of the molecules in the nematic phase have a preferred orientation characterized by a unit vector called the *director*. A thin film of nylon or polyimide was applied to the inner surfaces of indium-tin oxide (ITO)-coated glass substrates and subsequently buffed unidirectionally, causing the director to preferentially lie in the plane of the substrates. Long-range orientational order, which is homogeneous and coincides with the direction of the crystal optic axis, is thereby imparted to the molecules. The means by which the LCPDI phase shifts is shown conceptually in Fig. 83.30. For a homogeneously aligned nematic LC with molecular axis parallel to the cell walls, linearly polarized light along the long axis of the molecule in Fig. 83.30 will see extraordinary refractive index n_e . As voltage is applied to the cell, the LC molecules will reorient, as shown. The effective refractive index approaches the value of the ordinary refractive

index n_o when the molecules in the bulk of the fluid are nearly perpendicular to the cell walls. Cell parameters that determine the maximum phase shift are primarily the LC birefringence and fluid path length, assuming that the microsphere diameter and fluid path length are equal. If the microsphere diameter is less than the path length of the cell, phase modulation will be less. In addition, strong anchoring of interfacial LC molecules to the cell walls prevents complete reorientation of the director throughout the fluid path length, resulting in an effective refractive index that is somewhat less than n_o .

Fluid path lengths and microsphere diameters of either 10 or 20 μm were used, and cell gap was maintained by placement of fiber spacers or glass microspheres at the outer edges of the cell. The use of fiber spacers instead of glass microspheres at the corners of the device improved cell gap uniformity and reduced wedge across the clear aperture of the LCPDI device. Glass substrates, 2.4 cm \times 2.8 cm \times 1 mm thick, had inner walls that were coated with electrically conductive ITO prior to application of the alignment layer. We determined that in this application polyimide alignment layers offer an advantage over nylon layers because (1) they are more resistant to scratches that can be produced while manipulating the microspheres during assembly, and (2) they are easier to spin-deposit and buff, yielding devices with higher alignment

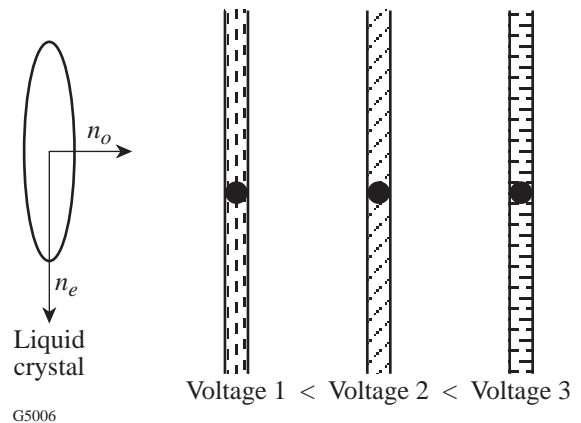


Figure 83.30

An electric field applied to the LCPDI produces a controlled reorientation of the birefringent LC molecules, thereby shifting the phase of the object wavefront relative to the reference wavefront. Light that is polarized along the buff direction of the cell will first see extraordinary refractive index n_e , followed by refractive index values approaching the ordinary refractive index n_o as voltage is applied. Attenuation of the object beam intensity by adding a “guest” dye to the LC fluid “host” allows high-contrast fringes to be obtained.

quality and contrast. Antiparallel buffing on opposing substrate surfaces generally provided better alignment quality than parallel-buffed surfaces. Bonding the wire leads to the devices with conductive epoxy *before* rather than after filling with LC eliminated the infiltration of air into the devices caused by the expansion and contraction of the fluid-filled cell during the epoxy thermal cure process. Visible-wavelength absorbing dye, Oil Red O, at 1% wt/wt concentration, was used for the device designed to operate at $\lambda = 543$ nm and produced an optical density of 2.1 in a 10- μm -path-length cell with no voltage applied. The blocking extinction, or optical density (OD), of this cell at $\lambda = 543$ nm with light polarized along the buffing direction as a function of applied voltage is shown in Fig. 83.31. Because of the absorption dichroism of the dye, the OD of the cell varied between 2.1 and 0.8 as voltage was raised from 0 to 6 V (rms) using a 2-kHz sine wave.

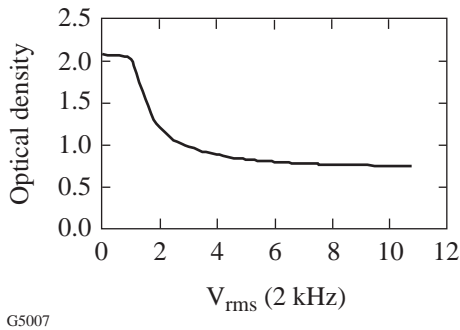


Figure 83.31 Absorbance at $\lambda = 543$ nm of the LCPDI with 1% wt/wt concentration of Oil Red O dye in the nematic E7 host LC as a function of voltage applied to the device. The dichroism of the dye produces voltage-dependent changes in fringe intensity and contrast.

Microspheres were placed in the cell using one of two different techniques: In the first method, a large quantity of microspheres were spin deposited onto one of the substrate surfaces before the cell was assembled. This ensured that a microsphere could later be found that would phase modulate satisfactorily upon optical testing and was quite easy to do compared with the manual deposition technique described below. A disadvantage of this approach is the possibility of microsphere agglomeration resulting in optical interference from adjacent microspheres during device testing. The current device assembly protocol calls for a single microsphere to be placed manually in the center of the substrate using a high-power microscope. In this method, the sphere is positioned using a single fiber from a camel's-hair brush. Custom assembly tooling helps to keep the two substrates in registration with each other as they are lowered to help eliminate the scratching

of the alignment coating caused by microsphere displacement when the substrates are inadvertently sheared. We have found that the use of glass microspheres rather than plastic ones as the central element reduces the number of scratches in the alignment coating caused by movement of the central sphere during device assembly operations. Plastic spheres also had a slightly elliptical appearance in some cells and showed a uniaxial conoscopic figure, likely due to stress-induced birefringence imparted by the substrates during cell fabrication and epoxy cure. The custom tooling used to maintain substrate registration remedied this by preventing excessive force from being applied during the assembly operation.

Test Sample Measurements

The LCPDI cell used for these measurements had a glass microsphere diameter and fluid gap of 10 μm and was placed in the experimental setup shown in Fig. 83.32. The $\lambda = 543$ -nm HeNe laser beam was spatially filtered and up-collimated to slightly overfill a 1-in.-diam $f/16$ doublet lens used to focus the beam into the LCPDI. A Tamron SP60 300-mm telephoto zoom lens was used to image the cavity region to the CCD camera. The beam diameter at the focus of the doublet was 41 μm at $1/e^2$ of peak intensity, as measured with a scanning slit. The intensity onto the LCPDI was adjusted, and linear polarization was maintained along the extraordinary axis of the LC by using two polarizers placed before the spatial filter. Fringe data were acquired through a sequence of five images, each shifted incrementally in phase by a relative amount $\pi/2$, and resultant phase ϕ computed using the five-frame algorithm^{8,12,13}

$$\tan(\phi) = \left(\frac{\Delta I_3 - \Delta I_1}{\Delta I_0 + \Delta I_4 - 2\Delta I_2} \right) \times \left(\frac{\sqrt{I_0^{\text{obj}}} + \sqrt{I_4^{\text{obj}}} + 2\sqrt{I_2^{\text{obj}}}}{\sqrt{I_3^{\text{obj}}} + \sqrt{I_1^{\text{obj}}}} \right), \quad (1)$$

where I_k^{obj} is the k th object beam intensity distribution and $\Delta I_k = I_k - I_k^{\text{obj}}$ is the k th interferogram in the five-frame sequence. Equation (1) is normalized to the intensity distribution of the object beam in order to reduce the effect of intensity and contrast changes caused by the dichroism of the dye, as described by Mercer.⁸ The object beam intensity was obtained by moving the LCPDI a short distance laterally so that the incident beam did not intersect the microsphere and by acquiring five frames of data at the same voltages used for acquiring interferometric phase data. Table 83.II gives a relative com-

parison of several different phase unwrapping algorithms that were tested with intentionally noisy data (i.e., low-contrast fringes with focus at the microsphere) in order to compare the robustness of the various unwrapping algorithms. In Table 83.II, the relative processing speed of these algorithms is compared to a simple path-dependent, linear algorithm that began at the edge of the CCD array and propagated unacceptably large unwrapping errors throughout the array. The large residual errors for the algorithms listed in the table are primarily from unwrapping errors at the edge of the CCD array. Although a tiled, path-dependent unwrapping algorithm that began in the center of the array, combined with a masking technique, produced the least phase error, the tiled algorithm

was chosen without masking because it required significantly less processing time and had only marginally greater residual error. Data acquisition was automated using a personal computer, in-house data acquisition and analysis software, and graphical user interface. With no test sample in the cavity region between the collimating lens and the focusing doublet, several focus and voltage conditions were investigated, as described in Table 83.III. The least amount of residual phase error in empty cavity measurements was found in the low-voltage regime (<1.2-V rms at 2 kHz) with 3 to 4 fringes on the camera. Greater phase error was observed in the high-voltage regime (3.8 to 7 V) because of the loss of fringe contrast caused by the absorption dichroism of the dye.

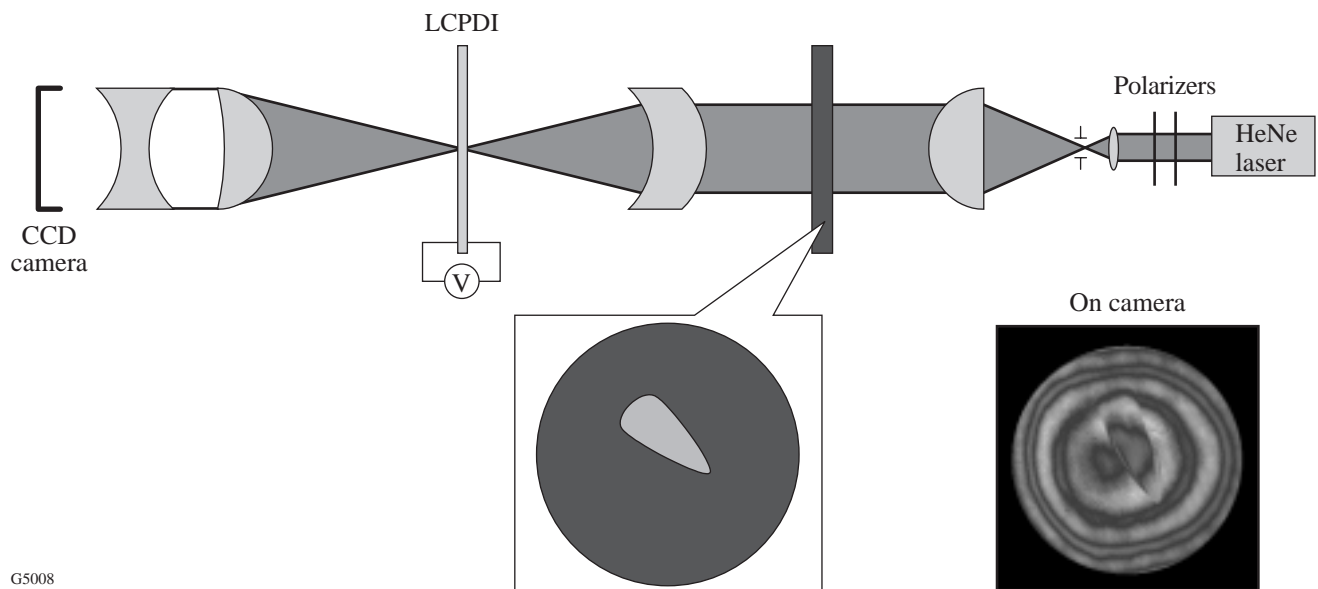


Figure 83.32 Experimental setup used for LCPDI measurements. The inset shows interference fringes from the test sample with an MRF-polished spot.

Table 83.II: Relative comparison of different unwrapping algorithms with intentionally noisy data (low-contrast fringes). Among the algorithms tested, the tile unwrapping algorithms showed the least number of unwrapping errors. The tile unwrapping algorithm with a tile size of 10×10 pixels was used for the experimental results reported.

	Centered Linear, Path Dependent	Box Mask and Linear, Path Independent	Tile Unwrap	Tile Unwrap and Box Mask
p-v (2π rad)	9.07	3.23	2.77	2.670
rms (2π rad)	0.45	0.13	0.10	0.094
Computation time (compared to standard unwrap starting at edge of array)	1:1	3:1	5:2	4:1

To characterize the empty cavity, two sets of ten phase measurements were taken approximately 5 min apart, the ten measurements averaged, and the two sets of phase averages subtracted to give residual peak-to-valley (p-v) and rms phase errors of 22 nm and 1.7 nm, respectively, as shown in Fig. 83.33. The quality of the interference fringes used for the five-frame sequence is shown in Fig. 83.33(a). As evident from the horizontal lineout in Fig. 83.33(b), a residual amount of tilt is present in the phase difference. With tilt removed, p-v and rms phase errors drop to 19 nm and 1.1 nm, respectively. The dominant phase error in Fig. 83.33(b) has a spatial period equal

to that of the interference fringes, suggesting that the effect of the dye has not been entirely eliminated through the use of Eq. (1). Also apparent in the phase image is an error term equal to twice the frequency of the fringes, indicating that there is some amount of phase-shift error related to the host LC in addition to the dye-induced error. Because these systematic error sources are present, their removal through subtraction of a reference phase requires stringent control of environmental parameters. Although air turbulence was reduced by placing a plastic enclosure around the setup in Fig. 83.32, the setup was not supported by an air-isolation table and was located in a

Table 83.III: Several focus and voltage conditions were investigated for the LCPDI in empty-cavity measurements.

Focus	<ul style="list-style-type: none"> - Close to best focus (1 to 2 fringes) - Intermediate focus position (3 to 4 fringes) - Far from best focus (8 to 9 fringes) - Off center (lateral movement of the LCPDI) - On center (no lateral movement)
Voltage (rms at 2 kHz)	<ul style="list-style-type: none"> - Low-voltage regime (0–1.21 V) - High-voltage regime (3.8–7 V)

Conditions giving least residual phase error: intermediate focus with low-voltage regime.

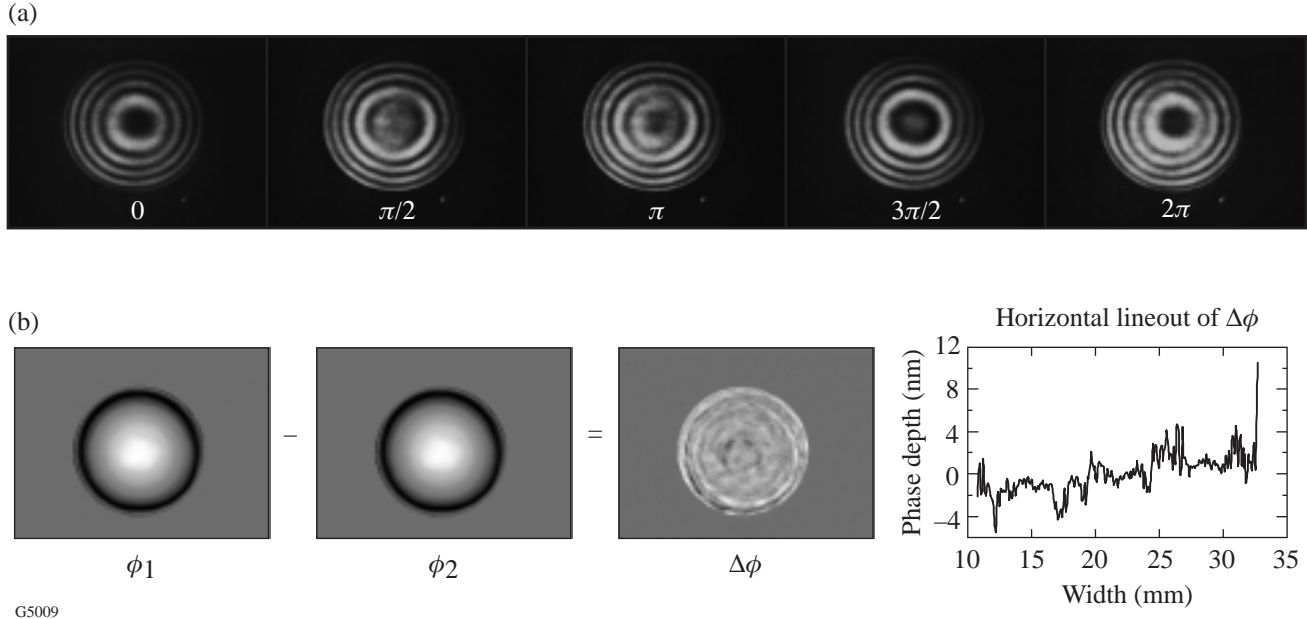


Figure 83.33

(a) LCPDI interference fringes obtained by phase-shifting through 2π rad, from 0.98 V (0) to 1.21 V (2π). (b) Two empty-cavity phase images ϕ_1 and ϕ_2 were subtracted to obtain the residual phase error $\Delta\phi$ in the LCPDI. The phase-difference image reveals phase-error contribution from both dye- and host-induced phase-shift error.

room without strict air-handling requirements. It is expected that more rigorous environmental standards and improvements to LCPDI packaging and mounting will significantly improve its precision. Further improvements to both accuracy and precision of the LCPDI can be achieved through removal or mitigation of systematic error sources, as discussed below.

A test object was next inserted into the cavity that consisted of a 2-in.-diam \times 0.25-in.-thick fused-silica wedged window with a central “spot” polished into the window using the magnetorheological finishing method (MRF).¹⁴ The geometry of the polished spot is characteristic of this technique and was well suited for this test because of the co-existence of steep and gradual gradient features (see Fig. 83.32). An empty-cavity phase measurement was subtracted from the phase measurement of the test object for all measurements reported here. In contrast to the empty-cavity measurements described previously, however, acquisition of both the test object phase and associated reference phase incorporated a $\pi/2$ phase-offset technique¹² that reduced residual phase-shift errors at twice the fringe frequency that were apparent in initial measurements of the test piece. In this method, ten phase measurements were acquired per Eq. (1) and averaged, followed by an additional set of ten phase measurements acquired with the first frame of the five-frame sequence offset in phase by $\pi/2$. Averaging the first set of ten measurements with the set of measurements acquired with $\pi/2$ offset produced the phase plot shown in Fig. 83.34. This figure shows that the LCPDI results are in close agreement with those from a 4-in.-aperture Zygo Mark IV XP operating at $\lambda = 633$ nm and located on an air-supported table in the Center for Optics Manufacturing (COM). The close comparison of the high gradient features on the left of the lineout is especially notable. The large peak on the right of the LCPDI lineout appears to approach a discrepancy of 100 nm, but it is near the edge of the aperture, where a valid comparison cannot be made because of the absence of Mark IV XP data. The remaining discrepancies on the right of the lineout are attributed to the following sources: (1) Phase-shift errors likely related to the dichroism of the dye produced an approximately 50-nm residual phase error at the same spatial frequency as the fringe pattern, which can be seen in the LCPDI phase image in Fig. 83.34. (2) The high-spatial-frequency ripple in the LCPDI lineout of Fig. 83.34 was caused by an interference pattern observed during data acquisition whose origin appeared to be multiple reflections between the zoom lens and the CCD array. (3) To a lesser extent, alignment distortions of the host LC molecules may also contribute residual phase-shift error, as discussed below. As noted previously, accounting for object beam intensity changes through

the use of Eq. (1) has not completely removed the phase error related to the absorption dichroism of the dye. The phase-offset method, however, reduced the appearance of LC host-induced phase-shift errors at twice the fringe frequency, although higher-order phase-shift error not compensated using this technique may still be present.¹⁵ Because the dominant error has periodicity equal to the interference fringes, the current LCPDI device incorporating the highly dichroic Oil Red O dye would be most useful for characterizing aberrations whose Zernike fit is not significantly affected by the presence of this error.

Discussion

1. Dye-Induced Measurement Error

The predominant phase error in Fig. 83.34 has a periodicity equal to that of the interference fringes, indicating that its most likely origin is an intensity change between phase shifts caused by absorption dichroism of the Oil Red O dye.⁸ The use of Eq. (1) significantly reduces the contribution of this effect to the phase error but does not eliminate it entirely. Equation (1) is exact provided that (1) the reference beam

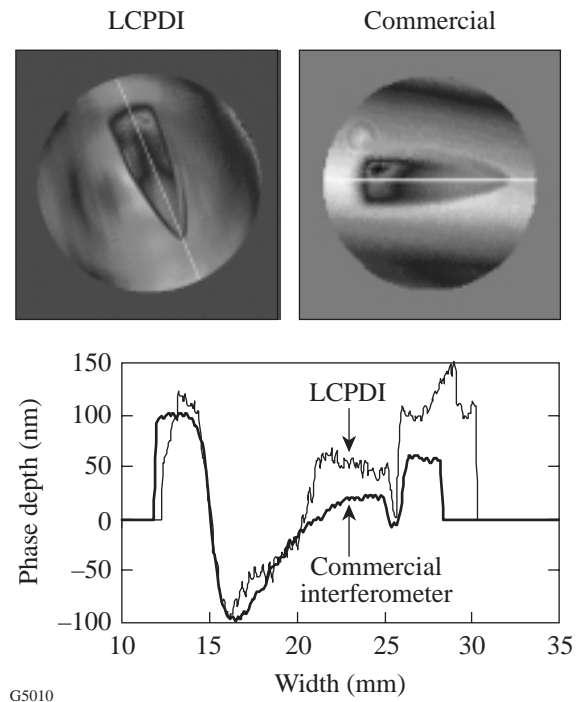


Figure 83.34 Phase measurements of a wedged window containing an MRF polishing spot comparing the LCPDI to a commercial interferometer (Zygo Mark IV XP). The LCPDI lineout matches that of the Zygo Mark IV in some areas and is ≤ 50 nm discrepant in other areas primarily due to the absorption dichroism of the dye used.

intensity remains constant with applied voltage and (2) the object beam intensity can be accurately measured. Although the object beam intensity is fairly well approximated using the procedure described above, a ray-trace model has shown that the intensity of the reference beam changes with voltage applied to the cell.^{16,17} This model has also indicated that refraction through the microsphere cannot produce sufficient intensity in the reference beam to obtain the experimentally observed high fringe contrast, and diffraction must also be considered.¹⁷ This suggests that by measuring fringe contrast and object-beam-intensity changes with voltage, it may be possible to accurately account for changes in reference beam intensity and thereby further reduce the phase error contributed by the absorption dichroism of the dye. Nonetheless, frame-to-frame absorbance changes in the LCPDI can be substantially reduced through the use of either a non-dichroic dye or a mixture of both positive and negative dichroic dyes. In Fig. 83.35, the absorbance as a function of wavelength for two such positive and negative dichroic dye combinations in E7 is shown for different voltages applied to the cell.¹⁸ Figure 83.35(a) shows that when the Oil Red O dye, having positive dichroism, was combined with a negative dichroic Orasol dye mixture, the OD at 543 nm in a 22- μm -path cell changed by only 0.03 as the voltage was increased from 0 to 5-V rms. This result represents a factor-of-40 improvement

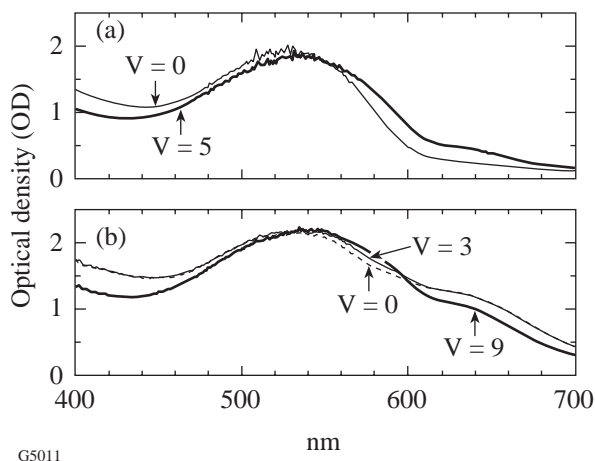


Figure 83.35

Absorbance (OD) of two different dye mixtures containing both positive and negative dichroic dye components in E7 shows very little change with applied voltage. Such mixtures can be used to significantly reduce phase-shift error in the LCPDI caused by the absorption dichroism of a single dye. (a) 1.3% Orasol Red BL, 0.55% Orasol Black RLI, + Oil Red O; (b) 1.3% Orasol Red BL, 0.55% Orasol Black RLI + 0.2% Sudan III, 0.38% Sudan Black B. In each case fluid path length was 22 μm .

compared with absorbance changes observed in the cell with the single dye component Oil Red O (compare with Fig. 83.31). An Orasol/Sudan dye mixture in Fig. 83.35(b) showed a change in OD of only 0.08 as voltage changed by 9-V rms. These results are summarized in Table 83.IV. We are currently in the process of purifying the Orasol dyes in order to reduce ionic conduction in the LC that has contributed to hydrodynamic-induced scattering observed in devices made with the new dye mixtures. Because the molecular structure of the Orasol dyes is not well known, the effect of these dyes on the long-range orientational order of the LC is currently unknown. Other visible-wavelength dye candidates with negative absorption dichroism that are expected to minimally perturb the liquid crystalline order parameter have also recently been identified.¹⁹ For applications at $\lambda = 1054 \text{ nm}$, LCPDI's fabricated using recently synthesized nickel dithiolene dyes with various terminal functional groups²⁰ also show significantly less intensity change as a function of voltage applied to the cell. It is anticipated that appropriate combinations of purified positive and negative dichroic dyes will substantially reduce, or even eliminate, the primary source of systematic error in the LCPDI.

2. LC Host-Induced Measurement Error

Although the long-range orientational order of the LC is homogeneous and planar, we have observed a distortion in the molecular alignment locally around the microsphere that is voltage dependent and can lead to phase-shift errors.¹¹ This alignment distortion is caused by a competition between anchoring forces on the surface of the sphere, the cell walls, and elastic forces of the LC.²¹ Viewed through a polarizing microscope with 100 \times magnification, the liquid crystal alignment around the microsphere has the appearance shown in Fig. 83.36. These images are of a 10- μm -diam silica micro-

Table 83.IV: Absorbance (OD) at 543 nm.

V (rms at 2 kHz)	Mixture A	Mixture B
0	1.854	2.13
1	—	—
3	—	2.2
5	1.823	—
9	—	2.21
A = 1.3% Orasol Red BL, 0.55% Orasol Black RLI, + ORO		
B = 1.3% Orasol Red BL, 0.55% Orasol Black RLI + 0.2% Sudan III, 0.38% Sudan Black B		

sphere within the 10- μm path cell of E7 with 1% wt/wt Oil Red O dye used for the comparison tests described in the previous section. The alignment perturbation has quadrupolar symmetry, most apparent at intermediate rms voltages (2.38 V and 3.9 V in Fig. 83.36). The buff direction of the cell can be seen as oriented diagonally from the lower left to the upper right of these images. Regions of director distortion that have the appearance of large “ears” and extend outward from the sphere in the buff direction can also be seen in these images. This alignment distortion is enhanced in a thicker, 20- μm path cell with 20- μm -diam glass microspheres, shown in Fig. 83.37. In the thicker cell, the planar anchoring force of the substrate walls has less effect in the bulk of the fluid, and the alignment perturbation at intermediate voltages is more pronounced than in the 10- μm path cell. The director distortion appearing as large ears in these images again extends parallel to the buff direction. In Figs. 83.36 and 83.37, the increased electric-field strength encountered at higher voltages imparts sufficient torque to the molecules to overcome the competing surface-anchoring forces and elastic distortions of the liquid crystal, and the perturbation becomes less severe.

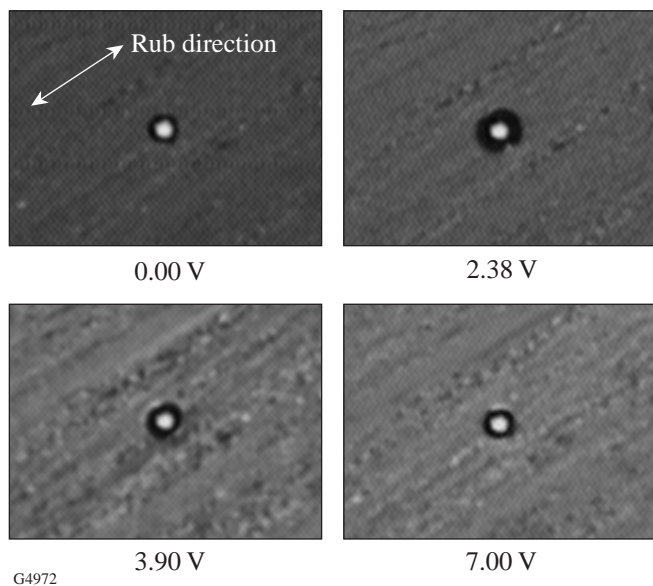


Figure 83.36

Polarizing microscope images of a 10- μm silica microsphere in 10- μm -path E7 host showing the quadrupolar alignment perturbation of the nematic director around the microsphere. This alignment perturbation produces a phase-shift error in the LCPDI that is dependent upon focusing conditions and the voltage applied to the cell. The quadrupolar symmetry is greatest at intermediate voltages, gradually becoming more circular with increasing electric-field strength. Voltage waveform was a 2-kHz sine wave.

The structures observed in Figs. 83.36 and 83.37 are similar to those described by other authors in the context of colloidal suspensions in nematic solvents^{22,23} and inverted nematic emulsions.^{21,24} The existence of planar or normal anchoring of the director to the sphere's surface plays a critical role in determining the director field configuration around the sphere²¹ as does the anchoring strength.²⁵ For strong anchoring conditions, topological defects are known to form at the sphere's surface in addition to director distortions in the region surrounding the sphere.²¹ With no voltage applied to the cell in Fig. 83.37, two such surface defects can be seen at the poles of the spheres that are diametrically opposed in a direction orthogonal to the long-range orientational order imposed by the substrates. We observed that altering the procedure by which the microspheres were applied to the surface of the substrates changed the topological orientation of the defects. In the images of Figs. 83.36 and 83.37, spheres were spin-deposited in a high-performance liquid chromatography-grade hexane solution onto one of the substrates, and the hexane was allowed to evaporate before the cells were filled with liquid crystal *via* capillary action. The alignment of the defects orthogonal to the rub direction of the substrates and the concomitant quadrupolar symmetry around the microsphere resemble structures characteristic of weak normal anchoring.²⁵ When a manual deposition method was used without hexane, however, the two surface defects appeared *along* the rub direction, providing evidence of planar anchoring at the surface of the sphere.²¹ The change in anchoring conditions is

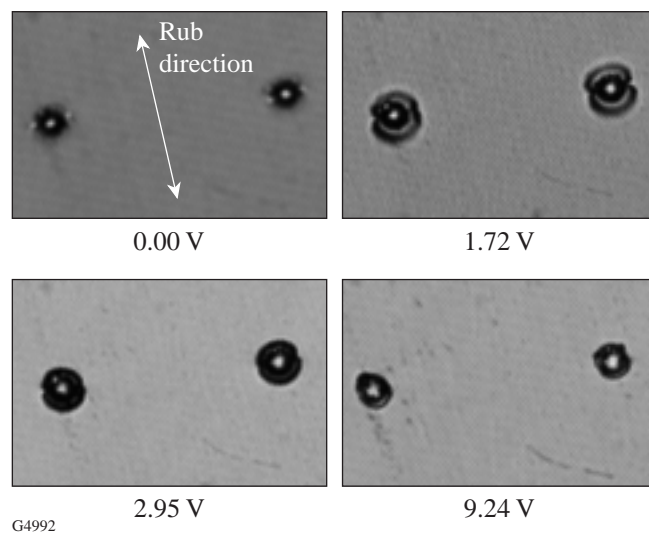


Figure 83.37

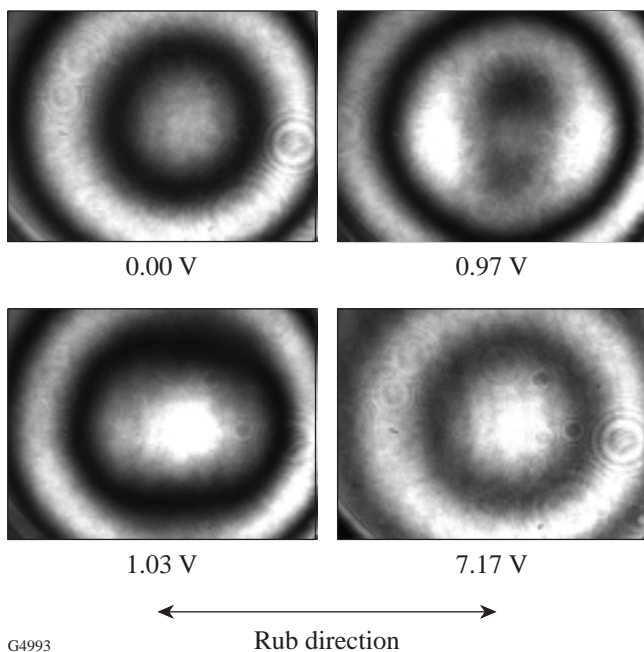
Polarizing microscope images of a 20- μm silica microsphere in 20- μm -path E7 host. The alignment distortion is enhanced, compared with the thinner LC cell of Fig. 83.36. Voltage waveform was the same as in Fig. 83.36

likely related to trace impurities that remained on the surface of the sphere after solvent evaporation since no attempt was made to further purify the hexane prior to use.

The effect of the quadrupolar alignment around the microsphere on a laser beam, when focussed close to the sphere, is clearly seen in Fig. 83.38. These interference fringes were obtained by using the setup shown in Fig. 83.32, and the small diffraction rings in Fig. 83.38 are from the final telephoto imaging lens. No measurable amount of light was observed to couple into the orthogonal polarization due to localized director distortions. Because the dye molecules rotate with the liquid crystal molecules, the dichroism of the Oil Red O dye in this cell may also have a contributing effect on the intensity and contrast changes observed. Focusing at a greater distance from the sphere produced fringes where the quadrupolar symmetry was less evident, as shown in Fig. 83.39. The loss of contrast caused by lower dye absorption of the object beam intensity can be clearly seen at 7.17 V in Fig. 83.39. As in Figs. 83.36 and 83.37, the effect of director distortions on the fringes in Figs. 83.38 and 83.39 is greatest at intermediate voltages. As the size of the Airy disk becomes increasingly larger compared with the size of the diffracting region, the reference wavefront

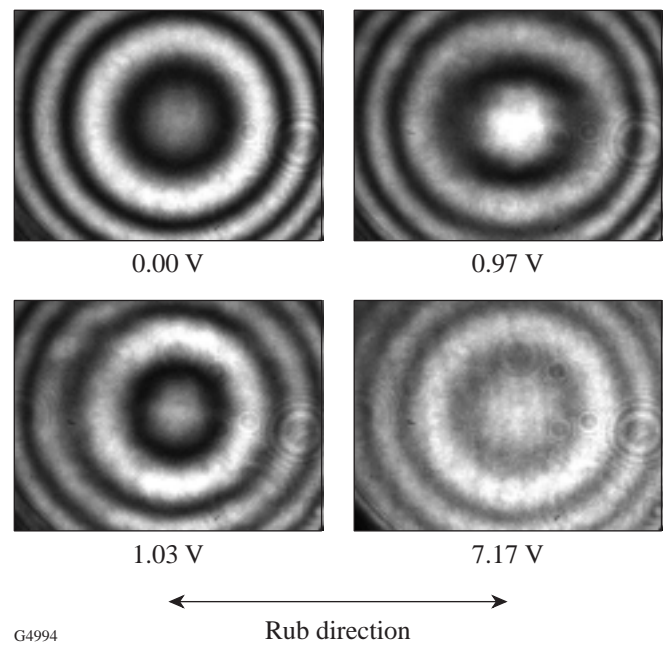
becomes increasingly spherical,⁸ with the optimum focusing condition for this device shown in Fig. 83.33(a).

These director distortions produce a phase-shift error that is both spatially nonuniform and nonlinear and can contribute significant residual phase error when the focus is placed very close to the microsphere. We have investigated the use of phase-shift algorithms designed for nonlinear and spatially nonuniform phase shifts, such as described by Hibino *et al.*,²⁶ to reduce these errors in the LCPDI. As described below, a six-frame algorithm designed to reduce the contribution of higher-order nonlinearity in the phase shift generally did not experimentally produce lower residual phase error than the five-frame algorithm produced. To explore the cause of this result, we have empirically derived a general form of the LCPDI phase-shift error with which we have compared the ability of each algorithm to reduce the contribution of director distortions to the phase measurement. A comparison of the residual phase error produced using these two algorithms in the absence of absorption dichroism was performed by subtracting a reference phase image created using error-free simulated fringes from the simulated phase image generated using the empirically derived phase-shift error.



G4993

Figure 83.38
Interference fringes obtained by focusing a 543-nm laser beam at $f/16$ into the LCPDI of Fig. 83.36, revealing the effect of director distortions having quadrupolar symmetry.



G4994

Figure 83.39
Interference fringes as in Fig. 83.38, but with displaced focal position. Quadrupolar symmetry is less evident at intermediate voltages than in Fig. 83.38. Loss of contrast due to dichroism of the Oil Red O dye molecules is observed at high voltage.

Neglecting frame-to-frame intensity and contrast changes, the intensity $I(x, y, \alpha_r)$ of each frame of data can be written as

$$I(x, y, \alpha_r) = I_0(x, y) \left\{ 1 + \gamma(x, y) \cos[\alpha_r - \phi(x, y)] \right\}$$

for $r = 1, 2, \dots, m$, (2)

where $I_0(x, y)$ is the mean intensity, γ is the interference fringe visibility, α_r is the phase shift at each discrete frame r , ϕ is the phase of the wavefront being measured, and m is the total number of frames. Here the phase-shift parameter α_r is spatially nonuniform and changes nonlinearly from frame to frame. Following Ref. 26, α_r can be given by a polynomial expansion of the unperturbed phase-shift value α_{0r} as

$$\begin{aligned} \alpha_r &= \alpha_{0r} \left[1 + \varepsilon(\alpha_{0r}) \right] \\ &= \alpha_{0r} \left[1 + \varepsilon_1(x, y) + \varepsilon_2(x, y) \frac{\alpha_{0r}}{\pi} + \varepsilon_3(x, y) \left(\frac{\alpha_{0r}}{\pi} \right)^2 \right. \\ &\quad \left. + \dots + \varepsilon_p(x, y) \left(\frac{\alpha_{0r}}{\pi} \right)^{p-1} \right] \end{aligned}$$

for $r = 1, 2, \dots, m$, (3)

where p ($p \leq m-1$) is the maximum order of the nonlinearity, ε_q ($1 \leq q \leq p$) are the error coefficients, which can be spatially nonuniform, and $\alpha_{0r} = 2\pi[r - (m+1)/2]/n$ is the unperturbed phase shift with n equal to an integer. For the five-frame algorithm in Eq. (1), for example, $m = 5$, $n = 4$, and the unperturbed phase shifts are therefore

$$\begin{aligned} \alpha_{01} &= -\pi, \\ \alpha_{02} &= -\pi/2, \\ \alpha_{03} &= 0, \\ \alpha_{04} &= \pi/2, \\ \alpha_{05} &= \pi. \end{aligned} \quad (4)$$

The offset value $(m+1)/2$ was introduced in Ref. 26 for convenience of notation and adds only a spatially uniform piston term to the calculated phase when no phase-shift error is introduced. In the simulation that follows, the functional form of the phase-shift error and the starting phase value were

chosen to closely represent the experimentally observed phase-shift error. Equation (1) can correct for linear phase-shifter miscalibration (i.e., $p = 1$) that is spatially nonuniform but is sensitive to the effect of spatial nonuniformity for higher orders of phase-shift error.²⁶ The six-frame algorithm [Eq. (39)]²⁶ given by

$$\tan \phi = \frac{\sqrt{3}(5I_1 - 6I_2 - 17I_3 + 17I_4 + 6I_5 - 5I_6)}{I_1 - 26I_2 + 25I_3 + 25I_4 - 26I_5 + I_6} \quad (5)$$

has greater immunity to both linear and quadratic nonlinearity ($p = 2$) of the phase shift that is spatially nonuniform. For this algorithm, the phase-shift interval is $\pi/3$, and $m = n = 6$. For both the five- and six-frame algorithms given by Eqs. (1) and (5), respectively, the phase ϕ was calculated using fringes simulated with Eq. (2), where the object beam intensity in Eq. (1) was taken as constant from frame to frame. As noted previously, a comparison of the residual phase error from these two algorithms was performed by subtracting a reference phase image ϕ_{ideal} , created by using error-free simulated fringes, from the phase image $\phi_{\text{perturbed}}$, generated using the empirically derived phase-shift-error coefficient

$$\varepsilon(\alpha_{0r}) = H \exp[-A\alpha_{0r}] \times f(x, y), \quad (6a)$$

where α_{0r} is the unperturbed phase shift and the spatial nonuniformity is given as

$$\begin{aligned} f(x, y) &= \left[1 - \exp(-|Bx^2 + Cy^2|) \right] \\ &\quad \left\{ \exp \left[-|(Dx^2 + Ey^2)^{1/2}/F|^G \right] \right\} \\ &\quad \times \left| \sin \left[\tan^{-1}(Kx/My) \right] \right|, \end{aligned} \quad (6b)$$

where $A-M$ are constants. The phase shift used in generating $\phi_{\text{perturbed}}$ was calculated by combining Eqs. (6) and (3):

$$\alpha_r = \alpha_{0r} \left[1 + H \exp(-A\alpha_{0r}) \times f(x, y) \right]. \quad (7)$$

Figure 83.40 shows the general form of $f(x, y)$ and the peak value of the phase error in Eq. (7) as a function of α_{0r} for one set of constants $A-M$ with $A > 0$. The functional form of this phase error is qualitatively similar to the director distortion observed in Figs. 83.36 and 83.37; the interference fringes in

Fig. 83.41, simulated using Eqs. (2) and (7) and used to obtain $\phi_{\text{perturbed}}$, are similar in appearance to those in Figs. 83.38 and 83.39. It is likely that some of the experimentally observed spatial variations in fringe intensity and contrast when focused close to the microsphere can be attributed to spatially nonuniform absorbance caused by orientational coupling between the dye molecules and liquid crystal molecules. We have not attempted here to model dye-induced absorbance changes that may affect fringe intensity and contrast. The image containing the residual phase error is thus given as

$$\Delta\phi = \phi_{\text{perturbed}} - \phi_{\text{ideal}}. \quad (8)$$

By expanding the exponential term in Eq. (7) and comparing with Eq. (3), it can be shown that the linear and quadratic error terms are, respectively,

$$\begin{aligned} \varepsilon_1 &= Hf(x, y), \\ \varepsilon_2 &= -AH\pi f(x, y), \end{aligned} \quad (9)$$

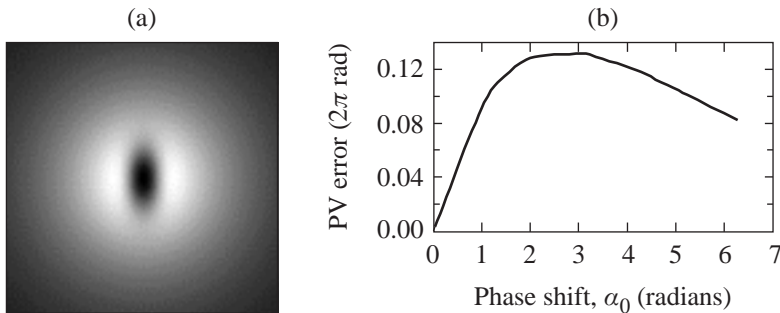
and Eq. (7) can be approximated by

$$\begin{aligned} \alpha_r &= \alpha_{0r} [1 + \varepsilon(\alpha_{0r})] \\ &\approx \alpha_{0r} \left[1 + \varepsilon_1(x, y) + \varepsilon_2(x, y) \frac{\alpha_{0r}}{\pi} \right] \end{aligned} \quad \text{for } r = 1, 2, \dots, m, \quad (10)$$

where $\varepsilon_1(x, y)$ and $\varepsilon_2(x, y)$ are given by Eq. (9). The ability of this approach to determine which algorithm would experimentally show better immunity to LCPDI phase-shift errors in the

absence of absorption dichroism was first tested theoretically using Eq. (10) with spatially uniform error coefficients ε_1 and ε_2 [i.e., $f(x, y) = 1$]. Table 83.V compares these results with the results of Hibino *et al.*²⁶ The residual errors shown in this table for the six-frame algorithm matched those of Ref. 26, and this algorithm performed significantly better than the five-frame algorithm when the quadratic phase-shift error shown in the table was introduced. The six-frame algorithm also produced less residual phase error when the spatially nonuniform error term given by Eq. (6b) was included in the simulated phase plots. When the phase error was exponentially increasing (i.e., $\varepsilon_1, \varepsilon_2 > 0$), the six-frame algorithm consistently yielded less residual error than the five-frame algorithm. When $\varepsilon_2 < 0$, however, the five-frame algorithm generally yielded less residual error. Table 83.VI gives a relative comparison of the algorithms using spatially nonuniform ε_1 and ε_2 given by Eq. (9) for both positive and negative values of ε_2 . For the cases when $\varepsilon_2 < 0$, the sum of the phase-shift error terms in Eq. (10) yields an approximation to the shape of the curve shown in Fig. 83.40; the descriptive terms in Table 83.VI when $\varepsilon_2 < 0$ correspond to the different regions of this curve. Among the curve shapes listed in Table 83.VI, the “parabola” most closely approximates the observed LCPDI phase-shift error, and the five-frame algorithm gave less residual phase error in this case.

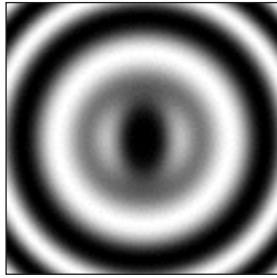
Residual phase errors from both algorithms using experimental fringes are compared in Table 83.VII with residual phase errors obtained using fringes simulated with the phase perturbation given by Eq. (7) and shown in Fig. 83.40. To avoid unwrapping errors observed when excessive phase error is introduced, an intermediate focusing regime that showed sufficient host-induced phase error was chosen for this test. Figure 83.42(a) compares two experimental interferograms from this series with their corresponding simulated interferograms. As shown in Table 83.VII, the five-frame algorithm produced lower residual rms phase error in both the experiment and the simulation by nearly the same factor. The larger p–v errors in



G5012

Figure 83.40

(a) Gray-scale image showing the spatial form of $f(x, y)$ defined in the text and used in Fig. 83.42. Black corresponds to $f(x, y) = 0$ with a maximum value of $f(x, y) = 1$. (b) Peak value of the phase-error function $\alpha_{0r} [\exp(-A\alpha_{0r}) f(x, y)]$ versus α_{0r} for the set of constants A – M given in Table 83.VII.



G5013

Figure 83.41
 Simulated interference fringes computed using the empirically derived form of the LC alignment perturbation given by Eq. (7) and the two-beam interference expression given by Eq. (2). The simulated fringes are similar in appearance to the experimental fringes in Figs. 83.38 and 83.39.

the experimental results are attributed to spurious phase spikes. The ideal phase image ϕ_{ideal} in the experimental data set was determined from a five-term Zernike fit to the final phase image $\phi_{perturbed}$; the phase difference $\Delta\phi = \phi_{perturbed} - \phi_{ideal}$ is shown in Fig. 83.42(b). To reduce the contribution of dye-induced absorbance changes, each intensity interferogram in the experimental data set was normalized by a reference intensity image obtained adjacent to the microsphere at the same voltage. In both the experimental and simulated fringes, the phase perturbation was observed to first increase, then decrease in amplitude as the phase was shifted through the requisite number of frames, corresponding to $A = 0.37$ and $H = 1.21$ in Eq. (7). For the experiment, the starting phase corresponded to a voltage close to the Frederiks transition threshold where very little perturbation in the fringes was

Table 83.V: Peak-to-valley residual phase errors (2π rad) that are due to linear and quadratic spatially uniform phase-shift errors for the five- and six-frame algorithms.

ϵ_1	ϵ_2	Five-Frame	Six-Frame	Six-Frame*
0.1	0.0	0.0020	0.00005	0.00005
0.0	0.2	0.0265	0.0015	0.0015
0.1	0.2	0.0260	0.0025	0.0025
0.0	0.4	0.0610	0.0060	0.0060
0.1	0.4	0.0595	0.0050	0.0050

*From Table 3 of Ref. 26.

Table 83.VI: Residual phase error (2π rad) produced by the five- and six-frame algorithms for different values of the quadratic error coefficient ϵ_2 . The error coefficients were multiplied by the spatial nonuniformity $f(x,y)$ in each case before computing residual error using the values of constants $B-M$ indicated. The descriptive terms refer to the shape of the curve produced by plotting the induced phase error given in Eq. (10) versus the phase shift α_0 .

ϵ_1	ϵ_2	Type		Five-Frame	Six-Frame
0.0833	-0.0139	Decreasing positive slope	rms	0.00490	0.00464
			p-v	0.03250	0.03010
0.0833	-0.0417	Parabola	rms	0.00236	0.00313
			p-v	0.01510	0.02030
0.0833	0.4629	Increasing exponential	rms	0.0601	0.0280
			p-v	0.2390	0.1780
0.0833	0	Linear	rms	0.00642	0.00533
			p-v	0.04100	0.03470

$B = 0.03; C = 0.008; D = E = 0.002; F = 2; G = 3; M = 0.$

observed. Thus, in the simulation, a starting phase of $\alpha_{0r} = 0$ was used. The superior performance of the five-frame algorithm by nearly the same factor in both the simulation and the experiment suggests that the form of the LCPDI phase-shift error represented empirically by Eq. (7) may be the underlying cause of the experimentally observed discrepancy.

Generally, an algorithm with more sample frames will be more effective in reducing measurement errors, depending upon the type of phase-shift error addressed by the algorithm and the type of error introduced during the measurement. Currently a period of 2 to 3 s is required between frames to ensure that the liquid crystal molecules have reached an equilibrated state, thus choosing a phase-shifting algorithm

that addresses LCPDI device-specific phase-shift errors and minimizes the number of frames required is critical. Multiple applications of the phase-offset method can also reduce higher-order phase-shift errors;¹⁵ however, this method is limited by the maximum retardance that can be obtained in an LCPDI device. This simulation and the experimental results (1) confirm the superior performance of the five-frame algorithm over the six-frame algorithm for this LCPDI, even though the six-frame algorithm was designed to address higher-order phase-shift error, and (2) emphasize the importance of understanding the underlying behavior of the phase-shift error in the LCPDI in order to choose effective phase-reduction algorithms and to optimize experimental conditions. For example, further reduction of phase errors related to the liquid crystalline host

Table 83.VII: Comparison of residual errors (2π rad) obtained using the five- and six-frame algorithms with both experimental and simulated interference images. Simulated images were obtained using the indicated values of constants A – M , corresponding to the phase perturbation shown in Fig. 83.40.

	Experiment		Simulation	
	Five-Frame	Six-Frame	Five-Frame	Six-Frame
p–v	0.1450	0.278	0.1001	0.1314
rms	0.0167	0.022	0.0164	0.0223

$H = 1.21498; A = 0.37; B = 0.06; C = 0.016; D = E = 0.002; F = G = 1; M = 0.$

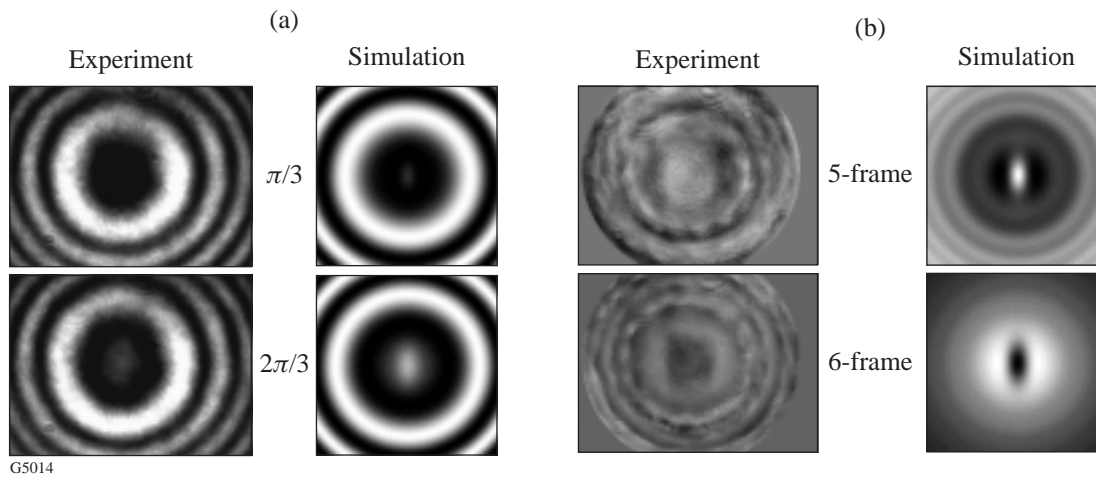


Figure 83.42

(a) Two interferograms from the six-frame series used in comparing five- and six-frame algorithms. For the images shown, the phase shift $\alpha_{0r} = \pi/3$ and $2\pi/3$, corresponding respectively to $r = 2, 3$ for the six-frame algorithm. Focusing conditions were chosen so as to introduce only a moderate amount of LC host-induced phase-shift error to avoid possible phase unwrapping errors. (b) Gray-scale images of the residual phase error $\Delta\phi = \phi_{\text{perturbed}} - \phi_{\text{ideal}}$ for the five- and six-frame algorithms. For the experimental results shown, ϕ_{ideal} was determined by a five-term Zernike fit to the phase data. Table 83.VII gives p–v and rms errors.

alignment distortions may be possible by tailoring an algorithm for the observed phase-shift error. In addition, operating the device well above the Frederiks transition threshold will reduce the alignment perturbation and thus also reduce the measurement error, once high-contrast fringes can be maintained in the higher-voltage regime through the use of a dye system without absorption dichroism. We have also begun to investigate the use of chiral-smectic-A LC's in place of nematic-phase LC's because of their faster response time, high birefringence, and gray-scale capability.^{27,28} Liquid crystal systems with a faster response time would make algorithms with a greater number of sample frames more practical.

Summary

The liquid crystal point-diffraction interferometer is attractive in that it combines the common-path design of the PDI with the high resolution that can be achieved through modern phase-shifting techniques; it is also a low-cost alternative to commercially available phase-shifting interferometers. Empty-cavity measurements using the LCPDI designed for 543 nm with a dye having large absorption dichroism produced residual p-v and rms phase errors of 19 nm (0.035λ) and 1.1 nm (0.002λ), respectively, without using a phase-offset averaging technique and with nonideal environmental conditions. This suggests that LCPDI devices to be fabricated using newly available near-IR dyes²⁰ will satisfy the desired accuracy of 105 nm at $\lambda = 1054$ nm for *in-situ* analysis of OMEGA beamlines. Using the visible-wavelength LCPDI for phase measurement of a wedged window with a polished spot yielded results that were comparable to those of the Zygo Mark IV XP, showing the current LCPDI to be a useful optical metrology tool. The LCPDI measurement matched the Mark IV measurement nearly exactly in some regions but was ≤ 50 nm discrepant in other regions. This spatially dependent error had periodicity equal to that of the interference fringes, suggesting an intensity change from frame to frame caused by the absorption dichroism of the dye as the primary cause of the discrepancy. Additional error contributors in these measurements were interference effects of multiple beams and LC molecular alignment distortions around the microsphere.

The use of a non-dichroic dye or a combination of positive and negative dichroic dyes will significantly reduce errors related to intensity changes from frame to frame. For visible-wavelength applications, the high absorbance necessary to achieve high-contrast fringes has been available from commercially available dyes, whereas for applications in the near-IR, we have synthesized several dyes showing significantly greater absorbance than can be obtained from commercial

dyes.²⁰ Two visible-wavelength dye mixtures that combine commercially available dyes having positive dichroism with Orasol dyes exhibiting negative dichroism were shown to have negligible change in absorbance over the voltage range of interest. Synthesis by-products not removed from the Orasol dyes may be the cause of the high ionic conduction measured in LCPDI cells made with these components, giving rise to a scattering texture that appeared when voltage was applied to the device. Purification of these dye components is in process, and it is expected that future LCPDI devices incorporating these purified dyes or other dye candidates will produce significantly less scatter. For wavefront analysis of OMEGA beamlines, initial tests of LCPDI devices fabricated using the newly synthesized near-IR dye mixtures show much less intensity change with voltage applied to the cell than that seen in the visible-wavelength devices, suggesting that some of these dye components may have negative dichroism.²⁰

Our investigation has also shown that director distortions in the vicinity of the microsphere can affect phase-measurement accuracy of the LCPDI and suggests that it is possible to tailor device fabrication and experimental testing parameters to reduce the effect of nematic director distortions on phase measurements. Stronger anchoring in the bulk of the fluid, achieved by using a thinner path cell, was shown to reduce the spatial extent of the alignment distortion. Obtaining weaker anchoring at the sphere surface will likely reduce phase-measurement errors by eliminating topological defects and minimizing director distortions as voltage is applied to the cell.²⁵ These director distortions were observed to perturb the interference fringes when the focus was placed very close to the microsphere, although by judicious choice of focusing regime, the contribution of alignment distortions to the phase error was significantly reduced. Our simulation using the empirically derived phase-shift error suggests that phase-measurement error due to host alignment distortions can be further reduced through the use of device-specific phase-shifting algorithms, once these distortions become the dominant contribution to the measurement error.

It is expected that (1) the use of dyes that eliminate absorbance changes during data acquisition and (2) the reduction of acoustic vibration through the use of an air-supported table and more rigid mounting of the device will greatly improve LCPDI accuracy and precision, making the LCPDI a low-cost alternative for evaluation of high-performance optical elements, such as required for OMEGA. The use of phase-shifting algorithms and averaging methods tailored for device-specific phase-shift errors can further improve LCPDI performance.

ACKNOWLEDGMENT

This work was supported by the U.S. Department of Energy Office of Inertial Confinement Fusion under Cooperative Agreement No. DE-FC03-92SF19460, the University of Rochester, and the New York State Energy Research and Development Authority. The support of DOE does not constitute an endorsement by DOE of the views expressed in this article.

REFERENCES

1. K. Creath, in *Progress in Optics XXVI*, edited by E. Wolf (North-Holland, Amsterdam, 1988), Chap. V.
2. M. V. R. K. Murty, in *Optical Shop Testing*, edited by D. Malacara, Wiley Series in Pure and Applied Optics (Wiley, New York, 1978), Chap. 4, pp. 105–148.
3. V. P. Linnik, C.R. Acad. Sci. (USSR) **1**, 208 (1933).
4. R. N. Smartt and W. H. Steel, Jpn. J. Appl. Phys. **14**, 351 (1975).
5. D. Malacara, ed. *Optical Shop Testing*, Wiley Series in Pure and Applied Optics (Wiley, New York, 1978).
6. See, for example, several references in Ref. 8.
7. C. R. Mercer and K. Creath, Opt. Lett. **19**, 916 (1994).
8. C. R. Mercer and K. Creath, Appl. Opt. **35**, 1633 (1996).
9. C. R. Mercer and N. Rashidnia, in *8th International Symposium on Flow Visualization 1998*, edited by G. M. Carlomagno and I. Grant (Edinburgh, Scotland, 1998), CD-ROM, pp. 256.1–256.9.
10. Zygo Mark IVxp™, Zygo Corporation, Middlefield, CT 06455.
11. M. J. Guardalben and N. Jain, Opt. Lett. **25**, 1171 (2000).
12. J. Schwider *et al.*, Appl. Opt. **22**, 3421 (1983).
13. P. Hariharan, B. F. Oreb, and T. Eiju, Appl. Opt. **26**, 2504 (1987).
14. S. D. Jacobs, S. R. Arrasmith, I. A. Kozhinova, L. L. Gregg, A. B. Shorey, H. J. Romanofsky, D. Golini, W. I. Kordonski, P. Dumas, and S. Hogan, Am. Ceram. Soc. Bull. **78**, 42 (1999).
15. J. Schwider, T. Dresel, and B. Manzke, Appl. Opt. **38**, 655 (1999).
16. A. C. Turner, 1998 Summer Research Program for High School Juniors at the University of Rochester's Laboratory for Laser Energetics, Laboratory for Laser Energetics Report No. 300, NTIS document No. DOE/SF/19460-299 (1998). Copies may be obtained from the National Technical Information Service, Springfield, VA 22161.
17. R. Rao, 1999 Summer Research Program for High School Juniors at the University of Rochester's Laboratory for Laser Energetics, Laboratory for Laser Energetics Report No. 311, NTIS document No. DOE/SF/19460-338 (1999). Copies may be obtained from the National Technical Information Service, Springfield, VA 22161.
18. The Orasol dyes were recommended by C. Mercer, private communication.
19. E. Prudnikova, B. Umanskii, and T. Plyusnina, Mol. Cryst. Liq. Cryst. **332**, 37 (1999).
20. Laboratory for Laser Energetics LLE Review **81**, 37, NTIS document No. DOE/SF/19460-335 (1999). Copies may be obtained from the National Technical Information Service, Springfield, VA 22161.
21. P. Poulin and D. A. Weitz, Phys. Rev. E **57**, 626 (1998).
22. P. Poulin, N. Frances, and O. Mondain-Monval, Phys. Rev. E **59**, 4384 (1999).
23. A. Glushchenko *et al.*, Liq. Cryst. **23**, 241 (1997).
24. H. Stark, J. Stelzer, and R. Bernhard, Eur. Phys. J. B **10**, 515 (1999).
25. O. Mondain-Monval *et al.*, Eur. Phys. J. B **12**, 167 (1999).
26. K. Hibino *et al.*, J. Opt. Soc. Am. A **14**, 918 (1997).
27. S. Garoff and R. B. Meyer, Phys. Rev. A **19**, 338 (1979).
28. A. Sneh, J. Y. Liu, and K. M. Johnson, Opt. Lett. **19**, 305 (1994).

Understanding the Mechanism of Glass Removal in Magnetorheological Finishing (MRF)

Introduction

Two magnetorheological (MR) fluids are currently in widespread industrial use for the commercial manufacture of high-precision optics using magnetorheological finishing (MRF). One composition, which consists of cerium oxide in an aqueous suspension of magnetic carbonyl iron (CI) powder, has been found appropriate for almost all soft and hard optical glasses and low-expansion glass-ceramics. The second composition, which uses nanodiamond powder as the polishing abrasive, is better suited to calcium fluoride, IR glasses, hard single crystals (i.e., silicon and sapphire), and very hard polycrystalline ceramics (i.e., silicon carbide).

The extension of MRF to a vast array of materials is possible because of the unique nature of this finishing process. The magnetic carbonyl iron particles may be thought of as a form of variable compliance lap that supports the nonmagnetic polishing abrasives. Lap stiffness may be increased or decreased by adjusting the CI concentration and/or the magnetic field strength.

Considerations leading to a choice of nonmagnetic polishing abrasive are more complex than those encountered in conventional pitch or pad polishing. Not only do the hardness and chemistry of the abrasive grains need to be appropriate to the workpiece, but the type of abrasive (median size, surface chemistry) can have a large or small effect on the out-of-field MR fluid rheology. Fluid properties in an MRF machine circulation system must be held constant to realize constant rates of material removal during polishing.

Advances have been made in understanding the mechanism of removal with MRF, based in part on the hardness of the CI powder, the magnetorheological properties of the MR fluid, and the interaction of cerium oxide or other abrasives with the workpiece surface. This article presents the results of recent studies, within the context of classical optical polishing operations.

The mechanisms of material removal important to glass polishing have been an area of study for years. Cumbo¹ describes the goals of precision polishing to be to shape the glass to within $0.1 \mu\text{m}$ of the desired form, to remove subsurface damage created by grinding operations, and to reduce the peak-to-valley (p-v) roughness to less than 5 nm. While there are several proposed mechanisms of material removal in polishing, none are widely accepted. Some authors describe polishing in terms of small-scale fracture,^{2,3} while others describe it as “plastic scratching” of a hydrated layer⁴ or a tribo-chemical wear process.⁵ The goal of this work is to try to use some of these existing theories to understand the mechanisms of material removal in the MRF of glass.

Preston⁶ gave a classic theory of removal in glass polishing that is still being studied today. He states, “(…the rate at which material is removed) is proportional to the rate at which work is done on each unit area of the glass.” Furthermore, he defines the work done in time t as

$$w = \mu A p v t, \quad (1)$$

where w = work ($\text{N} \cdot \text{m}$), μ = coefficient of friction, A = area of contact between the glass and polishing lap (m^2), p = pressure applied to the glass part (N/m^2), v = relative velocity between the lap and the part (m/s), and t = time in which work is done (s).

The term μp is the specific traction, or drag divided by the contact area, of the polishing lap (felt in this case) on the glass. The expression in Eq. (1) states that the work done on the material is proportional to the specific drag force multiplied by the area of contact and the velocity. He continues to say that if the specific drag force remains constant, then the removal rate is proportional to “…the amount of felt that passes over it…this is independent of velocity, except in so far as velocity may affect the amount of felt passing over.”⁶ In general, these statements are true in MRF as well: namely, that the

material removal scales with the drag force and is primarily controlled by the time of contact between the abrasive and the glass surface.

Preston's equation is commonly written in a slightly different form,

$$\frac{dz}{dt} = C_P \frac{L}{A} \frac{ds}{dt}, \quad (2)$$

where dz/dt = the change in height in time, or removal rate (m/s), C_P = Preston's coefficient (m^2/N), L = total normal load applied (N), A = area over which wear occurs (m^2), and ds/dt = velocity of the work piece relative to the tool (m/s).

The difficulty comes in defining Preston's coefficient in Eq. (2). The discussion above shows that a friction coefficient makes up part of it, but several other things are accounted for in this coefficient. The importance of various effects that make up Preston's coefficient in MRF will be demonstrated here. One of these is the chemical effects associated with the presence of water in the MR fluid. The mechanics associated with how different abrasive types affect the removal of material in MRF are also given. Before describing the mechanisms of material removal in MRF, it is instructive to discuss proposed mechanisms in other polishing processes.

Review of Mechanisms of Material Removal

Silvernail and Goetzinger^{7,8} summarize various factors that are important to glass polishing. Aside from pressure and velocity, they note that the polishing agent, liquid carrier fluid, and polishing lap are all important. Their results show that adding water to the slurry dramatically increases the removal rate of a crown glass. They conclude that the improved removal rate due to the addition of water is independent of the other parameters in the system (e.g., abrasive concentration, pressure, etc.) and that the interaction is primarily with the glass. The results that show changes in the polishing due to lap type are inconclusive. An increase in removal rate is seen with an increase in cerium oxide content, showing that the concentration of the slurry is important to material removal. This effect generally levels off at a concentration between 10 wt% and 20 wt% (approximately 1 vol% to 3 vol%). Furthermore, they discuss how cerium oxide behaves as an excellent abrasive while other rare earth oxides that are similar in structure are not good abrasives. They cannot explain the increased polishing effect of cerium oxide.

Other authors describe glass material removal in terms of small fracture events caused by the abrasive interacting with the glass surface. Buijs and Korpel-Van Houten² describe material removal of glass surfaces by abrasive particles through an indentation fracture theory. This process is intended to explain lapping, but a polishing process based on a similar theory could be envisioned. Essentially they describe how the abrasive particle acts like a Vickers indenter under a normal load. Material removal occurs through lateral cracking of the glass under the indenter-like abrasive. Removal rates in this model depend on the shape of the particle and material properties of the glass (namely, elastic modulus, hardness, and fracture toughness). While this explanation is typically used to explain grinding and microgrinding, Lambropoulos *et al.*³ show that removal rates obtained with MRF correlate with the same material properties described by Buijs and Korpel-Van Houten. They explain the fracture occurring through mechanisms other than indentation, however. Asperities on the surface can be modeled as nanometer-sized cracks. The abrasive contacts the asperity through shear and normal loads. In this geometry, the shear load works to drive the crack, while the normal load tends to close the crack. If the shear force is large enough relative to the normal load, fracture of the asperity will occur. This is different from Buijs *et al.* in that this mechanism is shear driven, while their work is controlled by lateral cracking from normal loads indenting the particle. The work of Lambropoulos *et al.* is in its early stages, but it gives a plausible explanation of how removal rates in polishing correlate with parameters used to describe fracture.

Water's positive impact on polishing is discussed in several other references. If polishing is thought to consist of small fracture events, then the effect of water can be explained by Michalske and Bunker.⁹ The authors (and references) describe how water can attack the Si-O-Si bonds at the crack tip, which results in a reduced fracture toughness of the glass. Furthermore, the hydrolysis rate increases as the stress of the bond increases. Consider the model proposed by Lambropoulos *et al.*³ and/or Buijs *et al.*² According to Michalske and Bunker's theory, the presence of the water as well as the stresses applied by the abrasive to the glass surface would dramatically reduce the fracture toughness of the material as well as speed up the kinetics of the process.⁹ This possibly explains why water enhances the removal of glass in polishing.

A second, possibly related, mechanism of material removal also involves hydration of the glass surface due to chemical interaction between the carrier fluid (water) and the glass surface. Cook¹⁰ describes how the water molecule breaks Si-

O-Si bonds and how this helps to create a hydrated layer in the glass surface. Cumbo^{1,11} gives a summary of Cook's work and extends it with a study of the chemical effects in polishing experiments. Cook's¹⁰ process basically describes how the loads applied to the surface by the abrasive promote diffusion of water into the silica network. As the water dissociates, it attacks the bonds within the network, weakening the structure. This promotes bond breakage and material removal. Cerium oxide and zirconia particles are described as having "chemical tooth," which promotes bonding of the abrasive to the silica. This promotes material removal from the silica network as well as inhibits redeposition of material back onto the surface. For chemically inactive materials, such as diamond, removal is said to depend on the carrier fluid's ability to carry the removed material away since the silica does not bond with the abrasive.

Izumitani's theory of the mechanism of material removal is also based on the idea of the hydrated layer.⁴ This hydrated layer is caused by a chemical reaction between modifier ions in the glass and the hydrogen ions in the water. Material removal occurs by abrasive particles scratching away this layer. The speed at which material is removed depends on how quickly the hydrated layer is formed (chemical durability of the glass) and the hardness of the hydrated layer as well as the hardness and/or friability of the abrasive. He showed that a softer abrasive that is more easily crushed but still harder than the hydrated layer is most effective. His explanation is that the crushing provides more particles and therefore a higher frequency of scratching events. He also describes the necessary properties of the lap used in polishing. The lap must be hard enough to support the abrasive and transmit pressure, but soft enough to allow the particle to embed into the polishing lap.

Evidence in the literature supports the existence of a surface layer that is created by hydration of the surface during polishing. Izumitani⁴ creates a hydrated layer by immersing the glass surfaces in 0.1 N solution of HCl. Subsequent Vickers microhardness tests show a reduction in microhardness of this layer with increased immersion time. Furthermore, he shows that the polishing rate increases as the microhardness of the hydrated layer decreases. Yokota *et al.*¹² use ellipsometry to show the existence of the hydrated layer after polishing. They demonstrate a reduction in refractive index in a small surface layer in glasses that are susceptible to chemical attack. The size of these layers is of the order of tens of nanometers deep. Glasses of interest to this work, borosilicate crown and silica, each reportedly have hydrated layers of approximately 40 nm with the polishing conditions studied. Maaza *et al.*¹³ use grazing-angle neutron reflectometry (GANR) to study the hydrated layer.

They also show evidence of a hydrated layer from the polishing process. The hydrated layer of their Borkron surfaces was approximately 5 nm (Borkron is a special borosilicate glass used for neutron optics applications¹³). It is 15 nm for the floated face of float glass and 40 nm for the nonfloated face. They also report on the existence of 2-nm cracks in the float glass from the polishing process. Yokota *et al.*¹² describe how some chemically resistant glasses like fused silica (FS), Vycor, and Pyrex actually show densification of the material in these layers. They explain this densification to be caused by high local pressures on the glass surface due to polishing. Shorey *et al.*¹⁴ provide more evidence of densification in fused silica by comparing numerical simulations with nanoindentation experiments. Densification apparently depends on the state of stress from both normal and shear loading.

Kaller^{5,15} describes a process he refers to as a tribo-chemical friction wear process. According to Kaller, the abrasive should be softer than the surface being polished, and the most important property of a polishing agent is its ability to "grip" the surface. He states that the most effective polishing abrasives (mostly cerium oxide and iron oxide) have a large number of lattice defects produced during manufacture, and it is the presence of these defects that promotes the gripping of the abrasive to the surface. He describes three steps: The first is intimate contact between polishing grains and the glass surface. This coupled with friction or shear forces promotes lattice deformation and partial removal of surface layers of the abrasive grain. Second, removal of these surface layers exposes ionic vacancies in the lattice, which bond with the glass. Finally, the continued motion of the polishing wheel produces continuous removal of glass. He continues his discussion to address how manufacturing methods can produce more, or fewer, lattice defects, as well as determine the primary crystallite size. Important additional lattice defects are created through (1) valance change of the oxide, (2) incorporation of metal ions or molecules into the lattice, and (3) quenching. Finally, he discusses how careful control of processing allows control of crystallite size, number of defects, and rubbing resistance. For a given process a particle could be manufactured with the appropriate number of lattice defects so that the abrasion resistance matches the process for which it is intended. In other words, a cerium oxide particle can be produced that will provide a low rubbing resistance (soft particle), which means low removal, but a high precision surface. A (hard) cerium oxide particle could also be produced to provide a high rubbing stress, which would give higher removal, but less precise (rougher) surfaces. He states that the first abrasive would be used in low shear to be most effective, but that the second one

would increase its effectiveness at very high shear, presumably due to the exposure of new lattice defects. His only discussion of a hydrated layer is to say that experiments that were supposed to prove the existence of the hydrated layer did not. To explain other observations of a densified surface layer resulting from the pressure of polishing, Kaller claims evidence for nanometer-scale abrasive particles left on or in the surface after polishing. He refutes the idea of a smallest-size limit in milling of abrasives.

Kaller's ideas are at least partially supported by Kirk and Wood.¹⁶ In their paper, they describe the calcination of cerium oxide sol-gels and show evidence of significant changes in the crystallography due to calcination temperature. Before calcination, the particles are loosely bonded and of the order of 5 to 10 nm in size. After calcination at 850°C for 1800 s, the crystallite size increases to about 60 to 80 nm, and they become strongly bonded together. Furthermore, they show that the {111}-type planes grow faster than {200} planes at elevated temperatures. The {111} planes have a higher atom density than the {200} planes, which means that more cerium atoms are exposed. The hypothesis is that this explains the increased polishing efficiency of properly calcined cerium oxide.

Several views on the roles of the various constituents in the polishing process clearly exist. Water plays a major role in glass polishing. It is not clear whether this is due to the reduced fracture toughness at the glass surface or a softening due to chemical attack of the silica network. Actually, each process description is similar, and there may be two ways of saying the same thing. The type of abrasive is also important. The wide acceptance of cerium oxide in glass polishing is explained to be due to its chemical tooth, which could be explained by Kaller's lattice defect theory. Also, both Izumitani⁴ and Kaller⁵ show that it is possible to polish hard materials with relatively soft abrasives; however, hard materials such as diamond can also be used. The relative effectiveness of an abrasive is not solely due to its hardness.

Much of this discussion is as appropriate for MRF as it is for the more common pitch or pad polishing. The ability of abrasives softer than the glass to polish, even in the absence of water, will be shown. Furthermore, without water, abrasives harder than the glass surface have difficulty maintaining contact with the surface and actually have a lower material removal rate than the softer abrasive. This will be explained the same way Preston did for Eq. (1); namely, removal rate is proportional to how long the abrasive is in contact with the glass surface. The importance of water in MRF and how it

allows abrasives to more easily abrade material away from the surface will be shown. Finally, the interactions of different abrasives with the glass surface are demonstrated. An increase in abrasive concentration increases the time the abrasives are in contact with the glass surface. This results in increased removal. The hypothesis that cerium oxide grips the glass better and that this leads to an increase in measured drag force under identical experimental conditions as aluminum oxide and diamond is experimentally substantiated. Diamond drastically reduces drag but gives an increased removal rate.

Overview of MRF

Several references describe the evolution of MRF in recent years.^{17–19} This process utilizes magnetic particles, nonmagnetic polishing abrasives in either an aqueous or nonaqueous carrier fluid, and a magnetic field to polish materials. The “standard” MR fluid consists of 36 vol% of carbonyl iron (CI) as the magnetic component and 6 vol% of cerium oxide as the abrasive with the balance made up of de-ionized (DI) water and fluid stabilizers.^{19,20} Figure 83.43 shows an SEM and size distributions of particles after being used in MRF for one week. The dark spherical particles are the magnetic CI and have a median particle size of 4.5 μm . The lighter, small particles are the nonmagnetic abrasive, which in this case is cerium oxide. The cerium oxide starts with a median size of 3.5 μm with a fairly broad distribution. The SEM shows several significantly smaller particles that are likely due to milling of the abrasives during use. Proper manipulation and control of the MR fluid allows MRF to successfully polish a wide variety of materials with commercially viable removal rates.^{18,19} Removal rates obtained with the standard MR fluid vary from about 2 $\mu\text{m}/\text{min}$ for a hard silica glass like fused silica to more than 9 $\mu\text{m}/\text{min}$ for a soft laser glass like LHG8.¹⁷

The primary concern of this work is to study how MRF polishes glass. Figure 83.44(a) shows a photo of an MRF machine with a vertical wheel [schematic of this machine shown in Fig. 83.44(b)]. MR fluid is pumped from the fluid conditioner (1) up to the nozzle (2), where it is ejected onto the rotating vertical wheel as a ribbon. The wheel shape is that of a portion of a 150-mm-diam sphere. At the initial point of contact, the MR fluid is a viscous fluid with the approximate consistency of honey (viscosity $\approx 0.5 \text{ Pa}\cdot\text{s}$, yield stress $\approx 0 \text{ kPa}$). The rotation of the wheel drags the fluid under the part in region (3), where it is acted upon by the magnetic field. The MR fluid ribbon flows through the converging gap between the lens and the wheel. The magnetic field stiffens the ribbon in this region, giving it the approximate consistency of clay (yield stress $\approx 10 \text{ kPa}$). Significant forces are created by the interac-

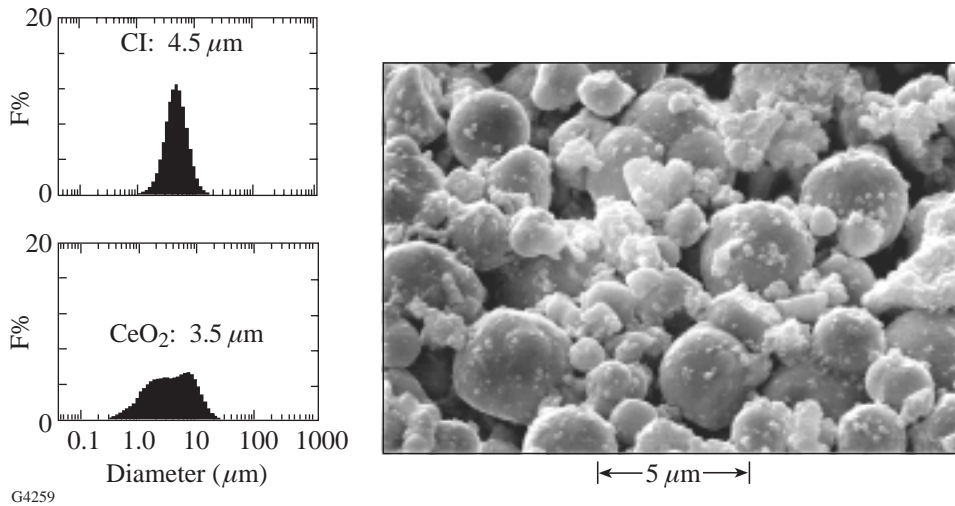
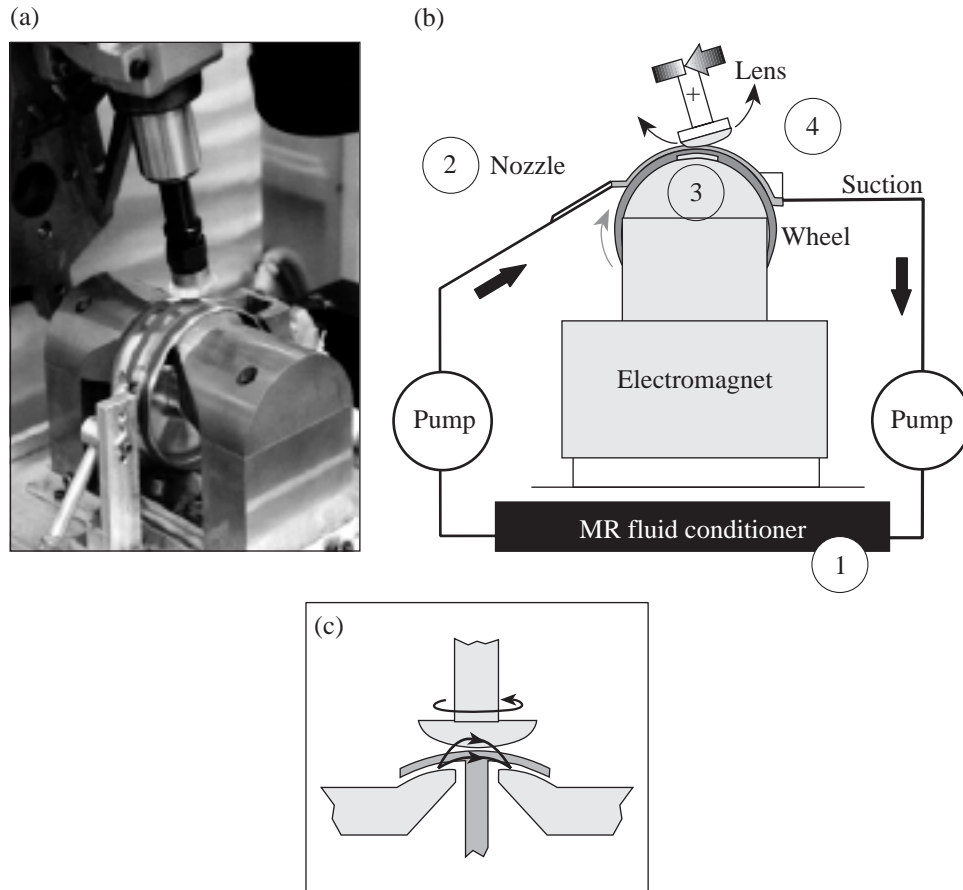


Figure 83.43
SEM of particles and their initial size distributions after one week of use in MRF. The dark spherical particles are the hard magnetic carbonyl iron particles. They have a median size of 4.5 μm. The smaller, light particles are the cerium oxide abrasives. They initially have a broad size distribution with a median particle size of 3.5 μm. The large amount of small particles in the SEM suggests that milling of the cerium oxide occurs during use.



G4995

Figure 83.44
The setup used in MRF with a vertical wheel. (a) A photo of an actual MRF machine. (b) A schematic of the MRF machine. Fluid is pumped from the conditioner at (1) to the nozzle at (2) onto the rotating wheel. The wheel carries the fluid between the part and wheel into the magnetic field at (3), where the field causes it to stiffen. Hydrodynamic flow in this region causes stresses sufficient to cause removal to occur. The wheel continues to carry the fluid outside of the field region, where it is removed from the wheel at (4). This fluid is again pumped to the conditioner to complete the circuit. (c) Cross-sectional view showing the relative orientation of the 150-mm-diam spherical MRF wheel, pole pieces, and part. Field lines in the polishing zone are schematically shown.

tion between the wheel, MR fluid, and glass surface since the MR fluid ribbon flows through a converging gap, deforming from a thickness of 2 mm to one of 1.5 mm. Rotation of the wheel continues to drag the MR fluid from region (3) over to region (4), where it is removed from the wheel through suction. Here, the magnetic field does not act on the MR fluid, so it again has the consistency of honey. The MR fluid is pumped back to the fluid conditioner, where it is cooled to a setpoint temperature and any evaporative losses are replaced. Our primary area of concern is region (3) inside the magnetic field where polishing occurs. Figure 83.44(c) shows a cross-sectional view of this region. The pole pieces provide the magnetic field to stiffen the MR fluid. This fringing field between the gap of the pole pieces has a strong vertical gradient. The field is higher at the wheel surface than it is at the part surface, which causes the CI to be pressed against the wheel surface and the nonmagnetic abrasive to move to the glass surface.

Figure 83.45(a) shows a photo of the MR fluid contacting a meniscus lens surface (flow direction is left to right for all of Fig. 83.45). The fluid contacts the surface in the shape of a backward D. This is the shape of the removal under the action of the rotating wheel if the part is held stationary in the fluid. This D-shaped region is referred to as the “spot” from this point on. The white regions surrounding the spot and extending downstream (to the right) from the spot are abrasive particles. This is evidence of the fact that abrasives move to the part surface under the action of the magnetic field. Figure 83.45(b) shows an interferogram of a removal spot; its oblique view is shown in Fig. 83.45(c) (adapted from Ref. 18). The surface before and after a removal experiment is evaluated using a phase-shifting interferometer.²¹ The instrument software is used to subtract the initial surface from the final surface containing the spot. Height variations on the resulting image

are due to material removed from the initial surface. The peak removal rate is found by dividing the depth of deepest penetration by the contact time between the part and MR fluid ribbon.

The proximity of the part and wheel surface changes due to the curvature of the wheel (and part, if polishing a lens). The location of the deepest and widest part of the spot shown in this figure is approximately the position of closest approach between the part and the wheel surface. During polishing, the part is rotated and swept through the polishing zone, allowing material to be removed in annular regions over the entire part surface. Computer-controlled dwell times allow control of the surface figure of the polished surface to a precision of $\lambda/20$.¹⁸

Removal mechanisms on a macroscopic scale have been previously considered.^{22,23} Since the normal force on an abrasive particle is low compared with conventional polishing,²⁴ a shear-controlled mechanism has been described.^{22,23} MR fluids are modeled as Bingham fluids with a yield stress (~10 kPa) and small plastic viscosity (~0.5 Pa•s).^{17,22,23,25} The flow of a fluid with a yield stress through a converging gap, like the one between the rotating wheel and part surface in MRF, allows the possible formation of unsheared regions called “cores” (see Fig. 83.46). These cores effectively reduce the gap between the wheel and part surface and cause increased shear stresses on the downstream end of flow. While the opacity of the MR fluid prevents visual confirmation of the presence of these cores, material removal has been shown to increase in the region where these cores are expected to be located.²³ In general, the low normal loading in MRF keeps an abrasive particle in contact with the glass surface, but material removal is primarily controlled by the shear stresses applied to the abrasive through the bulk flow of the MR fluid.

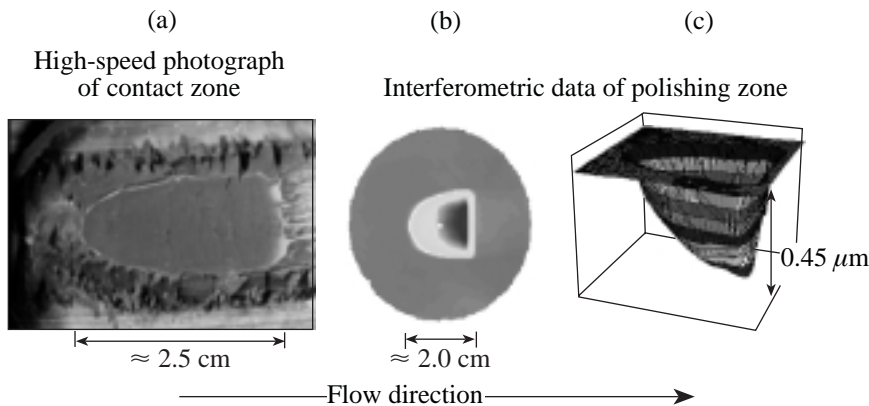


Figure 83.45

The spot in MRF. Flow is from left to right in all parts of this figure. (a) An actual photo of the contact region, or “spot,” on a stationary meniscus lens. (b) Interferogram of the material removed from the spot. Interferometric characterization of the spot gives a removal function that a computer program can use to vary dwell time of this spot over the surface. This allows precise control of the figure during polishing. (c) An oblique view of the figure during polishing. The deepest region is at the trailing edge of the flow and is approximately the position of closest approach between the part and wheel.

G4996

Experimental Considerations and Earlier Screening Studies

The spot-taking machine (STM)—a machine similar to the commercial MRF polishing machine²⁶—is used to perform these material removal experiments [see Fig. 83.44(a)].¹⁹ The only automated degree of freedom in the part motion on the STM is the height of the part above the rotating wheel. There is no rotation or swing of the part, so a removal experiment consists simply of making a spot on a flat part. Important machine parameters are held constant for all removal experiments. The vertical wheel rotates at 150 rpm, the MR fluid ribbon height is 2.0 mm, and the part surface is placed 0.5 mm into the MR fluid. The current to the electromagnet is kept at 15 A. This results in the magnetic flux density having a horizontal component of about 260 kA/m, 1 mm above the wheel surface.²⁷

Water loss due to evaporation from aqueous MR fluids is a concern during removal experiments. If this evaporation is left unchecked, the actual CI concentration of the MR fluids, and therefore the viscosity and yield stress, will increase. The STM monitors the viscosity in real time and maintains the appropriate CI concentration. An off-line moisture analyzer is used at the beginning of each experiment to measure moisture content in the MR fluid.²⁸ It is therefore possible to calculate the actual CI concentration for data analysis.

The viscosity outside of the magnetic field is measured off-line before each set of experiments using a cone and plate viscometer²⁹ whose shear rate may be varied from 0 to 960 1/s. These MR fluids are shear thinning, which means that the apparent viscosity decreases as the shear rate increases. Because of this, the viscosity is monitored at only the maximum shear rate since this is the approximate shear rate both in the fluid delivery system and underneath the part during polishing.

For all the experiments performed, the viscosity at 960 1/s is 60 ± 20 cps. As expected, the viscosity tends to increase with the amount of solids in an MR fluid. This viscosity is kept low so that it is easily pumped by the fluid delivery system.

Roughness measurements are made with two instruments. One is a white-light interferometer, which measures the roughness over a $0.25\text{-mm} \times 0.35\text{-mm}$ area and has a lateral resolution of $1.1 \mu\text{m}$.³⁰ This interferometer is a valuable tool in measuring the microroughness of a part. The second instrument is an atomic force microscope (AFM), which measures the roughness over a smaller region.³¹ Scans are performed in contact mode over a $5\text{-}\mu\text{m} \times 5\text{-}\mu\text{m}$ -square region using 256 samples, at a rate of 1 Hz. This allows us to investigate submicron features from polishing with a lateral resolution approaching 20 nm. The vertical scale is 15 nm for all AFM scans presented here.

Each fluid is characterized on the magnetorheometer described in previous work^{23,25} to determine the dynamic yield stress of the fluid. The MR fluids are tested at magnetic fields with flux densities of 200 kA/m and 250 kA/m only, since this is the nominal flux density at 15 A on the STM in the region of fluid/part interaction. Fixed conditions for other experimental parameters on the magnetorheometer are polishing configuration, 0.5-mm gap, and 3.33-rpm cup speed. The results of our work on the magnetorheometer are shown in Fig. 83.47. The data from this experiment were taken in the range of 40 vol% to 45 vol% CI. The dynamic yield stress does not change for CI compositions greater than about 35 vol% CI but asymptotically approach values of about 15 kPa at 200 kA/m and 20 kPa at 250 kA/m for a variety of commercial CI powders. The yield stress of the MR fluid is also unaffected by the incorporation of nonmagnetic abrasives at the low loading used for these experiments.

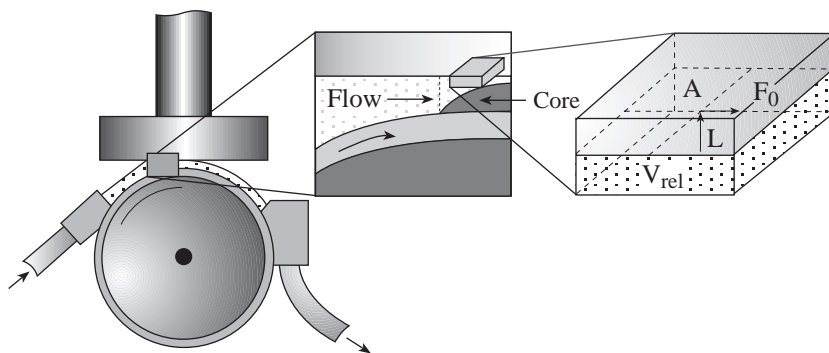


Figure 83.46
Schematic showing the contact between the MR fluid and the glass. The first callout shows the internal structure of the flow. The removal rate increases in the region of the core due to the increased shear stresses that result from the throttling action of the core. If material removal is considered over a small material volume, a Preston-type equation based on the shear stress at the part surface can be used to describe the removal process.

G4997

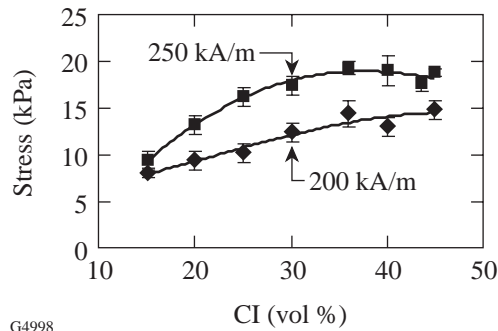


Figure 83.47

Dynamic yield stress measured on the magnetorheometer for the MR fluids used in removal experiments. Measurements were taken in the polishing configuration, 0.5-mm gap and 3.33-rpm cup speed at fields with a flux density of 200 kA/m and 250 kA/m. The yield stress is approximately 15 kPa at 200 kA/m and 20 kPa at 250 kA/m for the fluids between 40% and 45% CI concentration—the region of interest for these experiments. This data is for a variety of CI types, both with and without abrasives. The type of CI and presence of abrasives in this low loading have no effect on the dynamic yield stress of the MR fluid. Solid lines have been added only to aid the eye.

The flow of an MR fluid between the part surface and wheel is complicated. The yield stress does not give a full representation of the forces applied to the part by the fluid during removal.^{22,23} Because of this, the pressure and the total drag force applied to the part by the fluid are measured as well. A pressure-sensing pad³² is used to measure the pressure distribution applied to the part by the MR fluid. Measurements are taken by adhering the sensor to the part surface and lowering it into the MR fluid ribbon.

The drag force is measured using a linear translation stage,³³ a sapphire flat, and a 5-lb (≈ 22.2 N) load cell.³⁴ The interaction between the sapphire flat and the MR fluid forces the linear stage in the direction of flow. The linear stage, free to move horizontally, is driven into the load cell with a force equal to the drag force applied by the MR fluid. Drag force measurements are taken with the part at a depth of 0.5 mm into the MR fluid for experiments with nonaqueous MR fluids and a 1.0-mm depth with aqueous MR fluids (drag force measurements reported later for aqueous MR fluids without abrasives were done at both 0.5-mm and 1.0-mm depths). While this does not allow a direct comparison between pressure and drag measurements, it is sufficient for an evaluation of the relative performance of each fluid where the pressure and drag force are considered separately.

To fully understand mechanisms of material removal in MRF, the roles of the various constituents of the MR fluid need

to be separated and evaluated. In previous work, we described how the nanohardness (H_{nano}) of the magnetic carbonyl iron (CI) and nonmagnetic polishing abrasives could be determined through novel nanoindentation techniques.^{35,36} These results were used to conduct initial screening experiments on the importance of (1) the nanohardness of the CI in nonaqueous MR fluids without abrasives and (2) the effect of gradually adding DI water to the MR fluid and how the DI water changed abrasive interactions with the glass surface.³⁶ It was found that in nonaqueous MR fluids, CI that was softer than the glass surface slowly abraded material but did not penetrate the glass surface. Harder CI penetrated the glass surface. Adding DI water turned on chemistry and changed the way hard particles were seen to interact with the glass surface, due to the evolution of a hydrated or underdense (corroded) layer that enhanced rates of material removal. Removal rates were related to the mechanical properties of the CI and the glass. Surface morphologies resulting from abrasive/part interaction were consistent for three different glass types: BK7, LHG8, and FS.

Mechanisms of Removal in MRF

The work described in this section is based upon our previous screening studies. Aqueous MR fluids are used to remove material from a fused-silica (FS)³⁷ surface. These MR fluids are made up separately of hard CI ($H_{\text{nano}} = 11.7 \pm 0.8$ GPa), soft CI ($H_{\text{nano}} = 2.2 \pm 1.0$ GPa), and varying amounts of nonmagnetic polishing nano-abrasives (cerium oxide, aluminum oxide, and diamond). Variations in the material removal of FS ($H_{\text{nano}} = 9.9 \pm 0.1$ GPa) are monitored as a function of abrasive type and amount.

To study the effects of DI water in polishing requires a carrier fluid that suppresses the chemical effects. A dicarboxylic acid ester (DAE) has a density of 1.189 g/ml at 20°C³⁸ and a viscosity of 2.85 cps at 23°C,³⁹ which is similar to the density and viscosity of water, 0.982 g/ml and 1.0 cps, respectively.³⁸ This allows the nonaqueous DAE-based MR fluid to have a solids loading and rheology similar to the aqueous MR fluid. Another advantage of the DAE is that water is soluble up to 8.3 wt% (≈ 7 vol%), which makes it possible to study the chemical effects of water incrementally. Removal rates of BK7 glass were shown to increase exponentially with water concentration in this range (see Ref. 40).

The nine MR fluids studied here are summarized in Table 83.VIII. MR fluids 1 through 5 are made up with a carrier fluid and CI only. MR fluid 1 has 40 vol% soft CI and 60 vol% DAE; MR fluid 2 contains 40 vol% of the hard CI and 60 vol% DAE. MR fluid 3 is the same as MR fluid 2, except

that 1 vol% DI water is added to the composition. MR fluids 4 and 5 are the same as MR fluids 1 and 2 except that MR fluids 4 (soft CI) and 5 (hard CI) utilize an aqueous carrier fluid (made up of DI water and <1 vol% of stabilizing agents).

1. Removal Experiments Without Polishing Abrasives

Each MR fluid was used on the STM to put a removal spot on a 50-mm-diam FS surface initially polished flat to within $\lambda/4^{21}$ and 0.9 ± 0.1 -nm rms roughness.³⁰ Normal stresses were measured as previously described. The peak pressure was found to be 129 ± 4 kPa for all tests. The drag force was measured at a 0.5-mm gap and found to be 0.6 ± 0.2 N. This 0.2-N variation is measured within three repetitions of a single experiment and is due to the resolution of the cell. Removal rates were determined interferometrically as described on p. 162. Stated removal rates are the peak removal rate for a single spot. Removal rates under identical conditions in MRF have been found to be repeatable to within 2.5% error.²³

The results of this study are shown in Fig. 83.48. The areal rms roughness is plotted against the peak removal rate with the profilometer maps³⁰ given. The number on each profilometer map corresponds with the MR fluid number of the experiment, and the arrow gives the flow direction of the MR fluid. MR fluid 1, with soft CI, gives a low removal rate of $0.003 \mu\text{m}/\text{min}$

and a relatively low roughness (2.3 ± 0.1 nm) and leaves faint grooves in the direction of flow. No sleeks are apparent (sleeks are defined as the pit-like features with comet tails). The removal rate is still low for MR fluid 2 ($0.004 \mu\text{m}/\text{min}$) but the areal rms roughness increases to 22.6 ± 1.7 nm. Large numbers of pits and sleeks are seen as a result of the hard CI. The effect of adding a small amount of water to MR fluid 2 is shown with the result for MR fluid 3. The removal rate increases $2.5\times$ to $0.010 \mu\text{m}/\text{min}$, and the areal roughness drops to 7.0 ± 1.0 nm rms. Also, the numbers of sleeks is reduced, and they tend to become longer scratches. Using MR fluids 4 and 5 for removal experiments further emphasizes the effect of the DI water. The removal rate increases from $0.01 \mu\text{m}/\text{min}$ (MR fluid 3) to $0.23 \mu\text{m}/\text{min}$ for MR fluid 4 and $0.14 \mu\text{m}/\text{min}$ for MR fluid 5. The $0.25\text{-mm} \times 0.35\text{-mm}$ areal rms roughness values for these two aqueous MR fluids are greatly reduced (0.8 ± 0.2 nm for MR fluid 4, and 1.3 ± 0.3 for MR fluid 5). Also, the profilometer scans clearly indicate many fewer sleeks than for the nonaqueous MR fluids. It is interesting to note that the soft CI-based MR fluid 4 actually has a higher removal rate than the hard CI-based MR fluid 5. Otherwise, the presence of the DI water significantly diminishes the effect of the CI particle hardness in these experiments. Atomic force microscope images over $5\text{-}\mu\text{m} \times 5\text{-}\mu\text{m}$ areas show no significant differences in the FS surface for removal experiments with MR fluids 4 or 5.

Table 83.VIII: Summary of the MR fluids used for material removal experiments.

MR Fluid Number	Vol% CI	†CI Nanohardness (Gpa)	DAE (Vol%)	*Water (Vol%)	Abrasive Type (Amount, Vol%)
1	40	2.2 ± 1.0	60	0	None
2	40	11.7 ± 0.8	60	0	None
3	40	11.7 ± 0.8	59	1	None
4	40	2.2 ± 1.0	0	60	None
5	40	11.7 ± 0.8	0	60	None
6	40–45	11.7 ± 0.8	0	Balance	Cerium oxide (0–1.0)
7	40–45	11.7 ± 0.8	0	Balance	Aluminum oxide (0–1.0)
8	40–45	11.7 ± 0.8	0	Balance	Diamond (0–0.1)
9	40–45	2.2 ± 1.0	0	Balance	Cerium oxide (0–1.0)

*Aqueous MR fluids contain DI water and <1 vol% fluid stabilizers.

†Hardness measured with nanoindentation at 1 and 5 mN; FS nanohardness is 9.9 ± 0.1 Gpa at these loads.^{35,36}

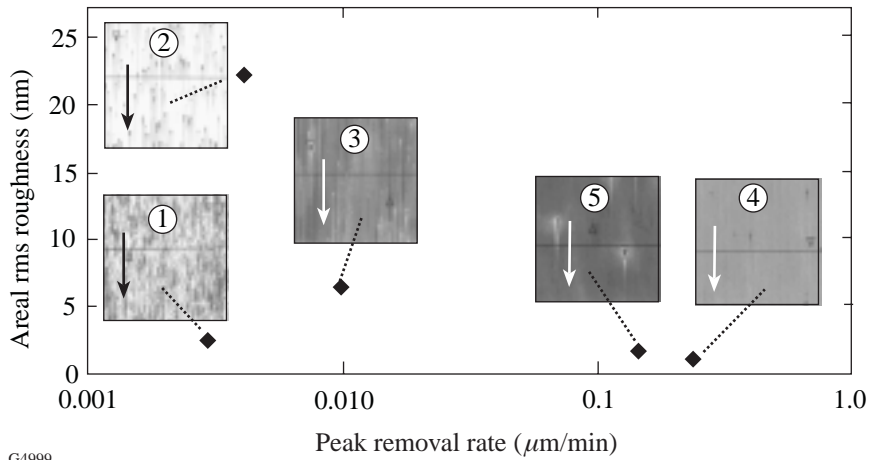


Figure 83.48

Areal ($0.25\text{-mm} \times 0.35\text{-mm}$) rms roughness versus peak removal rate on FS for MR fluids 1 through 5. The soft CI (MR fluid 1) is able to remove material at a very low rate in the absence of the chemical effects of water, but does not pit the surface. The hard CI without water (MR fluid 2) gives low removal and high roughness as the hard CI leaves pits and sleeks in the softer FS surface. The addition of 1 vol% DI water to MR fluid 3 decreases the number of sleeks, which results in a decrease in roughness, and increases removal rate. Fully aqueous MR fluids 4 and 5 show a decrease in pits and sleeks, decrease in roughness, and dramatic increase in removal rate.

G4999

2. Removal Experiments with 40 vol% to 45 vol% CI and Nonmagnetic Nano-Abrasives

Table 83.VIII also lists the composition information for MR fluids 6 through 9. The same hard and soft CI powders that were used in the previous experiments are used here. Table 83.IX summarizes the properties of three different types of nonmagnetic abrasives used in combination with the CI's. These abrasives are nano-cerium oxide,⁴¹ nano-aluminum oxide,⁴² and nano-polycrystalline diamonds.⁴³ The cerium oxide and aluminum oxide abrasives are described in the product literature⁴⁴ as loosely bound agglomerates approximately $10\ \mu\text{m}$ in size. It should be possible to disperse them down to agglomerates of a few hundred nanometers with moderate milling. Cerium oxide from an MR fluid was recently sized after being used in the STM. The mean diameter of the cerium oxide used for 10 days was found to be $0.125\ \mu\text{m}$ and that used for only 2 h was $>0.3\ \mu\text{m}$.⁴⁵ The milling that occurs in the STM among these particles and the CI breaks up any loose agglomerates. The stated primary particle sizes are 37 nm for the alumina and 11 nm for the cerium oxide.^{44,46} The polycrystalline diamonds have a particle size of about $0.125\ \mu\text{m}$ and are made up of crystals approximately 10 nm in size.⁴⁷ The advantage of using these nanoabrasives is that their particle sizes are similar, and they can be introduced in small quantities to the aqueous MR fluid without causing large changes in MR fluid rheology.

Notice from Table 83.VIII that the cerium oxide and aluminum oxide are added in concentrations ranging from 0 vol% to 1.0 vol%, while the diamonds are added in a volume loading up to only 0.1 vol%. This is due to the fact that the diamonds have an immediate and dramatic effect, whereas the other, softer abrasives have a more gradual effect. Also, due to the high cost of diamonds ($\approx \$10/\text{gram}$ versus $\approx \$0.10/\text{gram}$ for cerium oxide), their addition into the MR fluid was halted as soon as

the removal rate appeared to be unaffected by the addition of more diamonds. The difference in the performance of these abrasives is found to be significant even in the small volume loadings given here.

The next step in these experiments is to gradually add the nonmagnetic abrasives into the MR fluid. Figure 83.49 shows the removal rate for FS as a function of cerium oxide concentration for experiments done with MR fluid 6 at a 45 vol% hard CI concentration. The $5\text{-}\mu\text{m} \times 5\text{-}\mu\text{m}$ AFM scans representative of the FS surface at a given concentration of cerium oxide and their cross-sectional profiles are also given in this figure. The 15-nm scale length given in Fig. 83.49 (and Fig. 83.50) is appropriate for each profile in the figure. The AFM scans are shown because their lateral resolution (approximately 20 nm) allows for better characterization of an abrasive's performance than the $0.25\text{-mm} \times 0.35\text{-mm}$ profilometer maps do (lateral resolution = $1.1\ \mu\text{m}$). The white arrows in these AFM scans indicate the direction of flow. The removal rate increases from $0.62\ \mu\text{m}/\text{min}$ with no cerium oxide to $0.94\ \mu\text{m}/\text{min}$ with only 0.05 vol% cerium oxide. Distinct scratches caused by the small amount of cerium oxide in the MR fluid become apparent. The removal rate climbs to $3.01\ \mu\text{m}/\text{min}$ when the cerium oxide concentration is increased 10 \times to 0.5 vol% cerium oxide. The removal rate increases further, to $3.51\ \mu\text{m}/\text{min}$, as the cerium oxide concentration is increased to 1.0 vol%. The areal rms is $0.9 \pm 0.1\ \text{nm}$ for the scans in this figure. It is clear that not only does the cerium oxide become responsible for material removal but also a change in the surface morphology becomes apparent. These scans give more evidence that cerium oxide moves into the layer between the CI and the glass surface and becomes the primary agent for material removal. When cerium oxide is added to the MR fluid, the CI particle is no longer a primary abrasive. The increase in the number of polishing

grooves or scratches caused by the increase in nonmagnetic abrasive concentration is seen for all three types of nonmagnetic abrasives.

Additional information can be gained by considering the differences in morphology of the FS surfaces for the different abrasives used in polishing. Figure 83.50 shows the removal rates from experiments using the MR fluids with 45 vol% hard CI and the maximum loading of the three nano-abrasives used

for these experiments. The lowest removal rate here ($0.62 \mu\text{m}/\text{min}$) is for the MR fluid without nonmagnetic abrasives. When 1.0 vol% aluminum oxide is added, the removal rate increases to $1.0 \mu\text{m}/\text{min}$. Removal rates are even higher for the other nonmagnetic abrasives: $3.51 \mu\text{m}/\text{min}$ for 1.0 vol% cerium oxide, and $4.66 \mu\text{m}/\text{min}$ for 0.1 vol% diamond. An examination of the $5\text{-}\mu\text{m} \times 5\text{-}\mu\text{m}$ AFM maps in Fig. 83.50 shows differences in how these three nonmagnetic abrasives interact with the glass surface. The scan for the MR fluid with 45 vol%

Table 83.IX: Summary of particle size information for the nano-abrasives used.

	Primary Particle Size (nm)	Aggregate Size (μm)	Agglomerate Size (μm)
Cerium Oxide	11	1.5	3.0
Alumina	37	0.3	N/A
Diamond	10	0.125	N/A

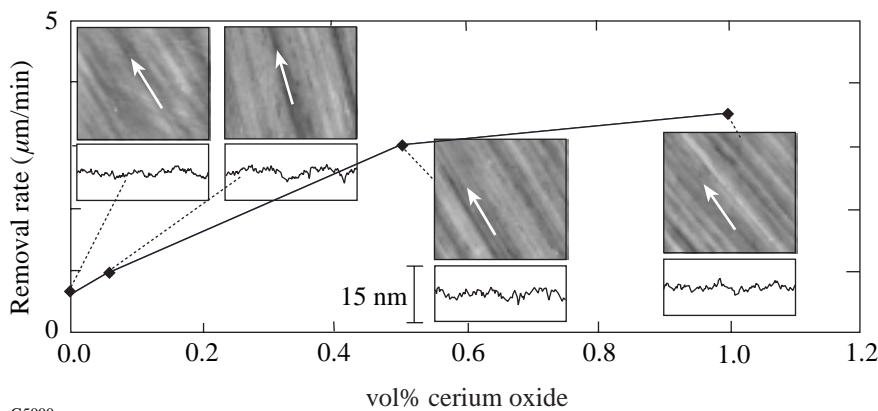


Figure 83.49

Removal rate versus concentration of cerium oxide for experiments using MR fluid 6 (each MR fluid contained 45 vol% hard CI and the aqueous carrier fluid). The removal rate increases with cerium oxide concentration, leveling off at about $3 \mu\text{m}/\text{min}$. The inset AFM scans and accompanying profiles show evolution of the morphology of the FS surface as the abrasive is added. The cerium oxide moves to the interface between the CI and the glass to control removal. The 15-nm scale applies to all profile plots.

G5000

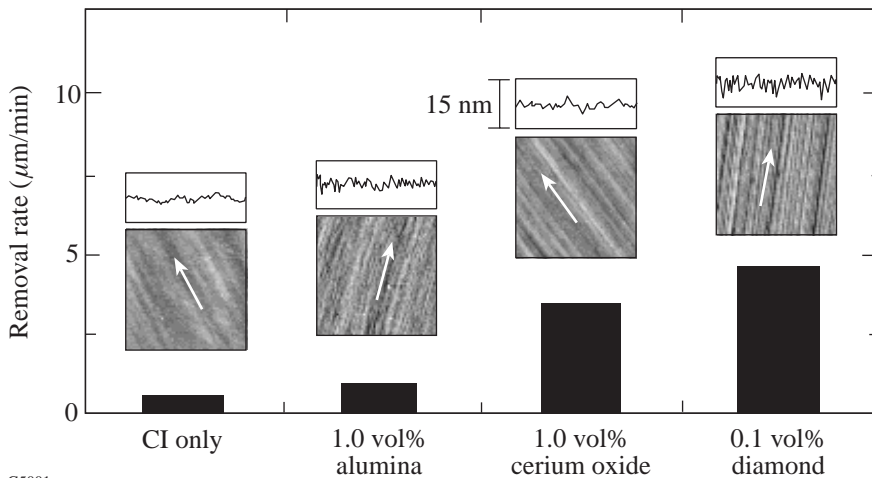


Figure 83.50

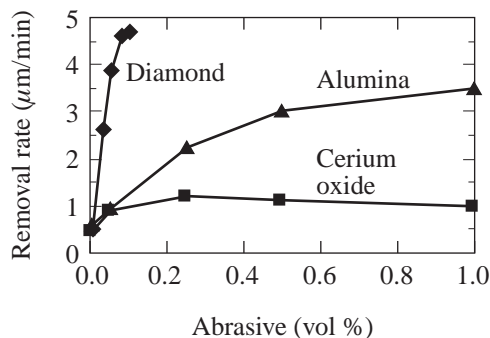
Removal rate as a function of abrasive type for MR fluids with 45 vol% hard CI and the maximum amount of abrasive used during these experiments (only up to 0.1 vol% diamond was used due to its high cost and high removal rates). The three abrasive types affect removal rates to varying degrees due to differences in how each interacts with the FS surface. Aluminum oxide gives deep ($\approx 4 \text{ nm}$) discontinuous grooves; cerium oxide gives shallower (≈ 1 to 2 nm), continuous grooves; and diamond gives deep ($\approx 4 \text{ nm}$) continuous grooves in the direction of flow. Characteristics of the polishing grooves help explain differences in removal rates for the three types of nano-abrasives.

G5001

hard CI without nonmagnetic abrasives is the same scan shown in Fig. 83.49. It has an areal rms of 0.8 nm. The aluminum oxide does not appear to continuously scratch the surface; instead, there appear to be several small discontinuous scratches at the FS surface. This leads to the lowest removal rates for the MR fluids containing nonmagnetic abrasives and an areal rms roughness of 1.2 nm. The cerium oxide gives wide, continuous scratches over the scanned region and an rms roughness of 0.9 nm. Finally, the diamond gives distinct narrow, continuous scratches along the direction of flow. The areal rms roughness for this scan is 1.4 nm. More differences in the behaviors of the abrasives are observed and are discussed below.

Differences in the Mechanics of Removal for Aqueous MR Fluids

Figure 83.51 shows the removal rate for MR fluids made up of 45 vol% hard CI and increasing amounts of nonmagnetic abrasives. Small amounts of diamond cause dramatic increases in removal rates. Cerium oxide increases removal to a lesser degree, and the aluminum oxide increases removal to an even lesser degree. These removal rates tend to level off at higher nonmagnetic abrasive concentrations. A certain minimum amount of nonmagnetic abrasive is needed to maximize the effectiveness, but there is a point where the addition of more abrasive has little or no effect on the removal rate. This has been shown to be true in more conventional polishing methods as well. Izumitani⁴ showed a maximum in polishing efficiency of BK7 glass at about 1.5 vol% (10 wt%) cerium oxide. It is not clear whether this polishing was done on pitch or on a polyure-



G5002

Figure 83.51

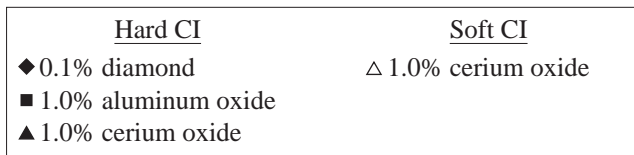
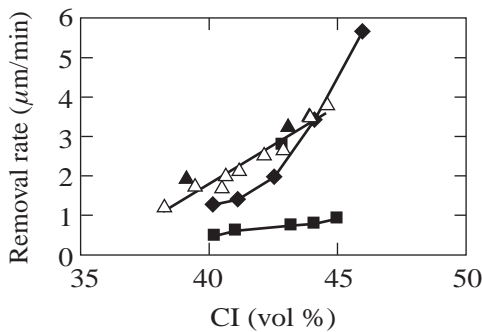
Removal rate versus vol% abrasive for 45 vol% hard CI and the aqueous carrier fluid. The diamonds are shown to have an immediate impact, dramatically increasing removal with less than 0.1 vol% concentration. The cerium oxide gradually increases removal. The aluminum oxide proves ineffective at increasing removal rates.

thane lap. Silvernail and Goetzinger⁸ show similar behavior on felt and Pellon laps. Their result depends on the applied pressure, but most of their removal rates level off above 1.5 vol% cerium oxide. Presumably this means that once the contact zone between the CI and the glass surface is saturated with nonmagnetic abrasive, further addition of abrasives is unnecessary.

The reason for the relative effectiveness of each particle type is not clear, but these results do agree with AFM measurements as well as with the experiments with nonaqueous MR fluids. The cerium oxide grooves are approximately 1 nm to 2 nm deep, whereas the aluminum oxide and diamond grooves are approximately 4 nm deep.⁴⁰ The diamonds, the hardest particles, exhibit distinct continuous scratches, which leads to high removal rates. The cerium oxide also scratches the material in a continuous manner, but the scratches are less severe, which leads to an intermediate removal rate. The lowest removal rate is for the aluminum oxide particles, even though they give features deeper than those from cerium oxide and as deep as those from diamond. The scratches associated with these aluminum oxide particles are discontinuous. The relative hardness values of the aluminum oxide and cerium oxide particles are not known because these particles are too small for nanoindentation experiments. Nanohardness tests done in a previous work³⁵ showed that it is possible for an aluminum oxide particle to be either very much harder than a cerium oxide particle or of comparable hardness. Even if the relative hardness values are not known, however, differences in removal rates should not be surprising after viewing the AFM scans. The continuity of contact between the abrasives and glass surface is important for high removal rates.⁶ The diamond and cerium oxide have this continuous contact while the aluminum oxide does not. The previous study³⁶ with the nonaqueous MR fluids without nonmagnetic abrasives (MR fluids 1 and 2) gave a similar result. The soft CI removed material from BK7 and LHG8 more efficiently than the hard CI. This trend changed somewhat when FS was used, probably because removal rates were so low and the hardness of FS is nearly the same as the hard CI. The proposed phenomenological explanation was that the soft CI could not penetrate the surface and was able to maintain contact with a shallow surface layer. The hard CI gave sleeks and pits and seemed to “skip” along the surface, causing discontinuity of contact between the abrasive and the glass surface. The reduced removal rate for aluminum oxide caused by discontinuity of abrasive/glass contact is consistent with these results. This may also be a partial explanation as to why Kaller¹⁵ recommends abrasives that are softer than the bulk material and Izumitani⁴ recommends abrasives with the same hardness of the hydrated layer.

Several references support these relative removal rates. The aqueous MR fluids have an approximate pH of 9. In Ref. 10 Cook analyzes work from others that shows cerium oxide is a much more efficient polisher than aluminum oxide in the pH range of 7 to 9. Cumbo¹¹ shows that cerium oxide has a higher removal rate on FS than aluminum oxide on FS at pH 10. Kaller and Cook give possible explanations for the effectiveness of cerium oxide. Kaller¹⁵ explains that lattice defects in cerium oxide crystals allow cerium oxide to grip the material better and therefore enhance removal rates. Cook's¹⁰ explanation is that the near neutral charge on the cerium oxide surface at this pH improves its ion exchange ability. The increased removal rate for diamond could be due to similar reasons. Its high hardness gives an explanation for the deep, distinct polishing grooves. The continuous contact maintained by the diamond could be explained by the fact that these diamonds are created by an explosion process,⁴⁷ which would likely result in many lattice defects. Kaller's explanation for cerium oxide provides support for the efficient removal seen with the MR fluids with diamond abrasives.

Figure 83.52 shows the removal rate as a function of CI concentration at the maximum nonmagnetic abrasive concentrations for the three abrasives used during these experiments. Notice that the data for MR fluids 6 (hard CI and cerium oxide)



G5003

Figure 83.52 Effect of the CI concentration on removal with maximum amount of abrasive present. Once again the diamonds prove to be the most efficient, reacting strongest to the increase in CI concentration. The cerium oxide data consist of both hard and soft CI. This shows that the hardness of CI is unimportant in the presence of the abrasive.

and 9 (soft CI and cerium oxide) coincide. This is more evidence that the type of CI is unimportant in aqueous environments with nonmagnetic abrasives, when the CI acts only as a lap. This plot shows the general trend that an increase in CI concentration leads to higher removal rates and that the relative increase in removal rate is largely related to the abrasive type. The nonmagnetic abrasives efficiently increase removal rate and decrease roughness. The diamonds are 10× more efficient than cerium oxide and aluminum oxide.

Figure 83.53 shows how the removal rate changes with pressure and drag force (pressure and drag force changed as a result of varying CI concentration but keeping the nonmagnetic abrasive concentration and wheel velocity constant). Figure 83.53(a) shows the removal rate as a function of drag force at the maximum nonmagnetic abrasive concentration used for these experiments. Figure 83.53(b) shows the removal rate as a function of the peak pressure. Both drag force and pressure scale with removal rate in a linear way, which is consistent with considerations such as Preston's equation⁶ discussed at the beginning of this article. The slopes of these lines (related to a Preston-type coefficient) depend on the type of abrasive used. The linear fits for the drag force tend to go through the origin, whereas they do not for the pressure. This supports the theory that in MRF the shear stress controls removal of material.

The drag force as a function of nonmagnetic abrasive content at a constant CI concentration is plotted in Fig. 83.54 for MR fluids 6, 7, and 8. As nonmagnetic abrasives are added, the drag force is reduced. This is once again consistent with the idea that nonmagnetic abrasives move to the region between the CI and the glass surface. All of the curves start at approximately the same initial drag force of about 5.5 N without nonmagnetic abrasive. While the MR fluid lap yields and conforms to the part surface, the magnetic field gives it a certain rigidity that makes it relatively difficult to shear. It is almost a two-body abrasion problem. This changes when nonmagnetic abrasives are added. They are forced to the glass surface because of the gradient in the magnetic field. At this point, the process becomes a three-body abrasion system. The magnetically stiffened CI forms the polishing lap that supports the free abrasives against the glass surface. This is similar to loose abrasive polishing on a conformal lap.

Consider the relative reductions in the drag force. The diamonds are seen to reduce the drag force dramatically, while increasing the removal rate just as dramatically. Adding aluminum oxide to the MR fluid also significantly reduces the drag

force, but adding cerium oxide has very little effect. This does not correlate with removal but may be interesting for a different reason. Several authors (see, for example, Refs. 10 and 15) hypothesize that one of the reasons cerium oxide is a successful polishing agent is because of its ability to chemically bond with the glass surface. This plot may begin to give physical evidence of this phenomenon.

All of these results suggest the use of a modified Preston equation to describe material removal in MRF. Consider Eq. (2). If a coefficient of friction is pulled out of C_p , it can be written as

$$\frac{dz}{dt} = C'_p \frac{\mu L}{A} \frac{ds}{dt} \tag{3}$$

The term C'_p is a new Preston coefficient and μ is a coefficient of friction. The friction coefficient multiplied by a normal load gives a drag force (F_D) and Eq. (3) becomes

$$\frac{dz}{dt} = C'_p \frac{F_D}{A} \frac{ds}{dt} \tag{4}$$

Finally, if this is considered over a very small volume of material (see callout on right in Fig. 83.46), the term F_D/A is simply the local shear stress at the part surface. This would give a removal rate description similar to Preston's equation based on the local shear stress (τ) at the part surface

$$\frac{dz}{dt} = C'_p \tau \frac{ds}{dt} \tag{5}$$

Previous work^{22,23} has shown that spot profiles are consistent with the shear stress distribution at the part surface. The remaining two terms in Eq. (5) are not yet fully understood. The relative velocity (ds/dt) is difficult to define in MRF. This velocity could be the relative velocity between the wheel and the part surface, but since the CI in the MR fluid actually supplies the lap, it is more correct that ds/dt is the relative velocity between the CI and the glass surface. This is not easily determined at this time. In fact, the behavior of the different abrasives in different MR fluids may indicate that this relative velocity depends on the abrasive type used. The wheel velocity was the same for all of the experiments described here, so this term was held as constant as possible in terms of controllable experimental parameters.

This work has also shown that, as for other polishing processes, it is difficult to define the Preston coefficient (C'_p) in MRF. This term contains information on the chemistry of the carrier fluid, abrasive type, and glass type. Lambropoulos *et al.*³ showed that the removal rate in MRF is proportional to the term $E/K_c H_K^2$ of the glass (E = elastic modulus, K_c = fracture toughness, and H_K = Knoop hardness of the glass). The experiments described here show that the removal rate depends on the abrasive type as well as the concentration. As a result, this coefficient would also have to contain information about the abrasive type used for a given MR fluid (probably size, shape, and hardness as well as the tribochemical "gripping"¹⁵ power). Finally, it was shown that the presence of DI water dramatically changes how the abrasive interacts with the glass surface. Therefore, information on the chemical make-up of the carrier fluid must also be contained in this coefficient.

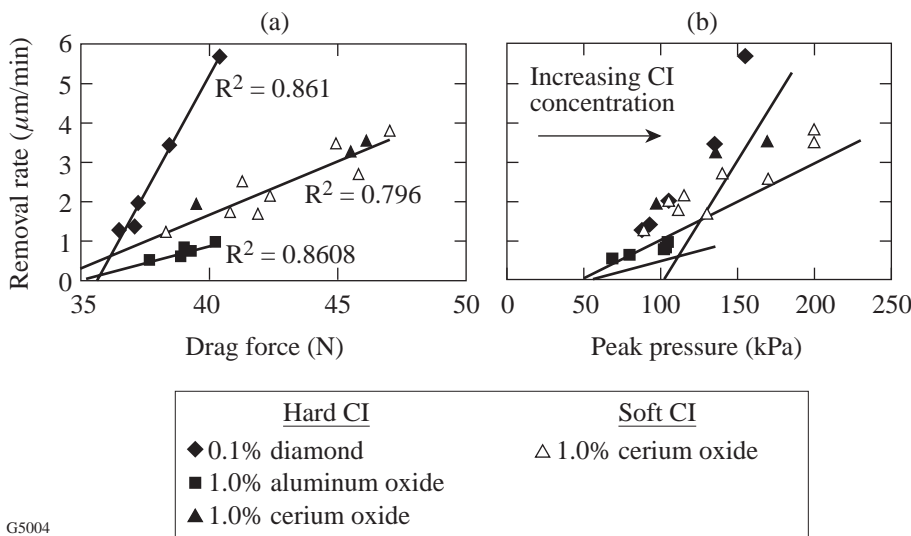
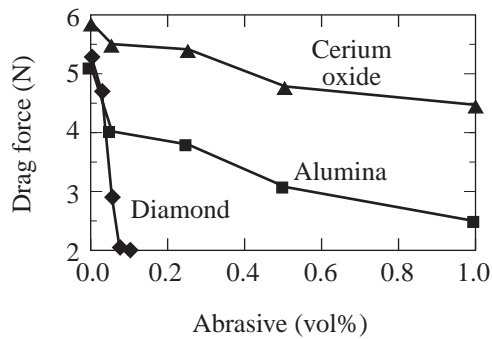


Figure 83.53 Removal rate versus drag force (a), and removal rate versus peak pressure (b). Removal rate increases linearly with pressure and drag force. The linear fits for the drag force go through the origin with high correlation coefficients, but do not for the pressure. This means that there can be removal with a nonzero pressure, but with no drag force (therefore no shear stress) there will be no removal. This supports the idea that shear stress controls removal rate in MRF.

G5004



G5005

Figure 83.54

Effect of adding abrasive to MR fluids 4, 5, and 6 containing 45 vol% CI. In each case the addition of abrasive reduces the drag force, supporting the idea that MRF becomes a three-body abrasion problem. The cerium oxide maintains a high drag force, which supports the theories that cerium oxide has “chemical tooth.”

Summary

The mechanisms of material removal in MRF have been presented. Previous work describes how the shear stress due to the hydrodynamic flow of the MR fluid between the rotating wheel and the part surface controls the removal rate. The idea that material removal depends on the shear stress at the part surface is supported by the linear relation between removal rate and the total drag force shown here. It has also been shown previously that the nanohardness of the CI is important in material removal with nonaqueous MR fluids. We show here that as DI water is added to the MR fluid, the differences in the behavior of the hard and soft CI become less significant as the removal rate dramatically increases for both. This is due to either the presence of a hydrated layer or reduced fracture toughness of the glass in aqueous MR fluids. The addition of nonmagnetic nano-abrasives increases removal rates further since they move to the interface between the CI and the glass surface to control material removal. A transition from two-body to three-body removal is hypothesized. The relative increase in removal depends on the amount and type of the abrasive since different abrasives interact with the glass surface in different ways. This behavior of the abrasive is evident from both AFM scans as well as drag force measurements. More work should allow these results to be summarized in a modified Preston equation based on the local shear stress at the part surface.

ACKNOWLEDGMENT

The authors would like to thank Rebecca Coppens, Henry Romanofsky, Leslie Gregg, Irina Kozhinova, Steven Arrasmith, Caleb Farny, and Susan Brandt of the Center for Optics Manufacturing for their help in this work. We

would also like to thank Alexander Maltsev of LLE for his assistance in sample preparation. Support for this work was provided in part by the Center for Optics Manufacturing (COM), QED Technologies, U.S. Army Materiel Command, and DARPA (Defense Advanced Research Project Agency).

REFERENCES

1. M. J. Cumbo, “Chemo-Mechanical Interactions in Optical Polishing (Glass Finishing),” Ph.D. thesis, University of Rochester, 1993, Chap. 1.
2. M. Buijs and K. Korpel-van Houten, *J. Mater. Sci.* **28**, 3014 (1993).
3. J. C. Lambropoulos, S. D. Jacobs, and J. Ruckman, in *Finishing of Advanced Ceramics and Glasses*, edited by R. Sabia, V. A. Greenhut, and C. G. Pantano, Ceramic Transactions, Vol. 102 (The American Ceramic Society, Westerville, OH, 1999), pp. 113–128.
4. T. S. Izumitani, *Optical Glass*, American Institute of Physics Translation Series (American Institute of Physics, New York, 1986), Chap. 4, pp. 92–98.
5. A. Kaller, *Glastech. Ber.* **64**, 241 (1991).
6. F. W. Preston, *J. Soc. Glass Technol.* **XI**, 214 (1927).
7. W. L. Silvernail and N. J. Goetzinger, *The Glass Industry* **52**, 130 (1971).
8. *ibid.*, 172.
9. T. A. Michalske and B. C. Bunker, *J. Am. Ceram. Soc.* **76**, 2613 (1993).
10. L. M. Cook, *J. Non-Cryst. Solids* **120**, 152 (1990).
11. M. J. Cumbo, D. Fairhurst, S. D. Jacobs, and B. E. Puchebner, *Appl. Opt.* **34**, 3743 (1995).
12. H. Yokota *et al.*, *Surf. Sci.* **16**, 265 (1969).
13. M. Maaza *et al.*, *Opt. Commun.* **100**, 220 (1993).
14. A. B. Shorey, K. Xin, K.-H. Chen, and J. C. Lambropoulos, in *Inorganic Optical Materials*, edited by A. J. Marker III (SPIE, Bellingham, WA, 1998), Vol. 3424, pp. 72–81.
15. A. Kaller, *Glass Sci. Technol.* **71**, 174 (1998).
16. N. B. Kirk and J. V. Wood, *J. Mater. Sci.* **30**, 2171 (1995).
17. D. Golini, S. Jacobs, W. Kordonski, and P. Dumas, in *Advanced Materials for Optics and Precision Structures*, edited by M. A. Ealey, R. A. Paquin, and T. B. Parsonage, Critical Reviews of Optical Science and Technology (SPIE, Bellingham, WA, 1997), Vol. CR67, pp. 251–274.
18. S. D. Jacobs, S. R. Arrasmith, I. A. Kozhinova, L. L. Gregg, A. B. Shorey, H. J. Romanofsky, D. Golini, W. I. Kordonski, P. Dumas, and S. Hogan, in *Finishing of Advanced Ceramics and Glasses*, edited by R. Sabia, V. A. Greenhut, and C. G. Pantano, Ceramic Transactions, Vol. 102 (The American Ceramic Society, Westerville, OH, 1999), pp. 185–199.

19. S. R. Arrasmith, I. A. Kozhina, L. L. Gregg, A. B. Shorey, H. J. Romanofsky, S. D. Jacobs, D. Golini, W. I. Kordonski, S. J. Hogan, and P. Dumas, in *Optical Manufacturing and Testing III*, edited by H. P. Stahl (SPIE, Bellingham, WA, 1999), Vol. 3782, pp. 92–100.
20. S. D. Jacobs, W. Kordonski, I. V. Prokhorov, D. Golini, G. R. Gorodkin, and T. D. Strafford, "Magnetorheological Fluid Composition," U.S. Patent No. 5,804,095 (8 September 1998).
21. Zygo Mark IVxp™ or Zygo GPI xpHR™ phase-shifting interferometer system was used for all data acquisition and analysis related to polishing spots, HeNe laser source with $\lambda = 632.8$ nm, Zygo Corporation, Middlefield, CT 06455.
22. V. W. Kordonski, D. Golini, P. Dumas, S. J. Hogan, and S. D. Jacobs, in *Smart Structures and Materials 1998: Industrial and Commercial Applications of Smart Structures Technologies*, edited by J. M. Sater (SPIE, Bellingham, WA, 1998), Vol. 3326, pp. 527–535.
23. A. B. Shorey, "Mechanisms of Material Removal in Magnetorheological Finishing (MRF) of Glass," Ph.D. thesis, University of Rochester, 2000, Chap. 3.
24. *ibid.*, Chap. 2.
25. A. B. Shorey, W. I. Kordonski, S. R. Gorodkin, S. D. Jacobs, R. F. Gans, K. M. Kwong, and C. H. Farney, *Rev. Sci. Instrum.* **70**, 4200 (1999).
26. Q22, QED Technologies, LLC, Rochester, NY 14607.
27. Field measurements were taken with the F. W. Bell Model 9500 Gaussmeter, Bell Technologies Inc., Ontario, FL 32807.
28. Computrac Max-1000 moisture analyzer, Arizona Instruments, Phoenix, AZ 85040-1941.
29. Brookfield DV-III cone and plate viscometer, Brookfield Engineering Laboratories, Inc., Stoughton, MA 02072.
30. Zygo NewView™ White Light Optical Profiler, areal over 0.25 mm \times 0.35 mm with a 20 \times Mirau objective, 1.1- μ m lateral resolution, Zygo Corporation, Middlefield CT 06455.
31. Nanoprobe III atomic force microscope (AFM), Digital Instruments, Santa Barbara, CA 93117.
32. Measured with the I-scan pressure measurement system, Tekscan, Inc., Boston, MA 02127. We used a 0.1-mm-thick 5051 pressure film with a maximum allowable load of 345 kPa (50 psi) and a lateral resolution of 1.27 mm.
33. Linear ball slide, Parker Hannafin Corporation, Cleveland, OH 44124-4141.
34. LKCP475 5-lb load cell, Cooper Instruments, Warrenton, VA 20188.
35. A. B. Shorey, K. M. Kwong, K. M. Johnson, and S. D. Jacobs, *Appl. Opt.* **39**, 5194 (2000).
36. A. B. Shorey, L. L. Gregg, H. J. Romanofsky, S. R. Arrasmith, I. Kozhina, J. Hubregesen, and S. D. Jacobs, in *Optical Manufacturing and Testing III*, edited by H. Stahl (SPIE, Bellingham, WA, 1999), Vol. 3782, pp. 101–111.
37. Corning 7940, Corning, Inc., Corning, NY 14831-0002.
38. R. S. Higgins and S. A. Kilinger, *High Purity Solvent Guide*, 3rd ed. (Baxter Diagnostics, Muskegon, MI, 1990).
39. Brookfield DV-II Digital Viscometer, Brookfield Engineering Laboratories, Inc., Stoughton, MA 02072.
40. A. B. Shorey, "Mechanisms of Material Removal in Magnetorheological Finishing (MRF) of Glass," Ph.D. thesis, University of Rochester, 2000, Chap. 5.
41. NanoTek Cerium Oxide, Nanophase Technologies Corporation, Burr Ridge, IL 60521.
42. NanoTek Aluminum Oxide, Nanophase Technologies Corporation, Burr Ridge, IL 60521.
43. 0.125- μ m Hyprez-type PC diamonds, Engis Corporation, Wheeling, IL 60090.
44. NanoTek Cerium Oxide and Aluminum Oxide product literature of Nanophase Technologies Corporation, Burr Ridge, IL 60521, <http://www.nanophase.com/products.shtml>.
45. I. Kozhina, L. Gregg, and J. Hesterman, "CPD-012 Cerium Oxide Powder Particle Size Measurements Using the Variety of Relative Refractive Indexes," Magnetorheological Finishing Laboratory internal report, Center for Optics Manufacturing, Rochester, NY, 25 February 2000.
46. "Fundamentals of Particle Sizing," product literature of Nanophase Technologies Corporation, Burr Ridge, IL 60521.
47. Engis diamond product literature, Engis Corporation, Wheeling, IL 60090, <http://www.engis.com/hyprez/powders.html>.

Publications and Conference Presentations

Publications

- R. Betti and J. P. Freidberg, "Radial Discontinuities in Tokamak Magnetohydrodynamic Equilibria with Poloidal Flow," *Phys. Plasmas* **7**, 2439 (2000).
- J. L. Chaloupka and D. D. Meyerhofer, "Characterization of a Tunable, Single-Beam Ponderomotive-Optical Trap," *J. Opt. Soc. Am. B* **17**, 713 (2000).
- T. J. B. Collins, H. L. Helfer, and H. M. VanHorn, "Oscillations of Accretion Disks and Boundary Layers in Cataclysmic Variables: I. Unperturbed, Steady-Flow Models," *Astrophys. J.* **534**, 934 (2000).
- T. J. B. Collins, H. L. Helfer, and H. M. VanHorn, "Oscillations of Accretion Disks and Boundary Layers in Cataclysmic Variables: II. A Local, Linear Stability Analysis of Accretion Disk Boundary Layers," *Astrophys. J.* **534**, 944 (2000).
- F. Dahmani, A. W. Schmid, J. C. Lambropoulos, S. J. Burns, and S. Papernov, "Lifetime Prediction of Laser-Pre-cracked Fused Silica Subjected to Subsequent Cyclic Laser Pulses," *J. Mater. Res.* **15**, 1182 (2000).
- V. N. Goncharov, S. Skupsky, T. R. Boehly, J. P. Knauer, P. W. McKenty, V. A. Smalyuk, R. P. J. Town, O. V. Gotchev, R. Betti, and D. D. Meyerhofer, "A Model of Laser Imprinting," *Phys. Plasmas* **7**, 2062 (2000) (invited).
- V. N. Goncharov, S. Skupsky, P. W. McKenty, J. A. Delettrez, R. P. J. Town, and C. Cherfiles-Cl rouin, "Stability Analysis of Directly Driven NIF Capsules," in *Inertial Fusion Sciences and Applications (IFSA 99): State of the Art 1999*, edited by C. Labaune, W. J. Hogan, and K. A. Tanaka (Elsevier, Paris, 2000), pp. 214–219.
- S. R. Gorodkin, W. I. Kordonski, E. V. Medvedeva, Z. A. Novikova, A. B. Shorey, and S. D. Jacobs, "A Method and Device for Measurement of a Sedimentation Constant of Magnetorheological Fluids," *Rev. Sci. Instrum.* **71**, 2476 (2000).
- K. S. Il'in, M. Lindgren, M. Currie, A. D. Semenov, G. N. Gol'tsman, R. Sobolewski, S. I. Cherednichenko, and E. M. Gershenson, "Picosecond Hot-Electron Energy Relaxation in NbN Superconducting Photodetectors," *Appl. Phys. Lett.* **76**, 2752 (2000).
- C. K. Li, D. G. Hicks, F. H. S guin, J. A. Frenje, R. D. Petrasso, J. M. Soures, P. B. Radha, V. Yu. Glebov, C. Stoeckl, J. P. Knauer, R. Kremens, F. J. Marshall, D. D. Meyerhofer, S. Skupsky, S. Roberts, C. Sorce, T. C. Sangster, T. W. Phillips, M. D. Cable, and R. J. Leeper, "D-³He Proton Spectra for Diagnosing Shell ρR and Fuel T_i of Imploded Capsules at OMEGA," *Phys. Plasmas* **7**, 2578 (2000).
- F. J. Marshall, J. A. Delettrez, R. Epstein, V. Yu. Glebov, D. R. Harding, P. W. McKenty, D. D. Meyerhofer, P. B. Radha, W. Seka, S. Skupsky, V. A. Smalyuk, J. M. Soures, C. Stoeckl, R. P. J. Town, B. Yaakobi, C. K. Li, F. H. S guin, D. G. Hicks, and R. D. Petrasso, "Direct-Drive, High-Convergence-Ratio Implosion Studies on the OMEGA Laser System," *Phys. Plasmas* **7**, 2108 (2000).
- R. L. McCrory, R. E. Bahr, T. R. Boehly, T. J. B. Collins, R. S. Craxton, J. A. Delettrez, W. R. Donaldson, R. Epstein, V. N. Goncharov, R. Q. Gram, D. R. Harding, P. A. Jaanimagi, R. L. Keck, J. P. Knauer, S. J. Loucks, F. J. Marshall, P. W. McKenty, D. D. Meyerhofer, S. F. B. Morse, O. V. Gotchev, P. B. Radha, S. Regan, W. Seka, S. Skupsky, V. A. Smalyuk, J. M. Soures, C. Stoeckl, R. P. J. Town, M. D. Wittman, B. Yaakobi, J. D. Zuegel, R. D. Petrasso, D. G. Hicks, and C. K. Li, "OMEGA Experiments and Preparation for Moderate-Gain Direct-Drive Experiments on the NIF," in *Inertial Fusion Sciences and Applications (IFSA 99): State of the Art 1999*, edited by C. Labaune, W. J. Hogan, and K. A. Tanaka (Elsevier, Paris, 2000), pp. 43–53.

A. V. Okishev, M. D. Skeldon, R. L. Keck, and W. Seka, "All-Solid-State Optical Pulse Shaper for the OMEGA Laser Fusion Facility," in *Advanced Solid State Lasers*, edited by H. Injeyan, U. Keller, and C. Marshall, OSA Trends in Optics and Photonics, Vol. 34 (Optical Society of America, Washington, DC, 2000), pp. 30–32.

P. B. Radha, S. Skupsky, R. D. Petrasso, and J. M. Soures, "A Novel Charged-Particle Diagnostic for Compression in ICF Targets," *Phys. Plasmas* **7**, 1531 (2000).

W. S. Varnum, N. D. Delamater, S. C. Evans, P. L. Gobby, J. E. Moore, J. M. Wallace, R. G. Watt, J. D. Colvin, R. Turner, V. Glebov, J. Soures, and C. Stoeckl, "Progress Toward Ignition with Noncryogenic Double-Shell Capsules," *Phys. Rev. Lett.* **84**, 5152 (2000).

B. Yaakobi, V. A. Smalyuk, J. A. Delettrez, R. P. J. Town, F. J. Marshall, V. Yu. Glebov, R. D. Petrasso, J. M. Soures, D. D. Meyerhofer, and W. Seka, "Spherical Implosion Experiments on OMEGA: Measurements of the Cold, Compressed Shell," in *Inertial Fusion Sciences and Applications (IFSA 99): State of the Art 1999*, edited by C. Labaune, W. J. Hogan, and K. A. Tanaka (Elsevier, Paris, 2000), pp. 115–121.

J. D. Zuegel, D. Jacobs-Perkins, J. A. Marozas, R. G. Roides, W. Bittle, E. M. R. Michaels, S. Regan, R. S. Craxton, J. H. Kelly, T. J. Kessler, W. Seka, and S. Skupsky, "Broadband Beam Smoothing on OMEGA with Two-Dimensional Smoothing by Spectral Dispersion," in *Inertial Fusion Sciences and Applications (IFSA 99): State of the Art 1999*, edited by C. Labaune, W. J. Hogan, and K. A. Tanaka (Elsevier, Paris, 2000), pp. 664–668.

Forthcoming Publications

E. L. Alfonso, I. Anteby, and D. R. Harding, "Temperature Profiles and $\ell = 1$ Nonuniformity Within Cryogenic ICF Targets," to be published in *Fusion Technology*.

S. R. Arrasmith, S. D. Jacobs, I. A. Kozhinova, A. B. Shorey, D. Golini, W. I. Kordonski, S. Hogan, and P. Dumas, "Development and Characterization of Magnetorheological Fluids for Optical Finishing," to be published in the *Proceedings of Fine Powder Processing '99*, University Park, PA, 20–22 September 1999.

A. Babushkin, M. J. Harvey, and M. D. Skeldon, "The Output Signal-to-Noise Ratio of a Nd:YLF Regenerative Amplifier," to be published in *Optics Letters*.

R. Betti and J. P. Freidberg, "Low- β , Magnetohydrodynamic Tokamak Equilibria with Poloidal Transonic Flow," to be published in *Physical Review Letters*.

T. R. Boehly, A. Babushkin, D. K. Bradley, R. S. Craxton, J. A. Delettrez, R. Epstein, T. J. Kessler, J. P. Knauer, R. L. McCrory, P. W. McKenty, D. D. Meyerhofer, S. Regan, W. Seka, S. Skupsky, V. A. Smalyuk, R. P. J. Town, and B. Yaakobi, "Laser-Uniformity and Hydrodynamic-Stability Experiments at the OMEGA Laser Facility," to be published in *Laser and Particle Beams*.

T. R. Boehly, Y. Fisher, D. D. Meyerhofer, W. Seka, J. M. Soures, and D. K. Bradley, "The Effect of Optical Prepulses

on the Performance of Direct-Drive Inertial Confinement Fusion Targets," to be published in *Physics of Plasmas*.

T. R. Boehly, V. N. Goncharov, O. Gotchev, J. P. Knauer, D. D. Meyerhofer, D. Oron, S. P. Regan, Y. Srebro, W. Seka, D. Shvarts, S. Skupsky, and V. A. Smalyuk, "The Effect of Pulse Shape on Laser Imprinting and Beam Smoothing," to be published in *Physical Review Letters*.

D. P. Butler, Z. Celik-Butler, and R. Sobolewski, "Y-Ba-Cu-O as an Infrared Radiation Sensing Material," to be published in the *Handbook of Advanced Electronic and Photonic Materials* (Academic Press, NY).

H. P. Chen, D. Katsis, J. C. Mastrangelo, S. H. Chen, S. D. Jacobs, and P. J. Hood, "Glassy Liquid-Crystal Films with Opposite Chirality as High-Performance Optical Notch Filters," to be published in *Advanced Materials*.

H. P. Chen, D. Katsis, J. C. Mastrangelo, K. L. Marshall, S. H. Chen, and T. H. Mourey, "Thermotropic Chiral-Nematic Poly (*P*-Phenylene)s as a Paradigm of Helically Stacked π -Conjugated Systems," to be published in *Chemistry of Materials*.

F.-Y. Fan, J. C. Mastrangelo, D. Katsis, and S.-H. Chen, "Novel Glass-Forming Liquid Crystals: V. Nematic and Chiral-Nematic Systems with an Elevated Glass Transition Temperature," to be published in *Liquid Crystals*.

W. Göb, W. Liebich, W. Lang, I. Puica, R. Sobolewski, R. Rossler, J. D. Pedarnig, and D. Bauerle, "Double Sign Reversal of the Vortex Hall Effect in $\text{YBa}_2\text{Cu}_3\text{O}_{7-\delta}$ Thin Films in the Strong Pinning Limit of Low Magnetic Fields," to be published in *Physical Review B*.

G. N. Gol'tsman, G. Chulkova, A. Dzardanov, A. Lipatov, O. Okunev, A. Semenov, K. Smirnov, B. Voronov, C. Williams, and R. Sobolewski, "Picosecond Superconducting Single-Photon Optical Detector," to be published in *Nature*.

V. N. Goncharov, P. W. McKenty, S. Skupsky, R. P. J. Town, R. Betti, and C. Cherfils-Clérouin, "Modeling Hydrodynamic Instabilities in Inertial Confinement Fusion Targets," to be published in *Physics of Plasmas*.

K. Green and R. Sobolewski, "Extending Scattering Parameter Approach to Characterization of Linear Time-Varying Microwave Devices," to be published in *IEEE Transactions on Microwave Theory and Techniques*.

M. J. Guardalben and N. Jain, "Phase-Shift Error Caused by Molecular Alignment Distortions in a Liquid Crystal Point-Diffraction Interferometer," to be published in *Optics Letters*.

S. D. Jacobs, "Take-Home Demo Excites Young People About Careers in Technology," to be published in *Optics and Photonics News*.

P. W. McKenty, M. D. Wittman, and V. N. Goncharov, "Characterization of Thick Cryogenic Fuel Layers Using Convergent-Beam Interferometry: A Numerical Investigation," to be published in the *Journal of Applied Physics*.

S. P. Regan, J. A. Marozas, J. H. Kelly, T. R. Boehly, W. R. Donaldson, P. A. Jaanimagi, R. L. Keck, T. J. Kessler, D. D. Meyerhofer, W. Seka, S. Skupsky, and V. A. Smalyuk, "Experimental Investigation of Smoothing by Spectral Dispersion," to be published in the *Journal of the Optical Society of America B*.

F. H. Séguin, C. K. Li, D. G. Hicks, J. A. Frenje, R. D. Petrasso, J. M. Soures, V. Yu. Glebov, C. Stoeckl, P. B. Radha, D. D. Meyerhofer, S. Roberts, C. Sorce, T. C. Sangster, and M. D. Cable, "Diagnostic Use of Secondary $\text{D-}^3\text{He}$ Proton Spectra for D-D OMEGA Targets," to be published in *Physics of Plasmas*.

A. B. Shorey, K. M. Kwong, K. M. Johnson, and S. D. Jacobs, "Nanoindentation Hardness of Particles Used in Magneto-rheological Finishing (MRF)," to be published in *Applied Optics*.

R. W. Short, "Stability of Self-Focused Filaments in Laser-Produced Plasmas," to be published in *Physical Review Letters*.

M. D. Skeldon, "A High-Bandwidth Electrical-Waveform Generator Based on an Aperture-Coupled Stripline," to be published in the *Review of Scientific Instruments*.

V. A. Smalyuk, B. Yaakobi, F. J. Marshall, and D. D. Meyerhofer, "X-Ray Spectroscopic Measurements of Areal Density and Modulations in Areal Density of Cold Compressed Shells in Implosion Experiments on OMEGA," to be published in the *Proceedings of the 12th Topical Conference on Atomic Processes in Plasmas*, Reno, NV, 19–23 March 2000.

D. J. Smith, J. A. Warner, N. E. LeBarron, T. J. Kessler, and S. LaDelia, "The Development of Ion-Etched Phase Plates," to be published in *Applied Optics*.

R. Sobolewski, "Time-Resolved Nonequilibrium Phenomena in High-Temperature Superconductors," to be published in the *Proceedings of the International Workshop on Superconductivity, Magneto-Resistive Materials, and Strongly Correlated Quantum Systems*, Hanoi, Vietnam, June 1999 (invited).

F.-Y. Tsai, E. L. Alfonso, S.-H. Chen, and D. R. Harding, "Mechanical Properties and Gas Permeability of Polyimide Shells Fabricated by the Vapor Deposition Method," to be published in *Fusion Technology*.

B. Yaakobi, C. Stoeckl, T. R. Boehly, D. D. Meyerhofer, and W. Seka, "Measurement of Preheat due to Fast Electrons in Laser Implosions," to be published in *Physics of Plasmas*.

B. Yaakobi, V. A. Smalyuk, J. A. Delettrez, F. J. Marshall, D. D. Meyerhofer, and W. Seka, "Measurement of Areal Density Modulation of Laser-Imploded Shells Through *K*-Edge Imaging," to be published in *Physics of Plasmas*.

J. D. Zuegel and D. W. Jacobs-Perkins, "An Efficient, High-Frequency Bulk Phase Modulator," to be published in *Applied Optics*.

Conference Presentations

R. Adam, M. Darula, and R. Sobolewski, "Subpicosecond Dynamics of the Switching Process in Y-Ba-Cu-O Josephson Junctions," SPIE's 14th Annual International Symposium on Aerospace/Defense Sensing, Simulation, and Controls, Orlando, FL, 24–28 April 2000.

The following presentations were made at CLEO/QELS 2000, San Francisco, CA, 7–12 May 2000:

A. Babushkin, M. J. Guardalben, R. S. Craxton, P. Adamson, H. Ammenheuser, R. L. Keck, and W. Seka, "Characterization of Frequency-Conversion Crystals for the Implementation of a 1-THz Bandwidth on the OMEGA Laser."

T. R. Boehly, D. D. Meyerhofer, Y. Fisher, W. Seka, and D. K. Bradley, "Measurements of the Optical Contrast on OMEGA: A 60-Beam, 30-kJ UV Fusion Laser."

A. V. Okishev, R. Boni, M. Millecchia, B. Kubera, P. A. Jaanimagi, W. R. Donaldson, R. L. Keck, W. Seka, K. V. Dukelsky, M. A. Eronyan, G. A. Shevandin, and G. A. Ermolaev, "A Unique High-Bandwidth, Multimode UV Optical Fiber: Manufacturing, Testing, and Laser-Fusion Applications."

The following presentations were made at the 30th Annual Anomalous Absorption Conference, Ocean City, MD, 21–26 May 2000:

R. Betti, J. P. Knauer, V. Lobatchev, and M. Umanski, "Hydrodynamic Instabilities from the Beginning to the End."

R. S. Craxton, J. P. Knauer, and R. P. J. Town, "Two-Dimensional Simulations of Cryogenic Deuterium Foil Acceleration for NIF Instability Experiments."

J. A. Delettrez, V. Smalyuk, B. Yaakobi, and D. D. Meyerhofer, "Results of Two-Dimensional Simulations of Implosions of DD-Filled CH Shell Targets on the OMEGA Laser."

R. Epstein, J. A. Delettrez, V. Yu. Glebov, V. N. Goncharov, P. W. McKenty, P. B. Radha, and S. Skupsky, "One-Dimensional Simulation of the Effects of Unstable Mix on Neutron and Charged Particle Spectra from Laser-Driven Implosion Experiments."

A. V. Kanaev and C. J. McKinstrie, "Numerical Simulations of SSD-Smoothed Laser Beam Filamentation and Forward SBS in Plasmas."

V. Lobatchev, R. Betti, and M. Umanski, "Numerical Study of Deceleration-Phase Rayleigh–Taylor Instability."

P. B. Radha, T. J. B. Collins, J. A. Delettrez, D. Keller, P. W. McKenty, and R. P. J. Town, "DRACO—A Multidimensional Hydrocode for ICF."

S. P. Regan, J. A. Delettrez, B. Yaakobi, R. Epstein, D. K. Bradley, D. D. Meyerhofer, and W. Seka, "Laser-Driven Burnthrough Experiments on OMEGA."

R. W. Short, "The Effects of Beam Intensity Structure on Two-Plasmon Decay in Direct-Drive Fusion Targets."

C. Stoeckl, V. Yu. Glebov, D. D. Meyerhofer, W. Seka, B. Yaakobi, and J. D. Zuegel, "Optical and X-Ray Signatures from the Two-Plasmon-Decay Instability on OMEGA."

T. R. Boehly, B. Yaakobi, D. Hoarty, J. P. Knauer, D. D. Meyerhofer, R. P. J. Town, R. E. Bahr, and M. Millecchia, "Measurements of Shock Heating Using Al Absorption Spectroscopy in Planar Targets," International Workshop on Warm Dense Matter, Vancouver, B.C., Canada, 29–31 May 2000.

J. P. Knauer, T. J. B. Collins, A. Frank, and E. Blackman, "Generation of Collimated Flows by Intense Laser Irradiation with Applications to Astrophysical Phenomena," 196th Meeting of the American Astronomical Society, Rochester, NY, 4–8 June 2000.

The following presentations were made at the 26th European Conference on Laser Interaction with Matter, Prague, Czech Republic, 12–16 June 2000:

S. Skupsky, R. L. McCrory, R. E. Bahr, T. R. Boehly, T. J. B. Collins, R. S. Craxton, J. A. Delettrez, W. R. Donaldson, R. Epstein, V. N. Goncharov, R. Q. Gram, D. R. Harding, P. A. Jaanimagi, R. L. Keck, J. P. Knauer, S. J. Loucks, F. J. Marshall, P. W. McKenty, D. D. Meyerhofer, S. F. B. Morse, O. V.

Gotchev, P. B. Radha, S. P. Regan, W. Seka, V. A. Smalyuk, J. M. Soures, C. Stoeckl, R. P. J. Town, M. D. Wittman, B. Yaakobi, J. D. Zuegel, R. D. Petrasso, D. G. Hicks, and C. K. Li, "Recent Progress in Direct-Drive ICF Research at the Laboratory for Laser Energetics."

B. Yaakobi, C. Stoeckl, T. R. Boehly, D. D. Meyerhofer, and W. Seka, "Measurement of Preheat due to Fast Electrons in Laser Implosions."

The following presentations were made at Optical Fabrication and Testing, Quebec City, Canada, 18–22 June 2000:

S. D. Jacobs and A. B. Shorey, "Magnetorheological Finishing: New Fluids for New Materials."

I. A. Kozhinova, S. D. Jacobs, S. R. Arrasmith, and L. L. Gregg, "Corrosion in Aqueous Cerium Oxide Magnetorheological Fluids."

A. B. Shorey and S. D. Jacobs, "Nanohardness of Abrasive Particles Used in Magnetorheological Finishing (MRF)."

The following presentations were made at the 13th Topical Conference on High-Temperature Plasma Diagnostics, Tucson, AZ, 18–22 June 2000:

T. R. Boehly, B. Yaakobi, D. Hoarty, J. P. Knauer, D. D. Meyerhofer, R. P. J. Town, R. E. Bahr, and M. Millecchia, "Measurements of Shock Heating Using Al Absorption Spectroscopy in Planar Targets."

J. A. Frenje, D. G. Hicks, C. K. Li, F. H. Séguin, R. D. Petrasso, K. Fletcher, H. Olliver, S. Padalino, S. Thompson, J. M. Soures, S. Roberts, C. Sorce, T. C. Sangster, and T. W. Phillips, "CR-39 Tract Detector Response to Charged Particles and Neutrons."

V. Yu. Glebov, D. D. Meyerhofer, C. Stoeckl, and J. D. Zuegel, "Secondary Neutron Yield Measurements by Current Mode Detectors."

P. A. Jaanimagi, R. Boni, and R. L. Keck, "Neutron-Induced Background in CCD Detectors."

C. K. Li, D. G. Hicks, F. H. Séguin, J. Frenje, R. D. Petrasso, J. M. Soures, P. B. Radha, V. Yu. Glebov, C. Stoeckl, J. P. Knauer, F. J. Marshall, D. D. Meyerhofer, S. Skupsky, S. Roberts, C. Sorce, T. C. Sangster, T. W. Phillips, and M. D. Cable, "Measuring Fusion Yields, Areal Densities, and Ion Temperatures of Imploded Capsules at OMEGA."

F. J. Marshall, T. A. Ohki, D. McInnis, Z. Ninkov, and J. Carbone, "Imaging of Laser-Plasma X-Ray Emission with Charge Injection Devices (CID)."

F. H. Séguin, C. K. Li, D. G. Hicks, J. A. Frenje, R. D. Petrasso, J. M. Soures, V. Yu. Glebov, P. B. Radha, D. D. Meyerhofer, S. Roberts, C. Sorce, T. C. Sangster, M. D. Cable, S. Padalino, and K. Fletcher, "Diagnostic Use of Secondary Proton Spectra for D-Filled ICF Targets."

V. A. Smalyuk, T. R. Boehly, L. S. Iwan, T. J. Kessler, J. P. Knauer, F. J. Marshall, D. D. Meyerhofer, C. Stoeckl, B. Yaakobi, and D. K. Bradley, "Fourier-Space Image Processing for Spherical Experiments on OMEGA."

C. Stoeckl, V. Yu. Glebov, D. D. Meyerhofer, W. Seka, B. Yaakobi, R. P. J. Town, and J. D. Zuegel, "Hard X-Ray Detectors for OMEGA and NIF."

The following presentations were made at Laser Optics 2000, St. Petersburg, Russia, 26–30 June 2000:

A. V. Okishev, R. Boni, M. Millecchia, B. Kubera, P. A. Jaanimagi, W. R. Donaldson, R. L. Keck, K. V. Dukelsky, M. A. Eronyan, V. S. Shevandin, G. A. Ermolaeva, and G. Nikolaev, "A Unique High-Bandwidth, UV Fiber Delivery System for the OMEGA Diagnostics Applications."

A. V. Okishev, M. D. Skeldon, R. L. Keck, and W. Seka, "A New High-Bandwidth, All-Solid-State Pulse-Shaping System for the OMEGA Laser Facility."

UNIVERSITY OF
ROCHESTER